Advanced computational analysis of calcium imaging data

Dissertation
to Fulfill the Requirements for the Degree of

Doctor of Philosophy (PhD)

submitted to the Faculty Council of the School of Medicine
at Friedrich Schiller University of Jena

by MSc. Vahid Rahmati
born on 11th January 1987 in Mashhad (Iran)

Zugl.: Dissertation, Friedrich-Schiller-Universität Jena, 2019

Gutachter *(akademischer Grad, Vor- und Nachname sowie Wirkungsort)*

1. Prof. Dr. rer. nat. Knut Holthoff (Universitätsklinikum Jena)

2. Prof. Dr.-Ing. Martin Bücker (Friedrich-Schiller-Universität Jena)

3. Prof. Dr. Dirk Ostwald (Freie Universität Berlin)

Tag der öffentlichen Verteidigung: 25.06.2019

I Table of Contents

II Glossary

$[Ca^{2+}]$	Intracellular Ca^{2+} concentration
CaBBI	Calcium imaging Analysis using Biophysical models and Bayesian Inference
UFARSA	Ultra-fast Accurate Reconstruction of Spiking Activity
HVA	High-voltage-activated
SNR	Signal-to-noise ratio
STP	Short-term synaptic plasticity
P	Postnatal day
TM	Template matching
GDP	Giant depolarizing potential
FP	Fixed point
FP-domain	Fixed point domain
ISN	Inhibition-stabilized network
Non-ISN	Non-inhibition-stabilized network
ROI	Region of interest

III Summary

Calcium imaging has emerged as a promising technique to indirectly measure the neural activity of populations of neurons, thereby enabling the functional analysis of these assemblies. This technique has been used to study the neural mechanisms and phenomena under a wide range of experimental and behavioral conditions. These include, as a point of interest for this thesis, the sparsification phenomenon occurring during early neocortical development, where population activity undergoes a dramatic transition from largely synchronized (cluster activity) to a relatively sparse mode around the time of eye-opening in rodents. Despite its wide-range of applications, the fluorescence traces (time-series) recorded by this technique are temporally smeared. This restricts the accurate reconstruction of quantities of interest such as spike times. Therefore, several spiking activity reconstruction methods have been introduced, where most of them are limited in dealing with issues such as variability in the kinetics of fluorescence transients, fast processing of long-term data, measurement noise and high firing rates. In addition, none of these methods provide insights into the underlying, intrinsic neuronal dynamics or biophysical parameters. As the first goal of this thesis, we sought to tackle these issues by introducing two novel reconstruction methods: i) CaBBI (Calcium imaging Analysis using Biophysical models and Bayesian Inference), and ii) UFARSA (Ultra-fast Accurate Reconstruction of Spiking Activity). While CaBBI is a neuronal model-based method aiming at inferring the underlying biophysical quantities such as membrane potential (thus, spikes) and voltage-gated channels' conductance, UFARSA is a heuristic method focusing on providing an ultra-fast, near-automatic reconstruction of spiking activities only. As the second goal, we sought to provide novel mechanistic insights into sparsification, whose underlying mechanisms are currently poorly understood. To this end, by integrating experimental findings, including only recently measured calcium imaging data covering the time course of sparsification, we present a dynamic systems modeling study of an *in vivo* developing neural network. With this approach, we address several aspects of sparsification such as i) the underlying mechanisms of cluster activity generation and its spatiotemporal characteristics, ii) the specific maturational processes mediating sparsification, and iii) the potential, developmental refinements in the network's information processing capabilities. Overall, this thesis not only provides novel tools of analyzing calcium imaging data in terms of the underlying biophysical quantities or ultra-fast near-automatic spiking activity reconstruction, but also presents how to analyze these data further with

computational models in order to reveal the mechanisms of the sparsification, as a signature of cortex maturation.

IV Zusammenfassung

Kalzium-Imaging hat sich als vielversprechende Methode zur indirekten Messung neuronaler Aktivität erwiesen und dadurch die funktionale Analyse von Neuronenpopulationen ermöglicht. Diese Methode wurde bereits eingesetzt um neuronale Mechanismen und Phänomene unter einer Vielzahl unterschiedlicher experimenteller und behavioraler Bedingungen zu untersuchen. Dazu gehört unter anderem das sogenannte "Sparsification"-Phänomen, welches von besonderem Interesse für diese Arbeit ist. Dieses Phänomen ist während der neokortikalen Entwicklung in Nagetieren zu beobachten, wenn großflächig synchronisierte Cluster-Aktivität einem Muster spärlicher Neuronenaktivität weicht. Dieses Phänomen tritt um den Zeitpunkt der Augenöffnungsphase der Jungtiere auf. Trotz des weit verbreiteten Einsatzes von Kalzium-Imaging ist das gemessene Fluoreszenzsignal zeitlich verschmiert. Dies limitiert die akkurate Rekonstruktion von Systemvariablen wie den Zeitpunkten des neuronalen Feuerns. Aus diesem Grund wurden bereits verschiedene Methoden zur Rekonstruktion neuronaler Aktivität eingeführt, wobei die meisten dieser Methoden Probleme wie die Variabilität der Fluoreszenzkinetik, eine schnelle Verarbeitung von Langzeitdaten, Mess-Ungenauigkeiten und hohe Feuerraten nur begrenzt zu lösen vermögen. Des Weiteren gibt keine dieser Methoden Aufschluss über die intrinsische neuronale Dynamik oder über biophysikalische Parameter. Als erstes Ziel dieser Arbeit versuchten wir deshalb, diese Punkte mithilfe zweier neuer Rekonstruktionsmethoden anzugehen: i) CaBBI (Calcium imaging analysis using Biophysical models and Bayesian Inference), und ii) UFARSA (Ultra-fast Accurate Reconstruction of Spiking Activity). Während CaBBI als modellbasierte Methode zum Ziel hat, biophysikalische Größen wie das Membranpotential und die Leitfähigkeit von spannungsgesteuerten Ionenkanälen zu ermitteln, ist UFARSA eine heuristische Methode zur ultraschnellen, nahezu automatischen Rekonstruktion der Zeitpunkte des neuronalen Feuerns. Als zweites versuchten wir, neue mechanistische Erkenntnisse zum bisher nur unzureichend verstandenen Sparsification-Phänomen zu erlangen. Daher präsentieren wir hier ein dynamisches System zur Modellierung eines sich *in vivo* entwickelnden neuronalen Netzwerks anhand unlängst gemessener Kalzium-Imaging-Daten, welche über den Zeitraum der Sparsification aufgenommen wurden. Dadurch

adressieren wir verschiedene Aspekte dieses Phänomens wie i) die zugrundeliegenden Mechanismen zur Erzeugung von Cluster-Aktivität und ihrer raumzeitlichen Eigenschaften, ii) die spezifischen Maturationsprozesse, welche zur Sparsification führen und iii) die potentielle Steigerung der Informationsverarbeitungskapazität des Netzwerks während der Entwicklung. Diese Arbeit präsentiert daher zum einen neue Werkzeuge zur Untersuchung von Kalzium-Imaging-Daten mit Augenmerk auf die zugrundeliegenden biophysikalischen Größen sowie auf die ultraschnelle, nahezu automatische Rekonstruktion der Feuerzeitpunkte. Zum anderen präsentieren wir hier Analysemethoden zur weiteren Untersuchung solcher Daten anhand von Computermodellen, um die Mechanismen des Sparsification-Phänomens als Ausdruck der Reifung des Kortex zu entschlüsseln.

1. Introduction

1.1. Neural network recording techniques

Measuring and quantifying neuronal network activity is a key to understand the operational principles of brain circuits. Available methods, which strongly differ in their spatiotemporal resolution, include extracellular recordings of local field potential and spiking activity, magneto- and electroencephalography, and functional magnetic resonance imaging. These methods have been widely used in both research and clinical studies to investigate the neural network mechanisms involved in, e.g., sensory processing, memory, perception, neural development, and attention (Chow et al. 2017, Herreras 2016, Baillet 2017, Kirmse et al. 2015, Linden et al. 2011, Buzsaki et al. 2012, Jackson und Bolger 2014). Since neurons are the basic functional units in the brain, the simultaneous measurement of their activity can enable a closer analysis of the mechanisms underlying computations in neuronal networks (Chorev et al. 2009). Among the afore-mentioned techniques, only extracellular single-/multi-unit measurements provide single cell resolution (Uludag und Roebroeck 2014, Min et al. 2010). However, extracellular recording techniques have several issues that limit their potential application (Chorev et al. 2009, Harris et al. 2016, Obien et al. 2015). One drawback lies in the cell identification: Isolating single unit responses from the recorded traces (time-series) usually involves a spike sorting step, which is a very challenging problem given that action potential waveforms of individual neurons may vary considerably. Second, the recorded traces are subject to substantial sampling bias in terms of the tendency to record from more active and larger neurons. Third, long-term recordings of the same units, in particular under *in vivo* conditions, are in practice difficult. Considering these issues, calcium imaging has emerged as an alternative method that not only enables recording of neuronal population activity with single cell resolution but also can overcome the issues of multi-unit recordings. We will describe this relatively new method in the following section.

1.2. Calcium imaging

1.2.1. Overview of the technique

Calcium imaging is a widely used technique to indirectly record the neural activity of both individual and populations of neurons (Grienberger und Konnerth 2012, Russell 2011). With this technique, the target neural structures are labeled by fluorescence calcium indicators. This can be done through a direct injection or a genetically encoding procedure (Lin und Schnitzer 2016, Chen et al. 2013b). This enables imaging the changes in the intracellular Ca^{2+} concentration

([Ca^{2+}]) by optical devices, thereby monitoring the underlying spiking activities. Each spike is monitored as a fluorescence transient composed of, usually, a sharp increase (rising phase) followed by a slow decay (decaying phase) (Grewe et al. 2010). This follows as spike generation activates high-voltage-activated (HVA) calcium channels (L-, N-, P/Q-, and R-type (Catterall 2000)) which can in turn trigger a relatively large, fast increase in [Ca^{2+}]. Subsequently, different cellular pumping and buffering mechanisms decline [Ca^{2+}] and govern the decay kinetics of transient.

Calcium imaging is applicable to both *in vivo* and *in vitro* brain preparations (Ackman et al. 2012, Kirmse et al. 2015, Kerr et al. 2005a), and can be performed at multiple spatial structure levels from neural sub-compartments (Brenowitz und Regehr 2007, Majewska und Sur 2003), individual neurons (Kerr et al. 2005a, Golshani et al. 2009) to rather large neuronal populations (Gobel und Helmchen 2007, Ohki et al. 2005, Ackman et al. 2012). The temporal resolution of this technique in regular calcium imaging recordings is usually between 20-50 ms. However, with the advent of new optical devices (Grewe et al. 2010, Prevedel et al. 2016), this technique can reliably acquire data with a temporal resolution up to a millisecond. This technique can also be combined with electrophysiological recordings and optogenetic techniques (Kirmse et al. 2015, Valeeva et al. 2016, Yang et al. 2018). These features, and in particular the ability of calcium imaging to simultaneously record activity of large populations of neurons, has been made it a suitable technique for the functional analysis of neural assemblies. In sum, calcium imaging provides novel ways for investigating the neural information processing and phenomena occurring under diverse experimental and behavioral conditions; e.g. different pharmacological manipulations, or spontaneous vs. stimulus-driven conditions (Grienberger und Konnerth 2012, Adelsberger et al. 2005, van der Bourg et al. 2016, Yaksi und Friedrich 2006, O'Shea et al. 2017, Chen et al. 2013a).

1.2.2. Analysis limitations: reconstruction challenge

Despite the wide range of applications of calcium imaging, reconstruction of quantities of interest such as exact spiking activity or [Ca^{2+}] kinetics from fluorescence traces (time-series) is challenging. This is mainly due to the contamination of these traces with different types of artifacts, measurement noise, and the intrinsic slow [Ca^{2+}] kinetics *per se*, relative to the fast time scale of spikes. Several methods have been already proposed to reconstruct spiking activities from fluorescence traces, based on various techniques. These include first derivative (Smetters et

al. 1999), nonlinear supervised classifying (Sasaki et al. 2008), template-matching (Greenberg et al. 2008, Grewe et al. 2010, Kerr et al. 2005b, Clements und Bekkers 1997), maximum entropy (Park et al. 2013), sequential Monte Carlo (Vogelstein et al. 2009), and deconvolution (Moreaux und Laurent 2007, Vogelstein et al. 2010, Yaksi und Friedrich 2006, Pnevmatikakis et al. 2016). For instance, as example of popular methods, a first-derivative-based method computes the first derivative of the fluorescence trace and then threshold it by a specific level to reconstruct the spiking events. A template-matching-based method usually, by using a set of specific conditions, compares the candidate transients in the recorded trace with an empirical or pre-defined template of a fluorescence transient, in order to either accept or reject each candidate as to be evoked by a spiking event. A deconvolution-based method usually considers a mathematical model of $[Ca^{2+}]$ kinetics and its relationship to the observed variable, the fluorescence data. Assuming that the convolution of this model with an unknown spiking activity train yielded the recorded trace, inversion approaches such as Bayesian inference and the inverse Fourier transform are used to reconstruct the spiking events from the recorded trace.

Whereas these reconstruction methods markedly improved the reconstruction accuracy over recent years, they still face a number of important limitations. First, one common property of these methods is that they are not able to provide insight into the biophysical quantities such as the membrane potential or the conductance of voltage-gated channels, from the recorded calcium imaging data. This is mainly because these methods are not based on biophysical models of how neurons fire. Clearly, such neuronal models exist and are widely used to model different biophysical aspects and firing patterns, based on electrophysiological data (Ermentrout und Terman 2010, Izhikevich 2007, Izhikevich 2004). One idea is to use these neuronal models to derive generative models of fluorescence traces, and use Bayesian methods to infer about the underlying biophysical quantities. For instance, in a similar fashion, for magneto- and electroencephalography, inverting such biophysically interpretable models by Bayesian inference approaches has been found useful for inferring the underlying neural dynamics and identifying brain effective connectivity patterns (David et al. 2006, Kiebel et al. 2009).

Most established reconstruction techniques are also limited in how they deal with issues such as fast processing of long-term data (or data acquired at high temporal resolution), heterogeneity of fluorescence transients' kinetics, relatively high firing rates, measurement noise, and artifacts. In addition, the results of these methods usually depend on the user's expertise in a specific method;

e.g. when adapting a method to data with different decay kinetics. These issues are common in studies based on calcium imaging recordings and potentially reduce the reliability of the reconstruction process. Resolving these issues remains challenging, and is a highly dynamic methods research area.

1.3. Sparsification

1.3.1. A signature of cortex maturation

The postnatal development of vertebrates' cortical networks determines the intricate functionality of adult neuronal networks. The proper development of these networks is strongly activity dependent (Khazipov und Luhmann 2006, Luhmann et al. 2016). A common characteristic of the immature cortical neural networks is to generate largely synchronized network activity, so-called cluster activity, or otherwise being mostly silent for relatively long periods (Golshani et al. 2009, Kirmse et al. 2015, Rochefort et al. 2009). In mammals, including human infants (Arichi et al. 2017, Vanhatalo et al. 2005, Colonnese et al. 2010), cluster activity has been observed in different brain areas both *in vitro* (Garaschuk et al. 2000, Dupont et al. 2006, Easton et al. 2014) and *in vivo* (Khazipov et al. 2004, Leinekugel et al. 2002, Yang et al. 2009). The specific spatiotemporal patterns of cluster activity are believed to play a critical role in the proper development of neural networks (Burbridge et al. 2014, Zhang et al. 2011). Importantly, it has been found that the perturbation of these early network activities can bring about long-term alterations of cortical and hippocampal networks (Marguet et al. 2015, Tolner et al. 2012). Such alterations can be predictive of neurodevelopmental disorders (Kirmse et al. 2018).

During development, network activity undergoes a dramatic transition from cluster activity to a relatively sparse mode around the time of eye-opening in rodents (Colonnese et al. 2010, Golshani et al. 2009, Rochefort et al. 2009, van der Bourg et al. 2016). This sparsification phenomenon has also been observed in human cortex, which sets in by the time of normal birth (Vanhatalo et al. 2005). The Sparse firing is thought to provide an efficient coding strategy for neural information processing and storing in adult neural networks (Kerr et al. 2005a, Olshausen und Field 2004, Shadlen und Newsome 1994). Since, unlike adult networks, generating cluster activity is a ubiquitous feature of many neural structures (Khazipov und Luhmann 2006, Luhmann et al. 2016), sparsification is thought to be a universal phenomenon of neural network maturation.

Importantly, in the recent years, *in vivo* calcium imaging techniques allowed for a "continuous" monitoring of the transition from dense to sparse coding in "intact" developing networks during the first postnatal month; i.e. the time course of sparsification process (Golshani et al. 2009, Rochefort et al. 2009). These studies not only uncovered the continuous developmental trajectory of network activity, but also revealed new characteristics of sparsification which had been remained obscure based on *in vitro* studies. For instance, it was found that sparsification is largely, though not entirely (Rochefort et al. 2009), mediated internally rather than being an experience dependent phenomenon, or that the loss of large cluster activity occurs around the time of eye-opening (Golshani et al. 2009, Rochefort et al. 2009) and not around the 7th postnatal day (P7) (Garaschuk et al. 2000).

Strikingly, the time course of sparsification coincides with major developmental changes in both intrinsic neuronal and synaptic properties. These include a sharp increase in the number (or density) of glutamatergic and GABAergic synapses (De Felipe et al. 1997, Feldmeyer und Radnikow 2009), a potent decrease in membrane resistance, an acceleration of postsynaptic currents (Etherington und Williams 2011, Golshani et al. 2009), an increase in background activity level (Golshani et al. 2009, Rochefort et al. 2009), as well as profound changes in short-term synaptic plasticity (STP) (Etherington und Williams 2011, Feldmeyer und Radnikow 2009).

1.3.2. Underlying mechanisms?

Despite the established experimental findings, and while sparsification is thought to be a development signature of all cortical areas examined to date (Colonnese et al. 2010, Golshani et al. 2009, Rochefort et al. 2009, van der Bourg et al. 2016) as well as in human cortex (Vanhatalo et al. 2005), the biophysical mechanisms underlying or being involved in sparsification remain poorly understood. In particular, it is currently unclear (i) what the origin of spontaneous activity in the developing networks is, (ii) what are the essential or perquisite maturational processes for transitioning network activity from dense to sparse coding, and (iii) what potential refinements in the network information processing capabilities prepare the network for an effective sensory processing towards the postnatal onset of sensory transduction. In this line, a computational modeling study, taking currently available experimental findings into account, might allow to mechanistically address these open questions and generate useful predictions for future experimental studies. However, there is currently no such unified modeling approach that provides a single explanation for these developmental observations, in a coherent fashion.

2. Objectives of this thesis

There are two goals in this thesis, the first is driven by the need for improved reconstruction techniques, and the second by the elusive underlying mechanism of sparsification:

First, despite the considerable advances in calcium imaging technique over recent years, extracting quantities of interest from recorded fluorescence traces remains restricted. The restrictions include making inference about relevant biophysical parameters and variables, as well as an accurate reconstruction of underlying spiking activities. Therefore, even though many different methods have been proposed already, there is still a need for methods which can handle issues such as such complex nonlinear relationship between neuronal dynamics and recorded fluorescence intensities, measurement noise, artifacts, high firing rates, systematic variation in fluorescence transient kinetics, and fast processing of long-term data. Taken together, as the first goal of this thesis we focused on developing novel reconstruction methods to overcome these limitations. To this end, we sought to develop one neuronal model-based method for making inference about the underlying biophysical quantities, and one heuristic method specifically for spiking activity reconstruction.

Second, while accumulating evidence, including recent findings based on *vivo* calcium imaging data (Golshani et al. 2009, Rochefort et al. 2009), suggests that sparsification is a universal phenomenon of neural network maturation, the underlying mechanisms governing this phenomenon remain poorly understood. For instance, it has not completely understood yet that i) how in the absence of sensory inputs, an immature network can be quiescent for relatively long periods and then abruptly elicit large cluster activity, ii) which biophysical parameters govern the spatiotemporal characteristics of cluster activity, iii) which, and how, specific maturational processes drive sparsification, iv) what is the role of GABA during the first postnatal week, and v) how information processing capabilities of a developing network are refined during sparsification, to prepare it for an effective processing of sensory stimuli towards the time of eye-opening. Therefore, as the second goal of this thesis we aimed at addressing these open questions. To this end, we first sought to combine well-established neural network models with the experimentally measured developmental trajectory of neurobiological parameters and network activity, in order to emulate the *in vivo* activity of a developing network during the first postnatal month. We then used a dynamics system approach in combination with network

simulations to investigate different firing and information processing characteristics of the developing network.

3. Manuscript overview

Manuscript I

Inferring Neuronal Dynamics from Calcium Imaging Data Using Biophysical Models and Bayesian Inference

Vahid Rahmati , Knut Kirmse, Dimitrije Marković, Knut Holthoff, Stefan J. Kiebel

PLoS Computational Biology, 2016 Feb; 12, e1004736, doi: 10.1371/journal.pcbi.1004736
(IF:4.58)

Date of acceptance: 5th January, 2016

In this publication, we developed a novel deconvolution method called CaBBI: Calcium imaging Analysis using Biophysical models and Bayesian Inference. CaBBI is the first method in providing insights into the biophysical quantities underlying calcium imaging data. To this end, in a Bayesian framework, it inverts both well-established and novel biophysical generative models, which create a direct link between neuronal dynamics, e.g. membrane potential and fluorescence traces. Using both synthetic and experimental fluorescence traces, we show that CaBBI not only performs accurate spiking activity reconstruction but also reliably infers the relevant biophysical parameters and variables like membrane potential or $[Ca^{2+}]$ kinetics, as well as the parameter changes e.g. due to a pharmacological intervention. Software repository and wiki for CaBBI can be found at: http://mbb-team.github.io/VBA-toolbox/wiki/CaBBI/.

V.R., K.K., K.H. and S.J.K. designed the study. V.R. developed the method and generative models, ran the simulations, and analyzed the data. KK performed the experiments and participated in analyzing the data. V.R., K.K., K.H. and S.J.K. participated in the interpretation of the data and results. V.R., K.K., D.M., K.H. and S.J.K. wrote the manuscript.

Personal contribution: 80%

Manuscript II

Ultra-fast accurate reconstruction of spiking activity from calcium imaging data

Vahid Rahmati, Knut Kirmse, Knut Holthoff, Stefan J. Kiebel

Journal of Neurophysiology, 2018 May; 119(5): 1863-1878, doi: 10.1152/jn.00934.2017
(IF:2.89)

Date of acceptance: 15th February, 2018

In this publication, we developed a novel reconstruction method called UFARSA: Ultra-fast Accurate Reconstruction of Spiking Activity. UFARSA is a heuristic, model-free-type method for reconstructing spiking activity from calcium imaging data. Using both synthetic and experimental data, we demonstrated that for a noisy fluorescence trace it provides an ultra-fast, accurate, near-automatic reconstruction of both isolated and within-burst spikes, as well as spike count per transient. The reconstruction is robust against the heterogeneity in the rise and decay kinetics or amplitudes of transients. Furthermore, it can correct for several artifacts, including fast and rather complex, slowly varying temporal drifts as frequently observed in *in vivo* data. Software repository and wiki for UFARSA can be found at: https://github.com/VahidRahmati/UFARSA.

V.R., K.K., K.H. and S.J.K. designed the study. V.R. developed the method, ran the simulations, and analyzed the data. V.R., K.K., K.H. and S.J.K. participated in the interpretation of the data and results. V.R., K.K., K.H. and S.J.K. wrote the manuscript.

Personal contribution: 80%

Manuscript III

Developmental Emergence of Sparse Coding: A Dynamic Systems Approach

Vahid Rahmati, Knut Kirmse, Knut Holthoff, Larse Schwabe, Stefan J. Kiebel

Scientific Reports (Nature), 2017 October; 7 (1):13015, doi: 10.1038/s41598-017-13468-z
(IF:4.6)

Date of acceptance: 25th September, 2017

In this publication, we provided the first mechanistic insights into the sparsification phenomenon. To this end, we presented a computational dynamic systems modeling study of an *in vivo* developing neural network, based on experimentally measured trajectories of intrinsic neuronal and synaptic parameters as well as network activity, during first postnatal month. By using the mathematical tool of stability analysis and network simulations, we derived several key results regarding this phenomenon. Importantly, we revealed the potent effect of a transient unstable state, hidden in network firing dynamics on its cluster activity generation. We addressed the mechanisms governing the spatiotemporal characteristics of cluster activity and the developmental refinements in network's information processing capabilities, over the sparsification time course. Furthermore, we quantified the effect of different maturational processes on driving sparsification, in terms of network biophysical parameters. This work not only suggests how adult sparse coding networks may emerge developmentally, but also provides concrete predictions to be tested experimentally.

V.R., K.K., K.H., L.S. and S.J.K. designed the study. V.R. designed the model, derived analytical expressions, and ran the simulations. V.R., K.K., K.H., L.S. and S.J.K. participated in the interpretation of the data and findings. V.R., K.K., K.H., L.S. and S.J.K. wrote the manuscript.

Personal contribution: 80%

4. Manuscripts

4.1. Manuscript I

Inferring Neuronal Dynamics from Calcium Imaging Data Using Biophysical Models and Bayesian Inference

Vahid Rahmati , Knut Kirmse, Dimitrije Marković, Knut Holthoff, Stefan J. Kiebel

PLOS | COMPUTATIONAL BIOLOGY

RESEARCH ARTICLE

Inferring Neuronal Dynamics from Calcium Imaging Data Using Biophysical Models and Bayesian Inference

Vahid Rahmati[1,2]*, Knut Kirmse[3], Dimitrije Marković[1,2,4], Knut Holthoff[3], Stefan J. Kiebel[1,2,4]

1 Department of Psychology, Technische Universität Dresden, Dresden, Germany, **2** Biomagnetic Centre, Hans-Berger Department of Neurology, University Hospital Jena, Jena, Germany, **3** Hans-Berger Department of Neurology, University Hospital Jena, Jena, Germany, **4** Max Planck Institute for Human Cognitive and Brain Sciences, Leipzig, Germany

* vahid.rahmati@tu-dresden.de

OPEN ACCESS

Citation: Rahmati V, Kirmse K, Marković D, Holthoff K, Kiebel SJ (2016) Inferring Neuronal Dynamics from Calcium Imaging Data Using Biophysical Models and Bayesian Inference. PLoS Comput Biol 12(2): e1004736. doi:10.1371/journal.pcbi.1004736

Editor: Claus C. Hilgetag, Hamburg University, GERMANY

Received: June 18, 2015

Accepted: January 5, 2016

Published: February 19, 2016

Data Availability Statement: All experimental data are available from the figshare database (http://figshare.com/s/e524c1d214d411e5869c06ec4b8d1f61).

Funding: This work was supported by the German Research Foundation and the Open Access Publication Funds of the TU Dresden, the Priority Program 1665 (HO 2156/3-1, KI 1816/1-1 and KI 1638/3-1), the Collaborative Research Center/Transregio 166 of the German Research Foundation (TRR 166/1 B3 to KH and KK), the Research Group FO 1738 (WI 830/10-2 to KH), the Federal Ministry of Education and Research (01GQ0923 to KH) and the Interdisciplinary Centre for Clinical Research Jena (to

Abstract

Calcium imaging has been used as a promising technique to monitor the dynamic activity of neuronal populations. However, the calcium trace is temporally smeared which restricts the extraction of quantities of interest such as spike trains of individual neurons. To address this issue, spike reconstruction algorithms have been introduced. One limitation of such reconstructions is that the underlying models are not informed about the biophysics of spike and burst generations. Such existing prior knowledge might be useful for constraining the possible solutions of spikes. Here we describe, in a novel Bayesian approach, how principled knowledge about neuronal dynamics can be employed to infer biophysical variables and parameters from fluorescence traces. By using both synthetic and *in vitro* recorded fluorescence traces, we demonstrate that the new approach is able to reconstruct different repetitive spiking and/or bursting patterns with accurate single spike resolution. Furthermore, we show that the high inference precision of the new approach is preserved even if the fluorescence trace is rather noisy or if the fluorescence transients show slow rise kinetics lasting several hundred milliseconds, and inhomogeneous rise and decay times. In addition, we discuss the use of the new approach for inferring parameter changes, e.g. due to a pharmacological intervention, as well as for inferring complex characteristics of immature neuronal circuits.

Author Summary

Calcium imaging of single neurons enables the indirect observation of neuronal dynamics, for example action potential firing. In contrast to the precise timing of spike trains, the calcium trace is temporally rather smeared and measured as a fluorescence trace. Consequently, several methods have been proposed to reconstruct spikes from calcium imaging data. However, a common feature of these methods is that they are not based on the biophysics of how neurons fire spikes and bursts. We propose to introduce well-established

PLOS | COMPUTATIONAL BIOLOGY

KK and KH). The funders had no role in study design, data collection and analysis, decision to publish, or preparation of the manuscript.

Competing Interests: The authors have declared that no competing interests exist.

biophysical models to create a direct link between neuronal dynamics, e.g. the membrane potential, and fluorescence traces. Using both synthetic and experimental data, we show that this approach not only provides a robust and accurate spike reconstruction but also a reliable inference about the biophysically relevant parameters and variables. This enables novel ways of analyzing calcium imaging experiments in terms of the underlying biophysical quantities.

Introduction

Calcium imaging has been used to record neuronal activity indirectly [1]. Individual neurons or neuronal populations are labeled by applying fluorescent calcium indicators so that the intracellular calcium transients become measurable by optical means. The technique has a temporal resolution up to the millisecond scale and allows measurements at multiple structural levels, from cellular sub-compartments [2,3] and individual neurons [4,5] to rather large neuronal ensembles [6–8]. Moreover, calcium imaging can be applied to both *in vivo* [6,9,10] and *in vitro* brain preparations [11,12].

While calcium imaging techniques have a wide range of applications, the reconstruction of the quantities of interest such as spike (or action potential) trains and intracellular free calcium concentration, $[Ca^{2+}]$, kinetics from fluorescence, F_b, traces is restricted mostly due to the intrinsic low temporal resolution of calcium traces, relative to the fast time scale of spikes. Several algorithms for the reconstruction of spikes from calcium imaging data have been proposed. These include template matching [7,9,13,14], first-derivative methods including deconvolution [15–17], reverse correlation [18] and a sequential Monte Carlo method [19].

One common feature of these previously described reconstruction methods is that they are not based on biophysical models for how spikes are generated. Such biophysical models have been developed to model different biophysical characteristics and firing patterns observed in electrophysiological data [20,21]. Here, we specify a generative forward model by explicitly linking the membrane potential (V), rather than only spikes, to fluorescence traces through $[Ca^{2+}]$ kinetics. We pursue the idea that reconstruction of spikes and, potentially, inferring the underlying neuronal dynamics, can be performed by inverting this generative forward model. The inversion of such biophysically plausible models has been found useful for magneto- and electroencephalography and can be performed using Bayesian inference techniques [22,23]. The expected advantages for the analysis of calcium imaging data, relative to existing approaches, are an increased robustness to noise and artefacts, incorporation of biophysically sensible prior information, and the biophysical interpretation of inferred variables and identified parameters. In addition, the Bayesian inference approach captures the uncertainty about the inferred quantities of interest, thereby allowing one to assess which dynamics and parameters can be inferred from the fluorescence traces, and which ones cannot.

As an illustration and proof-of-concept of the proposed modelling approach, we use both synthetic and *in vitro* calcium imaging data. We show for both data sets that spikes can be reconstructed accurately, even under low signal to noise (SNR) conditions, through inferring the neuronal dynamics such as membrane potential, $[Ca^{2+}]$ kinetics, membrane refractoriness and voltage-gated ionic currents. One important, potential application of the approach may be its use to reconstruct spikes from imaging data at high sampling rates but with rather low SNRs. We will show that the biophysical model reliably infers the within-burst or single spikes and also quantitatively captures and infers several experimental phenomena, e.g. fluorescence transients with both typical (i.e. fast) [13,24–26] or slow rise kinetics [27], and the somatic

bursts of hippocampal pyramidal neurons [28–30]. We will further demonstrate the usefulness of the approach for experimental setups like a pharmacological intervention where predictions about the change in specific biophysical parameters can be tested directly. To illustrate the method on real data, we use our recorded data from immature neurons of neonatal mice which impose a challenging spike reconstruction task, due to the slow rise kinetics of their spike-evoked fluorescence transients. In addition, we apply the method to a publicly available *in vitro* data set with fast rising fluorescence transients. To reduce the computational complexity of the method we also introduce and use two new, differentiable integrate-and-fire models for repetitive spiking and bursting firing patterns.

Methods

Overview

Our approach for model-based analysis of calcium imaging data is based on linking the neuronal membrane potential, to the fluorescence traces by using the kinetics of $[Ca^{2+}]$ as an intermediate variable. This requires three components: (i) a model for the membrane dynamics and how spikes are generated, (ii) a model for the $[Ca^{2+}]$ kinetics, where the entry via Ca^{2+} influx is regulated by a nonlinear function representing the activation-state of high-voltage-activated (HVA) calcium channels, and (iii) an observation function which provides a noisy nonlinear mapping from the generated $[Ca^{2+}]$ time series to the fluorescence trace. These three model components form a so-called generative model which explains how data are generated starting from the membrane potential. Given a fluorescence trace, we 'invert' this model by making inference on the neuron's underlying hidden states (i.e. dynamics) and/or parameters, see Fig 1A.

For inference, we use a recently developed approximate (variational) Bayesian inference approach [31] for stochastic, nonlinear state-space models, i.e. discretized stochastic nonlinear dynamic systems. In the following, we refer to this variational Bayesian approach as VB-Laplace. This approach performs efficient and robust parameter estimation even if both the evolution and observation equations (as with the proposed calcium imaging model) are nonlinear. As the framework enables analytical update equations, the method is generic and efficient in terms of computation time. Critically, the approach also enables the estimation of parameters (e.g., calcium decay time-constant) and precision-parameters, e.g. noise level on fluorescence trace. As we will show below, this is important for the application to calcium imaging data. As with any Bayesian approach, the method relies on the specification of the prior distributions of the parameters. This is useful because the generative model is biophysical and plausible prior knowledge can be derived directly from previous modelling and experimental studies.

The generative model is defined in terms of its state (i.e. evolution) and observation (i.e. likelihood) equations:

$$\text{Generative model}: \begin{cases} x_{t+1} = f(x_t, \theta, u_t) + \eta_t \\ y_t = g(x_t, \varphi, u_t) + \varepsilon_t \end{cases} \quad (1)$$

where x denote the states of neuronal dynamics such as V and $[Ca^{2+}]$, y_t refers to the fluorescence responses, θ and φ are quantities that parameterize the state evolution function f and observation function g, respectively, and u_t is the synaptic (or applied) input time series to the membrane. In this generic formalism, η_t denotes state-noise with precision (i.e., inverse variance) α and ε_t denotes measurement-noise with precision σ. The both random variables are drawn from zero-mean Gaussians: $\eta_t \sim N(0,(\alpha\Upsilon_x)^{-1})$ and $\varepsilon_t \sim N(0,(\sigma\Upsilon_y)^{-1})$, where Υ_x and Υ_y denote their corresponding inverse covariance matrices. The state equations (Eq 1) are derived

PLOS | COMPUTATIONAL BIOLOGY

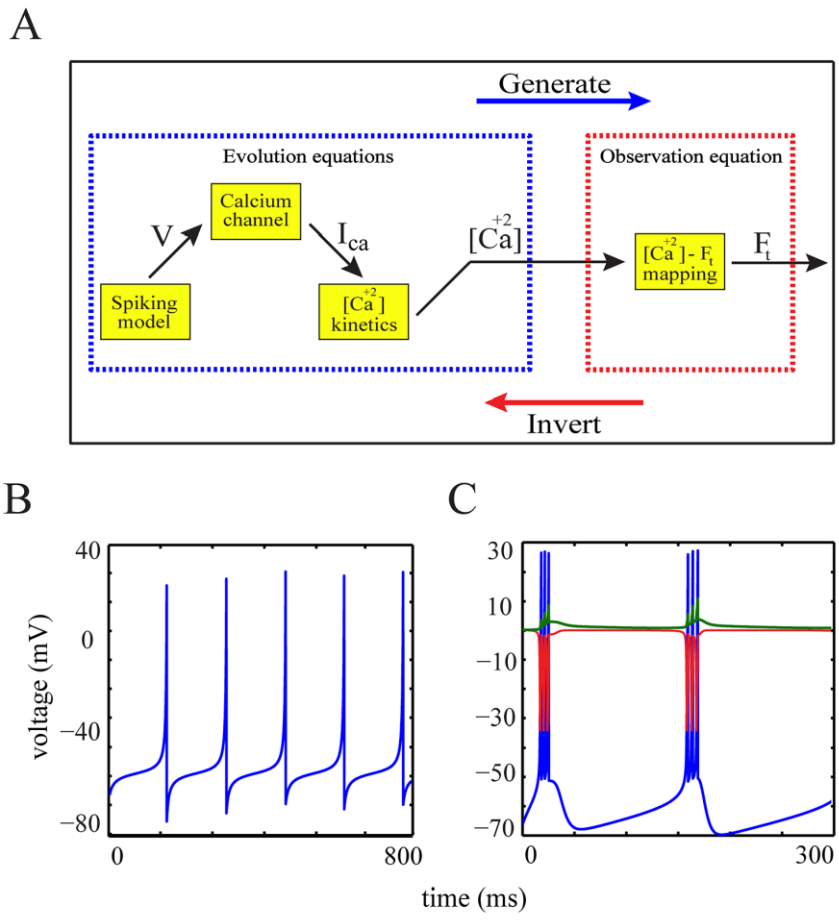

Fig 1. The generative model and non-hybrid quadratic integrate-and-fire (family of QGIF) models. (**A**) Graph representing the generative model and its inversion, which are comprised of evolution (i.e., a neuron model) and observation equations. The illustrated hierarchy in the graph displays how neuronal dynamics relate to fluorescence traces. (**B** and **C**) Sample voltage traces of (**B**) QGIF and (**C**) bursting-QGIF models. The traces show the rhythmic activity of these models in response to sustained depolarizations. Note that the family of QGIF models does not require any reset condition for spike/burst generation. The persistent Na^+ and M-type K^+ currents (red and green lines, respectively) of bursting-QGIF model are in units of [$\mu A / cm^2$]. Parameters for the simulations: (**B**) $I_{app} = 0.2\ \mu A / cm^2$, (**C**) $\bar{I}_{rep} = 80\ \mu A\ mS/\mu F$, $I_{app} = 1\ \mu A / cm^2$. See Table 1 for the rest of parameter values.

doi:10.1371/journal.pcbi.1004736.g001

from a set of first-order nonlinear differential equations which formulate the interaction between the underlying neuronal mechanisms. By integrating these equations and passing the $[Ca^{2+}]$ states through the observer equation, F_t traces are generated. This operator is assumed to be a saturating (nonlinear) function.

In what follows, we use Eq 1 as the basis for all following models, where the evolution and observation functions are specified in detail to derive several models that we used to analyze calcium imaging data. One guiding principle for the following selection of biophysical models is that we prefer models with low complexity and dimensionality, i.e. a low number of parameters and variables. Theoretical considerations and preliminary analyses showed that it is

unlikely that all parameters of highly detailed, complex models can be inferred from fluorescence traces, which are temporally smooth in comparison to spike data.

Evolution functions

Evolution functions are the neuronal models which formulate the neuron biophysics; they link the dynamic change in the membrane potential (in response to input) to the $[Ca^{2+}]$ kinetics. These models are comprised of three units: (i) a spiking model which (mainly) governs the membrane potential, (ii) a model for the mechanism of HVA calcium channels where the membrane potential controls the amount of calcium current entering the neuron, and (iii) an equation to model the modulation of $[Ca^{2+}]$ due to both the removal mechanisms of free cytoplasmic Ca^{2+} and the change in calcium current. The resulting $[Ca^{2+}]$ kinetics will be used later in the observation equation in order to compute the fluorescence trace (see Eq 12).

Spiking models

Spiking models can be categorized broadly into two groups: single- and multi-compartment models. The spiking models reported in the literature, for example [29,32–37], can reproduce a wide-range of repetitive spiking and/or bursting firing patterns of neurons; for reviews see also [20,21,38,39]. Since the fluorescence traces we considered were extracted exclusively from the somata, it is a sufficient approximation here to adopt single-compartment models of the cell body. In principle, any model based on differential equations can be used as a generative model of spikes. To show this anecdotally but also to investigate whether there is any particular model that may be best suited for modelling calcium transients, we selected three different models. We used two repetitive spiking models (i.e., the Fitzhugh-Nagumo model and Quadratic-Gaussian integrate-and-fire (I&F) model) with different model complexities (i.e., number of parameters and variables), as well as a model for compound spiking and/or bursting patterns (i.e., bursting-Quadratic-Gaussian I&F). We motivate the choice of each of these three models, in the three next sections below.

In all spiking models considered next, the total input current to neuron is $I = I_{app} + I_{syn}$, where I_{app} and I_{syn} are applied and synaptic currents, respectively.

FitzHugh-Nagumo Model (FHN). The FitzHugh-Nagumo model is a two-dimensional reduction of the Hodgkin-Huxley (HH) model and is one of the most widely-used models of spike generation [40–42]. Unlike the HH model, which has four dynamical variables with highly nonlinear equations, the FHN model is based only on a 2D system of equations with less nonlinearities. This reduced complexity and dimensionality motivated our choice of the FHN model, rather than the HH model. The FHN model describes the spike generation by two equations:

$$\frac{d}{dt}V = V - \frac{V^3}{3} - W + I \tag{2}$$

$$\frac{d}{dt}W = \lambda(V + \psi_1 - \psi_2 W)$$

where parameters λ, ψ_1 and ψ_2 are constants, V denotes the membrane potential, and W denotes the recovery variable of the membrane; V and W are dimensionless variables that have biophysical roles and time scales similar to the voltage-gated ionic channels (e.g. activation of K^+, and inactivation of Na^+ channels) in the HH model [35]. Note that the FHN model does not fire all-or-none spikes. Depending on the input strength, it may generate subthreshold

responses, or partial- or full-amplitude spikes [41]. As a consequence, similarly to the HH model, no well-defined firing threshold exists in the FHN model [41,43].

Quadratic-Gaussian Integrate-and-Fire model (QGIF). For a further reduction of model complexity, we can use single-variable (i.e. 1D) spiking models instead of the 2D FHN model. The 1D models such as standard I&F model [44–47], or its analogues [48] use the membrane potential as the only dynamical variable to generate spikes. From our perspective, the main drawback of these so-called hybrid models is their non-differentiability; that is, they demand (at least) one *if* condition due to the resetting of the membrane potential whenever a spike reaches its peak. The generative models in the presence of such a step function cannot be well inverted by our VB-Laplace method. To overcome this technical difficulty, we extended a quadratic I&F model. The advantage of the quadratic I&F model is its activity-dependent threshold (for non-zero inputs) and spike latency [21], as found experimentally. In addition, it produces the upstroke of a spike by the bistability of its resting and repetitive spiking states. Therefore, this model only requires one resetting condition which is used for hyperpolarizing the membrane potential at the spike's peak. Furthermore, it is computationally affordable [49] when compared to other nonlinear alternatives such as exponential I&F model [48]. In summary, by adapting this hybrid model [48] we created a novel 1D spiking model (i.e. the quadratic-Gaussian I&F (QGIF) model) without any discontinuous reset condition. This makes the model differentiable and invertible with the proposed Bayesian approach. The membrane potential in the QGIF model is governed by the following equations:

$$\begin{aligned} C\frac{d}{dt}V &= I - I_L + f_{sp}(V) - \frac{f_{rep}(V)}{\gamma} \\ I_L &= g_L(V - E_L) \end{aligned} \tag{3}$$

where C denotes the membrane capacitance, g_L the leak conductance, I_L the leak current, and E_L the leak reversal potential. Finally, $f_{sp}(V)$ and $f_{rep}(V)$ are the functions which describe the currents relating to the spiking- and repolarization-phases of each spike, respectively. In this model we set the parameter γ equal to dt / C, where dt denotes the integration time-step size. Following [48], we defined the spike-generating function by a quadratic function:

$$f_{sp}(V) = \frac{g_L}{2\Delta_{th}}(V - V_{th})^2 + I_L - I_{th} \tag{4}$$

where Δ_{th} denotes the spike slope factor, and I_{th} the threshold current which corresponds to the voltage threshold V_{th}. After generating a spike, the original quadratic I&F models, for example [48,50], use a reset of V while we use here a repolarization function which exerts an instantaneous repolarization that lasts for one time bin dt; the resulting intrinsic continuity in the membrane potential renders our spiking model non-hybrid. We formulate this function as a combination of a delta-like Gaussian and a steep sigmoid function:

$$G_{rep}(V) = \frac{a_{rep}}{\sigma_{peak}\sqrt{\pi}} \exp\left(-\left(\frac{V - V_{peak}}{\sigma_{peak}}\right)^2\right) \tag{5}$$

$$f_{rep}(V) = \frac{\overline{I}_{rep}}{1 + \exp(-b_{rep}(G_{rep}(V) - c_{rep}))} \tag{6}$$

where a_{rep}, σ_{peak}, b_{rep} and c_{rep} denote the generic shape parameters of these functions, V_{peak} denotes the height of the spike's peak, and $\overline{I}_{rep}$ denotes the size of the following repolarization after each spike. In our parameterization for this model, the value assigned to $\overline{I}_{rep}$ shifts the

PLOS | COMPUTATIONAL BIOLOGY

membrane potential to more negative voltages than the resting potential V_{rest} to model the hyperpolarization-phase of the spike. The QGIF model (also its bursting version; see below) is able to exhibit reasonable neuronal responses to both constant and fluctuating (synaptic) inputs. Fig 1B shows the response of this model to a sustained applied current.

Bursting-Quadratic-Gaussian Integrate-and-Fire model (bursting-QGIF). Many neurons fire bursts of spikes, for a review see [51]. The bursts are thought to play an important role in neural information transmission [28,51–54]. These firing patterns may also be intermixed by those of repetitive single spikes [28]. In this work, we aim at the precise reconstruction of the within-burst spikes from fluorescence traces. As a representative, we will demonstrate such reconstruction for the somatic bursts of hippocampal pyramidal neurons [28–30,55]. To do this, we require a model with low complexity (for inversion) but coverage of the important biophysics of these neurons. For this purpose, we adapted the QGIF model of the previous section to derive a bursting-QGIF model by incorporating the non-inactivating muscarinic-sensitive (M-type) K^+ and persistent Na^+ currents (I_M and I_{NaP}, respectively). The contribution of these currents to bursting activity of hippocampal pyramidal neurons has been already reported [56–59]. In brief, the slow activation of I_M during the bursting period is likely to be involved in the burst termination, and the increase of I_{NaP} can give rise to bursts as well as an increase in the number of spikes per burst. We followed [57] for both formulating and setting the parameters of these currents. Overall, the current balance equation for the bursting-QGIF model is given by:

$$C\frac{d}{dt}V = I - I_L - I_{NaP} - I_M + f_{sp}(V) - \frac{f_{rep}(V)}{\eta}$$

$$\frac{dz}{dt} = \frac{z_\infty - z}{75}$$

$$I_{NaP} = g_{NaP} r_\infty(V)(V - E_{Na}) \tag{7}$$

$$I_M = g_M z(V - E_K)$$

$$r_\infty = 1/\left(1 + \exp\left(-\frac{V+41}{3}\right)\right)^{-1}$$

$$z_\infty = 1/\left(1 + \exp\left(-\frac{V+39}{5}\right)\right)^{-1}$$

where z_∞ and r_∞ denote the steady-state activation values for gating variables of I_M and I_{NaP}, and E_K and E_{Na} (resp. g_M and g_{NaP}) denote the reversal potentials (resp. the maximal conductances) of these currents. The slow gating variable z is the probability of activation of I_M. Note that the inference may assign negative values to this variable; this would lack physical meaning. In order to constrain the solution, without qualitatively changing the dynamics, we reformulate

PLOS | COMPUTATIONAL BIOLOGY

the model using a first-order Euler method, see also [60]:

$$z^{aux}(t+dt) = z^{aux}(t) + \frac{dt}{75} \times \frac{z_\infty(V(t)) - z(t)}{z(t) - z^2(t) + O}$$

$$z(t) = 1/(1 + \exp(-z^{aux}(t))) \tag{8}$$

$$I_M(t) = g_M z(t)(V(t) - E_K)$$

where we expressed the dynamics of the gating variable z in terms of the variable z^{aux} to constrain z to the interval [0,1], thereby providing biophysically interpretable states for the activation of I_M. Parameter O can be set properly to retain numerical stability. Furthermore, the bursting-QGIF model can account for a variety of firing patterns which were reported by previous electrophysiological experiments, for example [30,37,56,57,59]. Fig 1C shows a typical bursting voltage trace of this model when stimulated by a sustained applied current. In Fig 2, we provide a more detailed assessment of this model.

Calcium dynamics

Calcium channels. Voltage-gated calcium channels have been categorized into high- and low-voltage-activated (HVA and LVA, respectively) channels [61], for a review see [1]. Unlike LVA (T-type) calcium channels, somatic calcium transients due to spikes are known to be largely mediated by HVA calcium channels (L-, N-, P/Q-, and R-type) whose activation threshold is considerably more positive than typical resting membrane potentials [5,62]. Importantly, it has been found for hippocampal CA3 neurons that L-type calcium channels are predominantly localized in somata, and have a major role in somatic calcium transients [63]. In our experiment the region of interest for extracting the fluorescence traces was also restricted to cell bodies. In addition, previous studies reported that in recorded fluorescence traces there is nearly no evidence for subthreshold fluctuations in the membrane potential [5]. Consequently, we assumed that the recorded fluorescence transients relate to the surge of Ca^{2+} through L-type channels. To model these channels, we followed [64], as the underlying mechanisms in the chosen parameter regime (see Table 1) are comparable to the Cav 1.2 and Cav 1.3 forms of the L-type calcium channels [65]. In addition, the model has less complexity as compared to other models proposed for L-type calcium channels; for a review see [66]. Overall, this model [64] formulates the calcium current, I_{Ca}, across the membrane as:

$$I_{Ca} = g_{Ca} s_\infty (V - E_{Ca}) \tag{9}$$

where g_{Ca} and E_{Ca} denote the corresponding maximal conductance and reversal potential, respectively. The steady-state voltage-dependent activation of this channel, s_∞, is described by the Boltzmann function (see also [64,67]):

$$s_\infty(V) = (1 + \exp(-(V - V_{1/2})/\rho))^{-1} \tag{10}$$

which is characterized by a half-activation voltage, $V_{1/2}$, and a slope factor, ρ. This model formulates I_{Ca} as a non-inactivating current whose activation is an instantaneous function of the membrane potential.

Eqs 9 and 10 are based on the biophysical ranges of the membrane potential. However according to the parameter regime of the FHN model (see Table 1) each full spike in this model has a peak and undershoot of 2 and -2, respectively. Therefore, the voltage will be scaled as: $\iota_1 V - \iota_2$, where we set $\iota_1 = 30$ and $\iota_2 = 40$. Note that the QGIF models are already in a

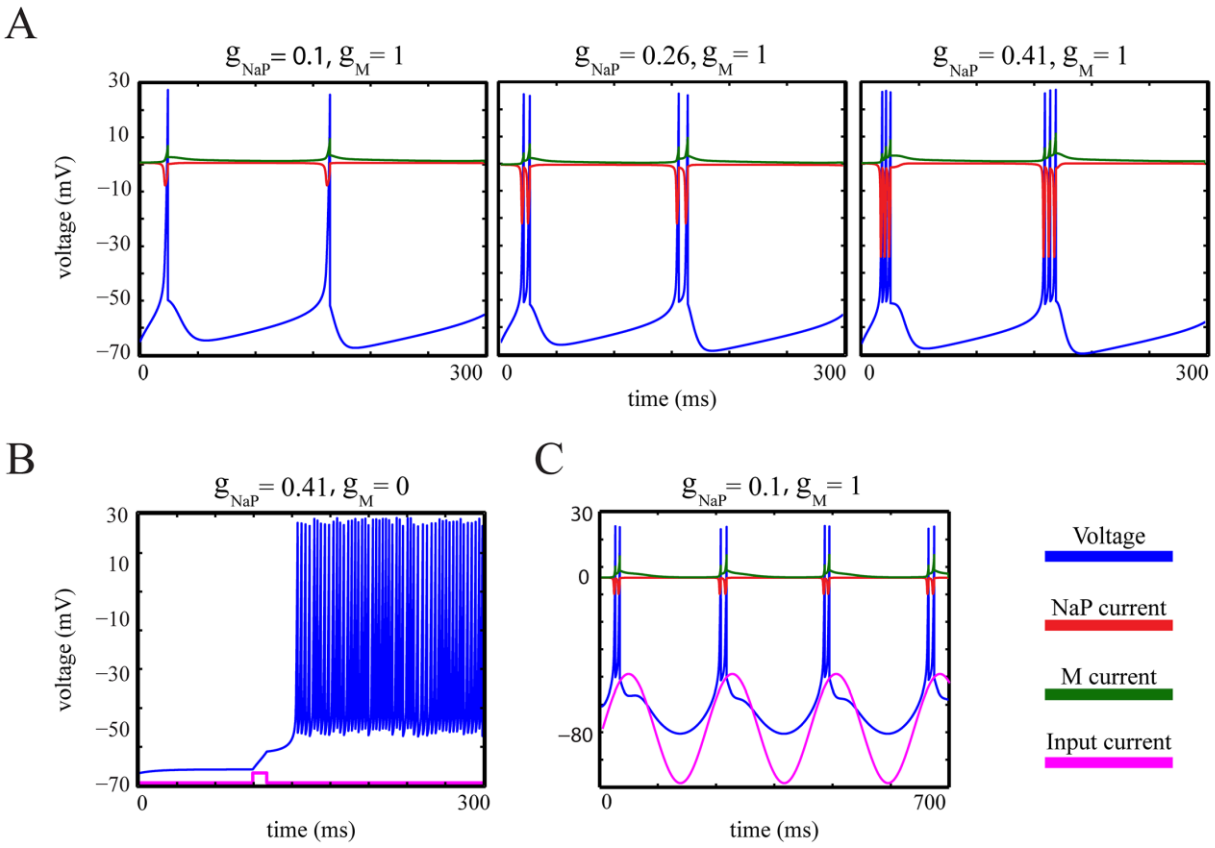

Fig 2. Assessment of biophysical aspects of the bursting-QGIF model. (**A-C**) Simulated voltage traces of the bursting-QGIF model in response to (**A**) sustained (not shown) and (**B**) brief square (magenta line) positive current pulses, and (**C**) a sinusoidal input current (magenta line). (**A**) The increment in persistent Na^+ current enhances the burstiness, similarly to [57]: As g_{NaP} increases, the number of spikes within each burst is increased, and the interspike intervals become shorter. Note that as expected biophysically the model exhibits a tonic repetitive spiking pattern for weak g_{NaP} densities. (**B**) M-type K^+ current governs the recovery mechanism for membrane potential, similarly to [57]: Blocking the M-type K^+ channel by setting $g_M = 0$ leads to a prolonged burst in response to a short-duration depolarized current pulse (magenta line). This indicates that the activation of this channel is important for terminating the bursts. (**C**) The bursting-QGIF model is selective in the input slope, similarly to [53]: the periodic burst response of the model to a sinusoidal input current shows that the burst are mainly initiated on the positive slope of the input (magenta line) thus signalling the input slope. The conductances and currents across **A-C** are in units of $[mS/cm^2]$ and $[\mu A/cm^2]$, respectively; input currents are in arbitrary units. Parameters for the simulation: (**A-C**) $\bar{I}_{rep} = 80\ \mu A\ mS/\mu F$, (**A**) $I_{app} = 1$, (**B**) $I_{app} = 0.6$, (**C**) $I_{app} = 2.5\sin(0.03t)\ \mu A/cm^2$. See Table 1 for the rest of parameter values.

doi:10.1371/journal.pcbi.1004736.g002

biologically plausible range; for example, in the QGIF model each spike has a peak around 30 mV followed by a hyperpolarization at around -80 mV.

$[Ca^{2+}]$ kinetics. The equation of $[Ca^{2+}]$ kinetics is given in [68] as:

$$\frac{d}{dt}[Ca^{2+}] = -\kappa_{Ca} I_{Ca} - \frac{[Ca^{2+}] - [Ca^{2+}]_{base}}{\tau_{Ca}} \tag{11}$$

where the opening of the calcium channels elevates the cytosolic $[Ca^{2+}]$ using entry via I_{Ca}, which subsequently decays back down to its basal concentration, $[Ca^{2+}]_{base}$, by time-constant τ_{Ca}. Parameter κ_{Ca} converts the calcium current to calcium concentration (per time unit), and also scales the amplitude of the calcium transient during the activation of the channel. The

PLOS | COMPUTATIONAL BIOLOGY

Table 1. Parameter values.

Models	Parameters	Units	References
QGIF family	$V_{th} = -59.9$	*mV*	[48]
	$I_{th} = 0.16$	$\mu A / cm^2$	[48]
	$g_L = 0.1$	mS / cm^2	[48]
	$C = 1$	$\mu F / cm^2$	[48]
	$V_{peak} = 30$	*mV*	[29]
	$\sigma_{peak} = 1$	*mV*	
	$a_{rep} = 10^{12}$	*mV*	
	$b_{rep} = 10^4$		
	$C_{rep} = 0.1$		
QGIF	$\bar{I}_{rep} = 120$	$\mu A\ mS / \mu F$	
	$\Delta_{th} = 3.48$	*mV*	[48]
	$dt = 0.2$	*ms*	[21]
	$k = 3$ **[INV]**		
	$\Upsilon_F = 3$ **[INV]**		
	$\Upsilon_V = 0.005$ **[INV]**		
	$\Upsilon_{Ca} = 10$ **[INV]**		
	$\tau_{Ca}^{real} = 2000$ **[SIM]**	*ms*	
	$\tau_{Ca}^{real} = 7500$ **[INV]**	*ms*	
bursting-QGIF	$\bar{I}_{rep} = 87$ **[SIM]**	$\mu A\ mS / \mu F$	
	$\bar{I}_{rep} = 80$ **[INV]**		
	$E_K = -90$	*mV*	[57]
	$E_{Na} = 55$	*mV*	[57]
	$g_M = 1$ **[U]**	mS / cm^2	[57]
	$g_{NaP} = 0.41$ **[SIM] [U]**	mS / cm^2	[57]
	$\Delta_{th} = 3.48$ **[SIM] [U]**	*mV*	[48]
	$O = 0$		
	$dt = 0.05$	*ms*	
	$k = 8$ **[INV]**		
	$\Upsilon_F = 6$ **[INV]**		
	$\Upsilon_V = 0.005$ **[INV]**		
	$\Upsilon_z = 20$ **[INV]**		
	$\Upsilon_{Ca} = 10$ **[INV]**		
	$\tau_{Ca}^{real} \approx 800$ **[SIM]**	*ms*	
	$\tau_{Ca}^{real} = 850$ **[INV]**	*ms*	
FHN	$\psi_1 = 0.7$		[21]
	$\psi_2 = 0.8$		[21]
	$\lambda = 0.08$		[21]
	$dt = 0.2$	*ms*	[21]
	$k = 3$ **[INV]**		
	$\Upsilon_F = 3$ **[INV]**		
	$\Upsilon_V = 2$ **[INV]**		
	$\Upsilon_W = 30$ **[INV]**		
	$\Upsilon_{Ca} = 10$ **[INV]**		
	$\tau_{Ca}^{real} = 2000$ **[SIM]**	*ms*	
	$\tau_{Ca}^{real} = 7500$ **[INV]**	*ms*	
Calcium channel	$g_{Ca} = 5$	mS / cm^2	[29]

(*Continued*)

Table 1. (*Continued*)

Models	Parameters	Units	References
	$\kappa_{Ca} = 0.002$ **[SIM] [U]**		[64]
	$[Ca^{2+}]_{base} = 0$ **[SIM] [U]**		
	$E_{Ca} = 120$	*mV*	[64]
	$\rho = 5$	*mV*	[64]
	$V_{1/2} = -25$ **[SIM]**	*mV*	[64]
	$V_{1/2} = -45$ **[INV]**	*mV*	[67]
Ca^{2+} -fluorescence mapping	$K_d = 200$ **(for OGB-1)**	*nM*	[4]
	$\kappa_F = 10$ **[U] (for QGIF)**		
	$\kappa_F = 5$ **[U] (for bursting-QGIF & FHN)**		
	$d_F = 0$ **[U]**		
Precision-parameters	$\sigma = \text{inf} \approx 10^{12}$ **[SIM] [U]**		
	$\alpha = \text{inf} \approx 10^{12}$ **[SIM] [U]**		

Parameter values used in the generative and inverse models. This table lists the default values of modeling parameters. The abbreviations **SIM** and **INV** in front of the parameter values (second column) indicate that these values were used in the simulations and inversions, respectively. The parameters designated by **U** were considered as free parameters in the inversions and thus need to be inferred from the data; the prior distributions for these parameters are listed in Table 2. Moreover, for simulating data the initial conditions of all neuronal dynamics were set to their steady-states in the absence of input to neuron model. The rest of parameters were kept with the same values in both simulations and inversions. All parameter values are consistent across the figures, unless stated otherwise.

doi:10.1371/journal.pcbi.1004736.t001

negative sign of I_{Ca} renders it an inward current. Note that the decay kinetics of the calcium transient reflect the decline in $[Ca^{2+}]$ as a result of different pumping and buffering mechanisms; for a review see [1].

The observation model

The transformation between $[Ca^{2+}]$ kinetics and fluorescence responses can be described by a saturating Hill-type function [19,69,70]:

$$g([Ca^{2+}]) = F_t = \kappa_F \frac{[Ca^{2+}]}{[Ca^{2+}] + K_d} + d_F \tag{12}$$

where κ_F and d_F are scale and offset parameters for the fluorescence trace and parameter K_d is the so-called dissociation constant [26], a quantitative measure of the affinity of the fluorescent indicator to calcium.

In practice, for each fluorescence trace, we estimate the measurement SNR by dividing the minimum amplitude of the fluorescence transient by the standard deviation (std) of the baseline fluorescence, similarly to [19,69,71].

Summary: The full generative model

In brief, each generative model (Eq 1) is a combination of the equations for a spiking model, the HVA calcium channel (Eqs 9 and 10), $[Ca^{2+}]$ kinetics (Eq 11), and the observation (Eq 12). As spiking models we use the FHN model, (Eq 2), and the family of differentiable integrate-and-fire models, for single spikes (QGIF, Eqs 3–6), and spike bursts (bursting-QGIF, Eqs 4–7), see also Table 3 for an overview. The parameter values for all models have been summarized in Table 1, or are indicated in the figure captions of the Results section below. More details are available in the S1 Appendix.

PLOS | COMPUTATIONAL BIOLOGY

Bayesian inference

This section describes the main concepts of the VB-Laplace method, a Bayesian inference method for stochastic nonlinear state-space models [31]. The inference is based on a probabilistic generative model which quantitatively describes how observed data are generated. For a given generative model, say model m and data time series y_t, the task is to infer the moments of the posterior (the so-called conditional) distributions $p(\upsilon|y_t,m)$ for the parameters/variables of interest $\upsilon = \{x_t,\varphi,\theta,\alpha,\sigma\}$ (see Eq 1), by using variational Bayes [72]. In this method the moments of the posterior distribution (conditional mean μ and covariance Σ) are updated iteratively by optimizing a free-energy lower bound, $F(q,y_t)$, on the log-evidence (i.e. the logarithm of the model evidence) with respect to an approximate posterior density, $q(\upsilon)$. The free energy is the difference between the Kullback-Leibler divergence (denoted by $D_{KL}(\cdot||\cdot)$) of true and approximate posterior densities, and the log-evidence [72]:

$$F(q, y_t) = \ln p(y_t|m) - D_{KL}(q(\upsilon)||p(\upsilon|y_t, m)) \tag{13}$$

Variational Bayes aims at minimizing the Kullback-Leibler divergence so that the approximations to both posterior $p(\upsilon|y_t,m)\approx q(\upsilon)$ and log-evidence $\ln p(y_t|m) \approx F(q,\upsilon)$ become analytical (i.e. can be computed iteratively in a computationally efficient fashion). This minimization is equal to maximizing the free-energy, with respect to $q(\upsilon)$. Note that the divergence is a non-negative value (thus, the free-energy is a lower bound on the log-evidence), and $q_{\text{exact}}(\upsilon) = p(\upsilon|y_t,m)$. The VB-Laplace method [31] inverts the generative model under two simplifying assumptions: (i) a mean-field separability assumption [73] which factorizes the $q(\upsilon)$ into the product of approximate marginal posterior densities, over the model unknown quantities (i.e. υ), and (ii) a Laplace approximation whereby each of these marginal densities (except those for precision-parameters) is approximated by a Gaussian density, namely $q(\upsilon_i) \approx N(\mu_{\upsilon_i}, \sum_{\upsilon_i})$. The first assumption facilitates the iterative maximization of free energy, and the latter finesses the analytical intractability problem of the inference; this problem arises from the nonlinearities in the likelihood (i.e. observation) functions. To update the marginal densities, the VB-Laplace method uses an iterative regularized Gauss-Newton scheme [74]. The precision-parameters are updated without requiring the Laplace approximation. Furthermore, the update rules of the hidden states exploit a variational Bayesian Laplace treatment of the extended Kalman-Rauch filter/smoother. Conceptually, given the full data time series, these probabilistic filters evaluate the approximate marginal posterior density on the hidden-states time point by time point, i.e. $q_i(x_t|y_{1:T})$, instead of capturing the full joint density over the whole time series, i.e. $q_i(x_{1:T}|y_{1:T})$. Therefore, the VB-Laplace method can control the lagged Kalman forward pass [31,75] by specifying to what extent this lag, k, is going to be applied. That is, for time t, this scheme approximates the lagged posterior density, $p_i(x_t|y_{1:t+k},m)$, by making inference on hidden-state at the current time, i.e. x_t, after observing all data up to time $t + k$, i.e. $y_{1:t+k}$. This step should (in general) improve the precision and the temporal smoothness of the inference on the hidden states. For full details of the VB-Laplace method we point the interested reader to [31,60].

All Bayesian inference procedures described in this study have been implemented as Matlab (MathWorks) code in the VBA toolbox (http://mbb-team.github.io/VBA-toolbox/) developed by Jean Daunizeau and colleagues.

Experimental methods

The experimental data recorded in our lab were six *in vitro* fluorescence traces for which simultaneous electrophysiological recordings (thus, veridical spike times) were also acquired.

Preparation of acute brain slices

All experimental procedures were carried out with approval by the local government and complied with international and European Union norms. Experiments were performed on acute brain slices prepared from C57BL/6J mice at postnatal day (P) 3–4 (P0 –day of birth). Animals were decapitated under deep isoflurane anesthesia. The brain was removed quickly and transferred into ice-cold saline containing (in *mM*): 125 NaCl, 4 KCl, 10 glucose, 1.25 NaH_2PO_4, 25 $NaHCO_3$, 0.5 $CaCl_2$, and 2.5 $MgCl_2$, bubbled with 5% CO_2/95% O_2 (pH = 7.4). Horizontal slices (350 μm) comprising the CA3 region of the hippocampus were cut on a vibratome (VT1200 S, Leica) and stored for at least 1h before use at room temperature in artificial cerebrospinal fluid (ACSF) containing (in *mM*): 125 NaCl, 4 KCl, 10 glucose, 1.25 NaH_2PO_4, 25 $NaHCO_3$, 2 $CaCl_2$, and 1 $MgCl_2$, bubbled with 5% CO_2/95% O_2 (pH = 7.4).

Simultaneous confocal Ca^{2+} imaging and electrophysiological recordings

For recordings, slices were placed into a submerged-type recording chamber on the stage of an Eclipse FN1 microscope (Nikon). Cells were loaded with the AM-ester of the Ca^{2+} indicator Oregon Green 488 BAPTA-1 (OGB1, 340 μM) by pressure-ejection (30 *s*) from a glass pipette (3–6 $M\Omega$) [76]. Fluorescence traces were acquired using a 16×/0.8 NA water-immersion objective (Nikon) at a frame rate of 22.6 *Hz* using a CSU10 Nipkow-disc scanning unit (Yokogawa) and a Rolera-XR camera (QImaging) controlled by the software Streampix 5 (Norpix). Excitation light at 488 *nm* was provided by a single wavelength solid-state laser (Sapphire CDRH-LP, Coherent). Electrophysiological signals were acquired using a Multiclamp 700B amplifier, a 16-bit AD/DA board (Digidata 1440A) and the software pClamp 10.4 (Molecular Devices). Signals were low-pass filtered at 3 *kHz* and sampled at 20 *kHz*. Loose-patch (seal resistance < 1 $G\Omega$) or tight-seal cell-attached recordings from cells in stratum pyramidale of the CA3 region were performed in voltage-clamp mode using borosilicate glass pipettes (8–12 $M\Omega$) filled with 154 *mM* NaCl. Alexa Fluor 488 (25–75 μM) was frequently added for pipette visualization. Holding current was manually zeroed prior to each experiment. Brief LED light pulses were used to synchronize optical and electrophysiological signals. All experiments were performed at 32–34°C at an ACSF flow rate of ~3 ml min^{-1}.

Extraction of fluorescence traces

We extracted the "somatic" fluorescence traces from a set of fluorescence image sequences recorded from the hippocampal CA3 neurons (see previous section); Fig 3A depicts the mean frame of one of the recorded image sequences for the whole field of view. We then converted the traces to the relative fluorescence changes ($F_t = \Delta F / F_0$) after subtraction of its resting (prestimulus) intensity level, F_0 [77].

Temporal drifts

A preliminary analysis of the recorded fluorescence traces (see Experimental methods) showed strong evidence of temporal low frequency drifts, which might be attributed to, for example, mechanical movements or photobleaching. In particular, we found (downward) drifts in the data lasting several hundred seconds (see Fig 3B, blue trace). This is far beyond the plausible ranges of calcium decay time-constants. Such low-frequency drifts have often been reported in time series of ECG and fMRI data, for example [78–80]. These drifts have commonly been treated as confounds, for example [81], because they can induce pronounced autocorrelation in the residual noise structures [82]. This autocorrelation may in turn decrease inference accuracy. Therefore,

PLOS | COMPUTATIONAL BIOLOGY

several methods have been suggested to remove low frequency drifts prior to analysis, for example [78,83]. Here, we decided to apply a fourth degree polynomial detrending method [78,84] to the fluorescence traces. Details for this method can be found in the S2 Appendix.

Membrane potential thresholding

To extract the onset times of reconstructed firing events by the QGIF and FHN models (see Results), we threshold the inferred membrane potentials. For simplicity, we use as voltage threshold (which we used as spike detection threshold) the value zero. After a threshold event, we also discount any other threshold passing from negative to positive for the next 6 *ms* to prevent false spike detection from potential high frequency fluctuations in the inferred membrane potentials.

Prior distributions

The Bayesian approach allows us to specify prior distributions to quantities of the generative model. Following [31], Gaussian prior distributions are assumed on both the evolution and observation parameters, and the initial conditions of hidden states. Each Gaussian prior is defined by its mean, μ, and covariance, Σ; the mean determines the prior expectation, and the covariance embodies the prior beliefs or information about the quantities of interest:

$$p(\theta|m) = N(\mu_\theta^0, \sum_\theta^0)$$

$$p(\varphi|m) = N(\mu_\varphi^0, \sum_\varphi^0) \tag{14}$$

$$p(x_0|m) = N(\mu_{x_0}^0, \sum_{x_0}^0)$$

where the upper index 0 denotes these moments belong to prior distributions. Moreover, the form of the evolution and observation equations (note the Gaussian state- and measurement-noises in Eq 1) yields the Gaussian transition and likelihood densities, respectively:

$$p(x_{t+1}|x_t, \theta, \alpha, m) = N(f(x_t, \theta, u_t), (\alpha\Upsilon_x)^{-1})$$

$$p(y_t|x_t, \varphi, \sigma, m) = N(g(x_t, \varphi, u_t), (\sigma\Upsilon_y)^{-1}) \tag{15}$$

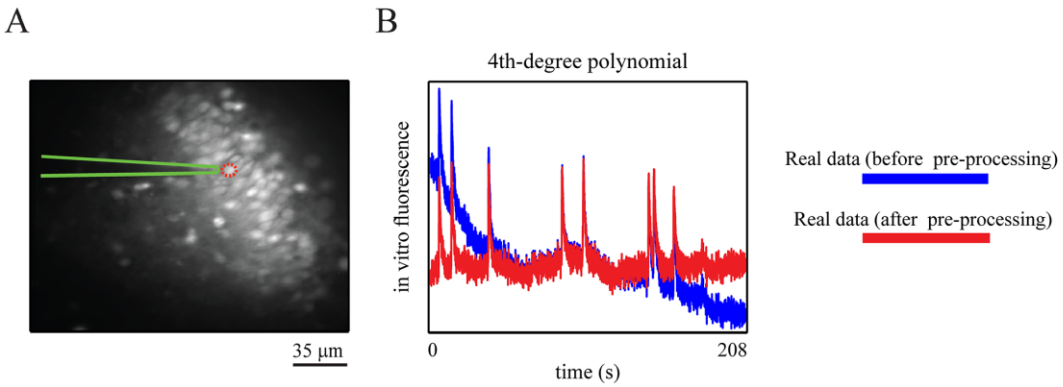

Fig 3. Field of view and low frequency temporal drifts. (**A**) Sample average (over frames) Oregon Green BAPTA 1 (OGB-1) fluorescence image of a neuronal population from the CA3 area of a hippocampal slice. (**B**) An *in vitro* OGB-1 fluorescence trace before (blue line) and after (red line) removal of its slowly varying components, by using the fourth degree polynomial detrending method.

doi:10.1371/journal.pcbi.1004736.g003

PLOS | COMPUTATIONAL BIOLOGY

Hence, the mean and variance of the prior distribution on hidden states and observations can be assigned through the definition of the evolution and observation functions, and precision quantities. In addition, Gamma priors are used on precision-parameters, where each distribution is parameterized by its shape, a, and rate, b, parameters:

$$\begin{aligned} p(\alpha|m) &= Ga(a_\alpha^0, b_\alpha^0) \\ p(\sigma|m) &= Ga(a_\sigma^0, b_\sigma^0) \end{aligned} \tag{16}$$

Parameters of interest

In the present models, there are five subsets of parameters: (i) calcium-dynamics-modulating parameters, (ii) membrane-potential-modulating parameters, (iii) initial conditions, (iv) observation parameters, and (v) precision-parameters. In the following, we motivate our choices for the prior distributions of these parameters. Not unexpectedly and due to the temporal smoothness of the fluorescence transients, our preliminary analyses revealed that the biophysical models are rather too complex and potentially over-fitting the data. To avoid over-parameterization, we therefore fixed several parameters to physiologically plausible values. Operationally, for a fixed parameter we set its prior variance equal to zero. This effectively prevents updating of the parameter in the VB-Laplace method. To fit the data, we kept those parameters free which influenced the kinetics of the fluorescence transients as these parameters may be inferred from the data. In the following, we will specify which parameters are fixed for the five different model components (see Table 1 for the parameter values):

(i). Calcium-dynamics-modulating parameters control the dynamics of HVA calcium channel's gating variable and current (Eqs 9 and 10), as well as the kinetics of Ca^{2+} concentration (Eq 11). Specifically, we fixed parameters ρ, $V_{1/2}$, E_{Ca}, and g_{Ca}. As free parameters, we used τ_{Ca}, κ_{Ca}, and $[Ca^{2+}]_{\text{base}}$. Note that as both g_{Ca} and κ_{Ca} have in Eq 11 the same effect on scaling the calcium transients we fix g_{Ca}.

(ii). Membrane-potential-modulating parameters control the dynamics of membrane potential, refractoriness, and activation of the voltage-gated ion channels. Importantly, selection of inappropriate parameter regimes may preclude firing of the neuron, or trap it in a biologically meaningless state. Therefore, we fix most of these parameters in order to retain their potential physiological meanings. However, for inverting the bursting-QGIF model for data with near-millisecond resolution, we use Δ_{th}, g_M, and g_{NaP} as free parameters. These, in principle, can take part in shaping of spike-evoked calcium transients (see Results). In particular, by keeping g_M and g_{NaP} as free parameters the model will have access to a wide range of different firing regimes. It is an open and interesting question whether these parameters can be inferred from the data, e.g. at a high temporal resolution (see Results).

(iii). Prior means for initial conditions were set to their steady-state values in the absence of any input current to the neuron, i.e. when the neuron is "at rest". We allowed the VB-Laplace method to estimate the initial values of the neuronal dynamics from the onset of fluorescence traces by keeping these as free parameters.

(iv). Observation parameters control the mapping of $[Ca^{2+}]$ kinetics on to fluorescence traces. We fix K_d and keep only κ_F and d_F as free parameters. We specify tighter priors on these parameters in favor of the parameters of interest listed under (i). This is because parameters κ_F and κ_{Ca} (and g_{Ca}), as well as K_d all effectively scale the fluorescence transients [19,69]. Similarly, both d_F and $[Ca^{2+}]_{\text{base}}$ can set the offset of fluorescence trace [19]. However, our preliminary results showed that using κ_F and d_F as free parameters

PLOS | COMPUTATIONAL BIOLOGY

increased the robustness of the inference with respect to adverse conditions such as low SNR and rather variable amplitudes of the transients.

(v). Precision-parameters control the level of synaptic input to the membrane, and the noise on gating variables, recovery variable, $[Ca^{2+}]$ kinetics, and fluorescence traces. This noise level can differ, for example, among different experimental conditions. Therefore, precision-parameters need to be inferred from the data. To do so, it is sufficient to make inference about either the precision-parameters (i.e. α and σ) or the inverse covariance matrices (i.e. Υ_x and Υ_y), see Eq 1. Following [31,60] we kept the precision-parameters free, while the inverse covariance matrices are fixed with constant values. We defined Υ_x as a diagonal matrix and Υ_y as a scalar whose values are constant for the whole time series.

In summary, we specify prior distributions on initial conditions, six evolution parameters $\theta = \{\kappa_{Ca}, \tau_{Ca}, [Ca^{2+}]_{base}, \Delta_{th}, g_M, g_{NaP}\}$, two observation parameters $\varphi = \{\kappa_F, d_F\}$ and precision-parameters $\{\alpha, \sigma\}$. The prior distributions are listed in Table 2. To ensure the positivity of the evolution parameters (except $[Ca^{2+}]_{base}$; see the S1 Appendix) and the observation scaling parameter (i.e. κ_F) we re-parameterized them as $\theta_i = \theta_i^0 \exp(\chi_i)$ and $\kappa_F = \kappa_F^0 \exp(\chi_{\kappa_F})$, see also [60]. That is, we estimate the posterior distribution over, e.g., parameter θ_i under Gaussian prior assumption on its modal parameter χ_i; thus $p(\chi_i) = N(\mu_{\chi_i}^0, \nu_{\chi_i}^0)$. $\mu_{\chi_i}^0$ and $\nu_{\chi_i}^0$ are the prior mean and variance of χ_i. Accordingly, we set $\mu_{\chi_i}^0 = 0$, while prior knowledge about the prior expectation of the parameter will be effectively embodied in the value of θ_i^0.

To assign a proper prior to calcium decay time-constant, we consider the following relationship:

$$\tau_{Ca}^{frame} \exp(\chi_{\tau_{Ca}}) \times dt^{frame} = \tau_{Ca}^{real} \times dt \tag{17}$$

Table 2. Prior densities.

Models	Parameters	Prior densities
All	$\tau_{Ca} = \tau_{Ca}^0 \exp(\chi_{\tau_{Ca}})$	$\chi_{\tau_{Ca}} \sim N(0,5)$
	$\kappa_{Ca} = 0.002 \exp(\chi_{\kappa_{Ca}})$	$\chi_{\kappa_{Ca}} \sim N(0,5)$
	$[Ca^{2+}]_{base}$	$[Ca^{2+}]_{base} \sim N(0.100)$
	$[Ca^{2+}](0)$	$[Ca^{2+}](0) \sim N([Ca^{2+}]^{ss}\|_{V_{1/2}\ \ 45}, 25)$
	$\kappa_F = 5 \exp(\chi_{\kappa_F})$	$\chi_{\kappa_F} \sim N(0,1)$
	d_F	$d_F \sim N(0.5\min(F_t), 0.25)$
	α	$\alpha \sim Ga(1,1)$
	σ	$\sigma \sim Ga(1,1)$
QGIF	$V(0)$	$V(0) \sim N(V^{ss}, 100)$
Bursting-QGIF	$\Delta_{th} = 3.48 \exp(\chi_{\Delta_{th}})$	$\chi_{\Delta_{th}} \sim N(0,1)$
	$g_{NaP} = 0.41 \exp(\chi_{g_{NaP}})$	$\chi_{g_{NaP}} \sim N(0,1)$
	$g_M = \exp(\chi_{g_M})$	$\chi_{g_M} \sim N(0,1)$
	$V(0)$	$V(0) \sim N(V^{ss}, 100)$
	$z(0)$	$z(0) \sim N(z^{ss}, 1)$
FHN	$V(0)$	$V(0) \sim N(V^{ss}, 4)$
	$W(0)$	$W(0) \sim N(W^{ss}, 1)$

Prior densities of the free (i.e. unknown) parameters. *N*(mean,variance) indicates normal distribution, and *Ga*(shape, rate) indicates a Gamma distribution. The superscript *ss* denotes the steady-state value of the corresponding variable in the absence of input to neuron model. The proper values for τ_{Ca}^0 (in terms of τ_{Ca}^{real}) can be found in Table 1.

doi:10.1371/journal.pcbi.1004736.t002

PLOS | COMPUTATIONAL BIOLOGY

Table 3. Generative models.

		Spiking models		Calcium channel		[Ca^{2+}] kinetics		Ca^{2+} -fluorescence mapping		Generative model's name
Eq 1	{	**QGIF** (Eqs 3–6)	+	Eqs 9–10	+	Eq 11	+	Eq 12	} =	**QGIF**
		Bursting-QGIF (Eqs 4–7)								**Bursting-QGIF**
		FHN (Eq 2)								**FHN**

Overview of the three generative models QGIF (Quadratic-Gaussian integrate-and-fire) model, bursting-QGIF model, and Fitzhugh-Nagumo (FHN) model, and the equations required for their construction. The three models only differ in the spiking model.

doi:10.1371/journal.pcbi.1004736.t003

where $\tau_{Ca}^{frame} = \tau_{Ca}^{0}$ is an a-priori specified value for τ_{Ca}, τ_{Ca}^{real} is the actual value of calcium decay time-constant in real time, dt^{frame} is the inverse sampling frequency (in $[ms]$), and dt is the integration time-step size of neuron dynamics (in $[ms]$). Eq 17 informs the generative model about the temporal precision of fluorescence data: the inversion operates on two different time scales simultaneously, a slow and fast relating to fluorescence traces (observation equation) and neural dynamics (evolution equations). The slow time scale evolves in an image frame resolution and the fast in a sub-millisecond resolution.

Note that most of the fixed parameters in both simulating and inverting tasks (Table 1), as well as the prior means for the free parameters (Table 2) were set to values according to previously reported modelling or experimental studies (e.g., see the "References" column in Table 1). See also the S1 Appendix for a more detailed explanation about our choices for a number of fixed parameters, like $V_{1/2}$ and $[Ca^{2+}]_{base}$.

Data simulation

To illustrate the method, we simulated the synthetic fluorescence traces using each of the FHN, QGIF and bursting-QGIF models, followed by inversion for each data set. For each model, the membrane was stimulated by a set of square pulses of depolarizing currents with various widths and strengths so that the spiking and/or bursting firing patterns were triggered. These traces were down-sampled at the desired frame rates (see Results). We added background noise, i.e. the trace recorded in the absence of fluorescence emission (when the laser was switched OFF), after scaling to the fluorescence traces in order to achieve the desired SNRs.

Scaling of fluorescence data

In this study, the fluorescence traces which we used as data had a range around 0.2 (for high SNR) $< \max(F_t) <$ 1 (for low SNR), with the baseline set to zero. For data within different ranges, one can use the priors used in this study, following by an automated normalization, see also [71], where first the baseline of the drift-corrected trace is set to zero, followed by a scaling: $F_t \leftarrow (scale \times F_t / \max(F_t))$, where $scale = 1$.

Alternative methods

We compare the spike reconstruction efficiency of our method to two different types of established spike reconstruction methods: 1) template matching [85], and 2) a deconvolution-based method [71].

For the first type, we used a widely-used template matching (TM) method using an optimally scaled template [85] implemented in the pCLAMP 10.2 software package (Molecular

Devices, Sunnyvale, CA, 2009). To perform the comparisons, we use two data sets with different types of, in particular, rise kinetics (i.e. fast or slow, see Results). In an initial, interactive phase we defined a distinct template for each data set, as follows. For data with slowly rising transients, we first extracted around twenty veridical fluorescence transients from the six *in vitro* low SNR fluorescence traces, recorded in our lab. After averaging these transients, which were evoked during synchronized network activities, we found that a two-term Boltzmann equation can be well fitted to this averaged (empirical) template (see Results). In a similar way, we defined a template for the data set with fast rising transients; namely, by averaging fifty-six veridical single-spike-evoked transients extracted from twelve adopted *in vitro* traces (see below), followed by fitting a two-term Boltzmann equation to the averaged transient. Accordingly, we adopted the fitted templates by the TM method in order to detect the spiking activities in fluorescence traces. For this method a threshold (Thr_{TM}) parameter for the detection-criterion needs to be set manually. In brief, this threshold embodies both the optimum scaling factor and the goodness of fit; for more detail see [85]. For each trace, we used four different thresholds as Thr_{TM} = 1, 1.5, 2 and 2.5. We then used the available joint electrophysiological and optical recordings in order to select the optimal threshold for each data set, separately (see Results). All these steps were carried out using pCLAMP 10.2.

As a deconvolution-based method, we used the fast filter technique [71] which is one the most well-established, probabilistic spike reconstruction methods. This method performs a fast nonnegative deconvolution of fluorescence traces in order to infer the most likely spike trains. It uses a first-order generative model: The calcium transients are generated through convolving the spikes, sampled from a Poisson distribution, with a decaying exponential. This model assumes an instantaneous rise time for each evoked transient, whose amplitude is linearly scaled by the number of spikes in a time frame. The generated $[Ca^{2+}]$ trace is converted to fluorescence intensities by using a linear (or saturating) mapping and adding Gaussian noise. Given the model and a fluorescence trace, the method aims to find the maximum a posteriori (MAP) spike train (the filter's output). Note that the computed MAP is an approximation to the actual MAP. This is because for the inversion the method replaces the Poisson distribution with an exponential distribution, due to analytical intractability issues. This approximation removes the integer constraint from the number of spikes, which had been primarily determined by the Poisson distribution. Consequently, an optimal detection threshold for the filter's output must be determined, in order to extract the best possible solution to the most likely spike train (see [71]). In other words, this thresholding is required for reporting the spike or event (single spike or burst) detection results. In our analyses, we were interested in quantifying the event, rather than individual spike detection errors (see Results). Accordingly, to make the comparison to the proposed method appropriate, when searching for an optimal threshold, we only counted the first inferred spike per event. For implementing this method we used available Matlab code (https://github.com/jovo/fast-oopsi/), with the parameter initializations performed as described in the main paper [71], including the sampling rate of the fluorescence data. More details about the method can be found in [71].

Results

In this section, we apply the proposed method to both synthetic data and *in vitro* fluorescence measurements. In particular, we use two *in vitro* data sets, which have been acquired simultaneously with electrophysiological recordings to validate the inferred spike times: 1) a data set of six joint transmembrane current and fluorescence traces (with slowly rising transients) recorded in our lab from neonatal CA3 neurons, and 2) a data set of twelve joint membrane potential and fluorescence traces (with fast rising transients) recorded for a previous study [71]

from juvenile layer V somatosensory cortex neurons (available at: https://github.com/jovo/fast-oopsi/tree/master/data/). For our approach, the values of all model parameters and their prior densities are summarized in Tables 1 and 2, unless stated otherwise in the figure captions.

For the sake of brevity, hereafter we refer to our approach (i.e. the combination of the VB-Laplace and our generative models) as "CaBBI"; an abbreviation of "*calcium* imaging analysis using *biophysical* models and *Bayesian inference*".

Synthetic data

In this section, we show the inversion results of the new approach for fluorescence traces simulated by the three different generative models (see Methods). More specifically, we will show that through making a reliable inference about the neuronal dynamics (like, membrane potential), our approach has the following central features:

1. It accurately reconstructs both single spikes and within-burst spikes from fluorescence transients with fast rise times (e.g. 3 *ms*). Such transients are typical for adult neurons and are the standard transient type considered in previously proposed spike/firing rate reconstruction methods, e.g. [17,19,71]; see also [86].
2. The method accurately reconstructs the single spikes from the transients even with "slow" rise kinetics (e.g. lasting 100 *ms* for a single-spike-evoked transient) as observed in the data from neonate hippocampal tissues [27], and in recordings with new genetically encoded calcium indicators [87–89]. To our knowledge, this is the first time that an (accurate) spike reconstruction approach, in practice, is applied to such data.
3. The method adapts to different kinetics of the spike-evoked fluorescence transients, for example with different rise times. This means that due to the biophysical constraints embodied by the generative model equations, the method does not require a training/conditioning or re-parameterization phase. This training step is typically performed by other methods, usually by using simultaneous optical and electrophysiological recordings, to constrain/set parameters and priors [5,13,25].
4. The method is robust against rather high levels of noise (i.e. low SNR condition). This is important because fluorescence traces with high temporal resolutions [13,90], or obtained from *in vivo* experiments [91], are usually acquired with relatively low SNR. This would mean that when using the proposed method, one can have, for example, both high temporal resolution and informative spike reconstructions.

Simulated single-spike-evoked transients (with fast rise times)

To show that our approach can accurately reconstruct spikes from fluorescence traces, we first applied it to simulated traces resembling the single-spike-evoked transients in adult neurons with fast rise kinetics.

The generated traces are shown in Fig 4 (first row) for the two non-bursting models, QGIF and FHN. We inverted these models for fluorescence traces containing the transients with fast rise times, i.e. less than 5 *ms* (thus, imaged within one frame in the given sampling frequency of 33.3 *Hz*). The fast rise kinetics are shown in zoomed-up, representative fluorescence transients in the last row of Fig 4. This figure shows that the neuronal dynamics can be inferred reasonably accurately, including the non-saturating $[Ca^{2+}]$ kinetics (third row) and membrane potentials (fourth row). Consequently, the spikes were detected accurately, as compared to simulated spikes (grey stars in fourth row). For data with high SNR this can be seen in Fig 4A and 4B; QGIF: SNR $\approx$ 30, number of veridical spikes (n) = 12, missed spikes (M) = 0 and falsely

PLOS | COMPUTATIONAL BIOLOGY

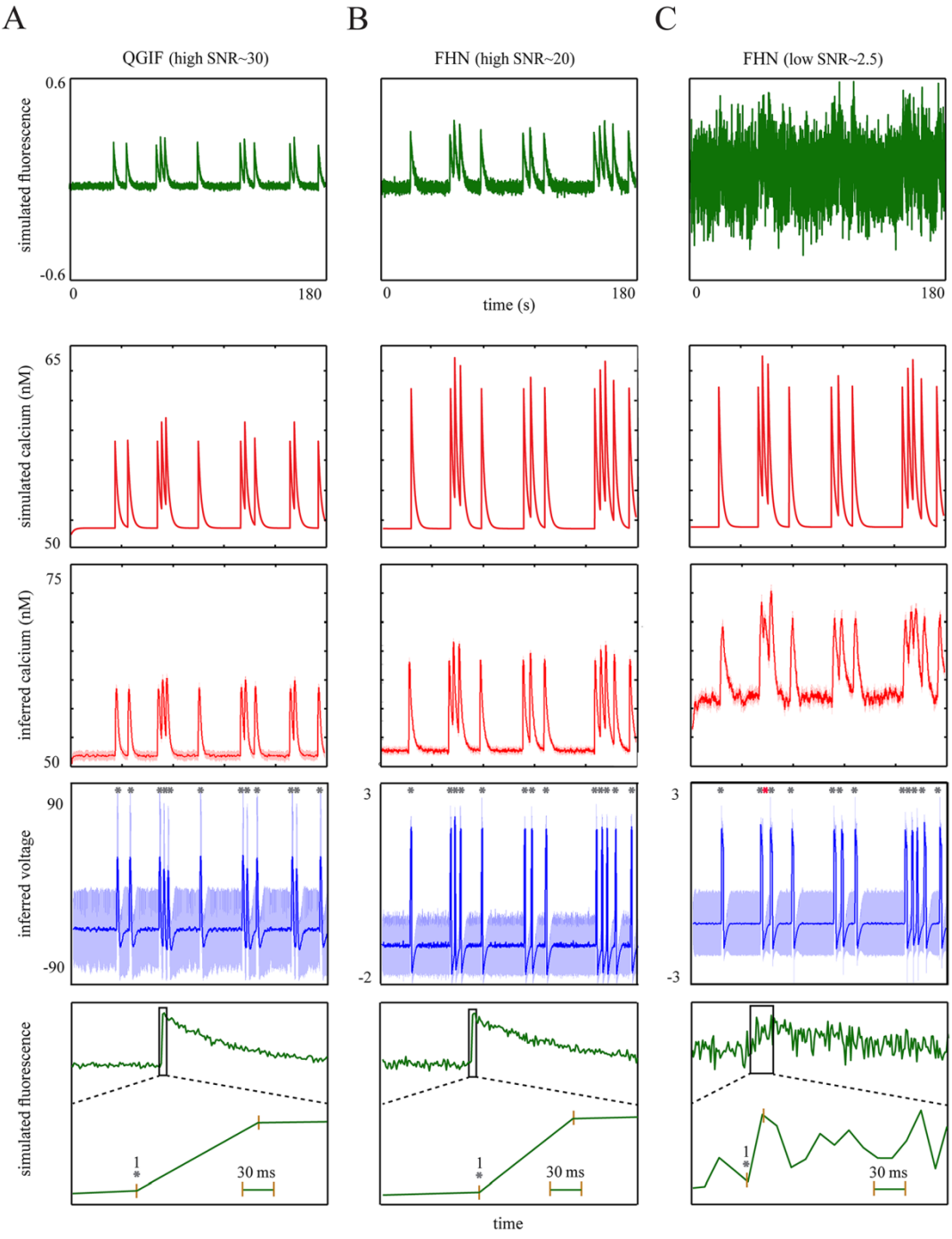

Fig 4. Results of the proposed approach for synthetic single-spike-evoked transients with fast rise times. (**A**): QGIF model, (**B**): FHN model with high SNR, (**C**): FHN model with low SNR. (**A-C**) Inferring neuronal dynamics from transients with fast rise times (e.g. 3 *ms*). The fluorescence traces (first row) and $[Ca^{2+}]$ kinetics (second row) were simulated by using (**A**) QGIF and (**B** and **C**) FHN generative models. Inverting each model for its corresponding trace by

PLOS | COMPUTATIONAL BIOLOGY

using CaBBI led to a reasonably accurate inference about the membrane potentials and non-saturating [Ca^{2+}] kinetics (rows four and three); 95% confidence intervals are shown as shaded areas. The inferred spikes (fourth row) coincide accurately with the veridical spikes (grey stars). The robustness of the method against high levels of noise is evident in the results shown in **C**, where only one spike was missed (red star). Fifth row shows the zoom into the rise time of a representative fluorescence transient in each trace shown in the first row. Membrane potential has the unit of [*mV*] in the (family of) QGIF model(s), but is dimensionless in the FHN model. The fluorescence traces were sampled at a frequency of 33.3 *Hz*. The values of parameters for the simulations and inversions can be found in Table 1, and prior distributions in Table 2. Units and conventions, as well as the parameter values are consistent across the following figures, unless stated otherwise.

doi:10.1371/journal.pcbi.1004736.g004

detected spikes (FD) = 0, FHN: SNR ≈ 20, n = 13, M = 0 and FD = 0. The uncertainty (shaded areas) was mainly elevated for near-rest membrane potentials. This is because we modeled only HVA calcium channels, which open mainly during spikes (see Methods). We also evaluated the inference under low SNRs, see Fig 4C. These low SNRs present a lower limit of the typical SNR expected in regular experimental setups. Fig 4C (fourth panel) shows that even for this low SNR (Fig 4C, first panel), the estimated spikes match accurately the true spikes (grey stars) and only one spike was missed (red star) (Fig 4C, fourth panel; SNR ≈ 2.5, n = 13, M = 1 and FD = 0). For the low SNR case the inferred non-saturating [Ca^{2+}] kinetics (Fig 4C, third panel) display a higher level of rest [Ca^{2+}] as compared to the true kinetics (Fig 4C, second panel). This indicates that CaBBI has optimized the fit by estimating larger values for basal calcium concentration. For this low SNR case we used only the FHN model; qualitatively similar results can be obtained by inverting the QGIF model (not shown).

In sum, the proposed approach can reconstruct spikes veridically from single-spike-evoked transients with fast rise times, even at a low SNR level.

Simulated single-spike-evoked transients (with slow rise times)

For slowly rising transients there is a delay (on the order of 100 *ms*) between the onset of the spike and the peak of the fluorescence transient. Although this may not be a crucial issue for reconstruction methods, this delay may cause difficulty for reconstruction methods that rely on a rather instantaneous relationship between spike and fluorescence transient peak, e.g. the sequential Monte Carlo [19] or finite rate of innovation [92] methods. Here, we show that the proposed method can precisely reconstruct single spikes even if the transients have slow rise kinetics.

The interpolated rise kinetics of the fluorescence transients lasted around 200–450 *ms*, see the fourth row of Fig 5. We inverted the non-bursting models (i.e. QGIF and FHN) for the traces containing single-spike-evoked fluorescence transients (first row of Fig 5). The non-saturating [Ca^{2+}] kinetics and veridical spikes can be accurately estimated for data with high SNR (Fig 5A and 5B), second and third rows; QGIF: SNR ≈ 25, n = 12, M = 0 and FD = 0, FHN: SNR ≈ 25, n = 13, M = 0 and FD = 0), and for the trace with low SNR (Fig 5C; FHN: SNR ≈ 2, n = 13, M = 0 and FD = 0); compare grey stars to inferred spikes in the third row of Fig 5.

We performed these reconstructions with the same parameterization as in the previous section (synthetic adult neurons with faster rise times), since our generative models do not incorporate any parameter which can explicitly capture the slow rise times in the data (τ_{Ca} corresponds only to the 'decay' but not the rise kinetics of the calcium transient; see Eq 11). Still, the results displayed in Fig 5 show that the models can be inverted reasonably well given data with slow rise kinetics. This is because the inference procedure takes into account the stochastic dependencies among the neuronal dynamics (see Methods), whose evolutions over time are constrained by their prior precisions. Accordingly, CaBBI adapts to different fluorescence transient kinetics (as for example here with slow rise kinetics) by using a suitable amount of state-noise on the neuronal dynamics.

PLOS | COMPUTATIONAL BIOLOGY

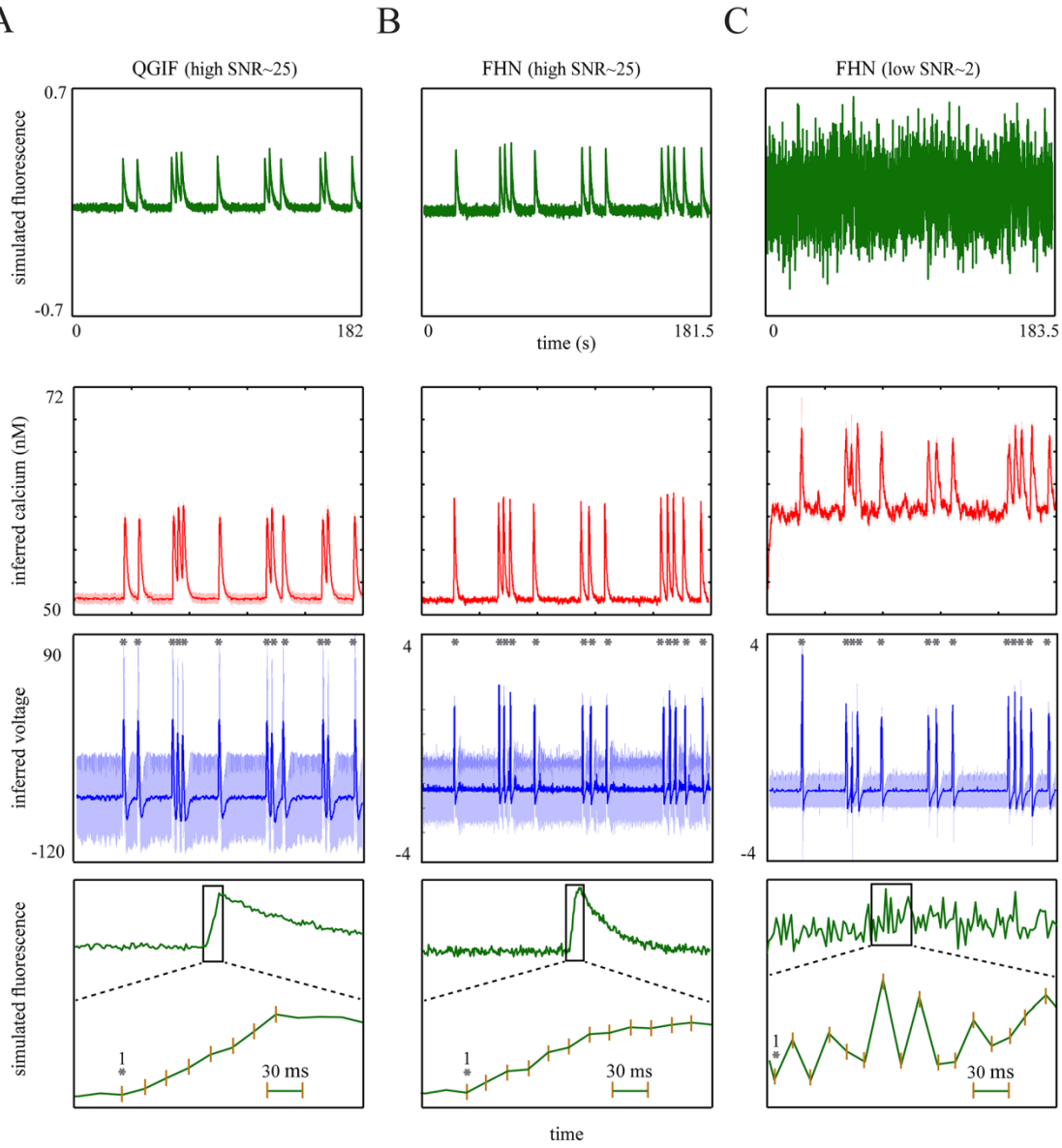

Fig 5. Results of the proposed approach for synthetic single-spike-evoked transients with slow rise times (around 200–450 ms). (**A**): QGIF model, (**B**): FHN model with high SNR, (**C**): FHN model with low SNR. First row: Fluorescence traces generated by each of the two non-bursting generative models. The rising kinetics of all transients were stretched using interpolation, Second row: Inferred non-saturating [Ca^{2+}] kinetics, Third row: Inferred membrane potentials, where the synthetic spikes as indicated by grey stars are closely matched by the inferred spikes, Fourth row: Zoom into the interpolated, slow rise time of the first fluorescence transient in the traces shown in the first row. The time from the simulated spike (grey star) to the peak was roughly 200–450 *ms*. The decaying time-constant of the transients was about 2 seconds.

doi:10.1371/journal.pcbi.1004736.g005

PLOS | COMPUTATIONAL BIOLOGY

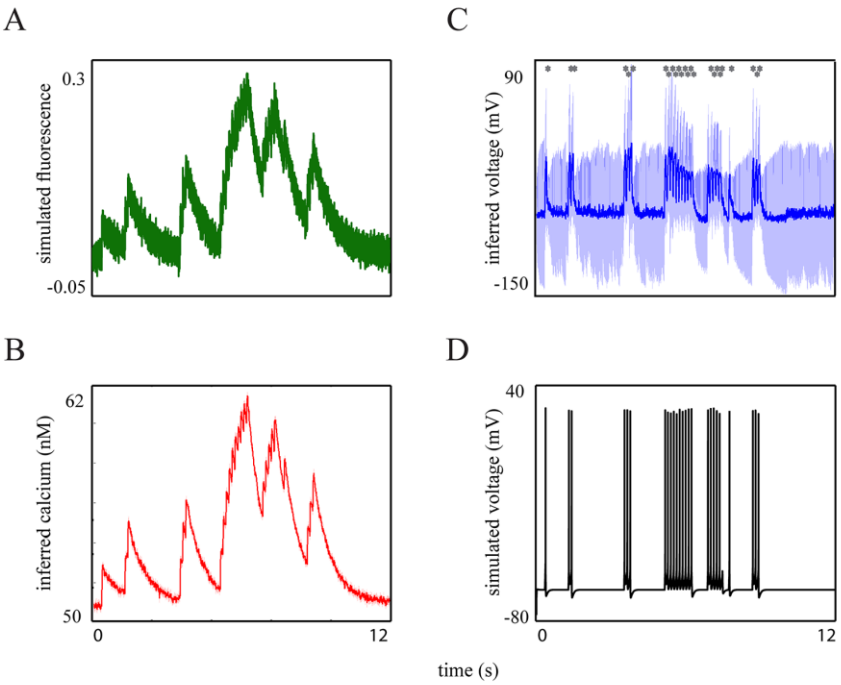

Fig 6. Results of the proposed approach for synthetic burst-evoked transients with fast rise times. (**A**): The fluorescence trace generated by the bursting-QGIF model, sampled at a high frequency of 700 *Hz*. (**B**): Inferred non-saturating [Ca^{2+}] kinetics. (**C**): Inferred membrane potential, (**D**): Simulated membrane potential of the bursting-QGIF model. Comparison of **C** and **D** indicates that both single and within-burst spikes could accurately be detected (note also the grey stars), resulting in a precise estimation of the interburst intervals and periods of quiescence. The values of parameters for the simulations and inversions, as well as the prior distributions can be found in Tables 1 and 2.

doi:10.1371/journal.pcbi.1004736.g006

Simulated burst-evoked transients

Many neurons fire bursts, possibly intermixed with single spikes. Here we show that if the temporal resolution of the fluorescence measurements is high enough, we can still accurately reconstruct spike timing (see Fig 6). This holds true not only for single spikes but also for the spikes within a burst.

For bursts the reconstruction of spike activity from fluorescence traces becomes challenging: For high frequency and/or a high number of spikes within each burst, the impact of calcium accumulation [77] and fluorescence saturation [93,94] becomes relevant (especially when high-affinity indicators are used); in principle, these two mechanisms result in smaller spike-evoked fluorescence transients (thus, smaller effective SNR) with (probably) slower decays [19,26]. These strong nonlinearities will make the spike reconstruction challenging mainly due to the less differentiable transients during bursts.

In general, fluorescence traces with low temporal resolution, e.g. acquired at 4.2 *Hz* [95], cannot resolve the single transients evoked by each distinct spike within a burst [17,95,96]. However, recent developments in calcium imaging have made it possible to obtain fluorescence measurements at very high sampling rates such as 1 *kHz*, for example [13,25]. Assuming a sampling rate of 700 *Hz*, we generated a synthetic fluorescence trace (Fig 6A) using the bursting-QGIF model. To generate complex burst patterns (Fig 6D), we used doublet, triplet and multiplet (5 and 10 spikes)

bursts, and interspersed single spikes (indicated by grey stars in Fig 6C). Although we imposed relatively high noise on the trace, all of single spikes and the within-burst spikes were inferred accurately (Fig 6C; SNR $\approx$ 3, bursting-QGIF: n = 25, M = 0 and FD = 0). In addition, the durations of the bursts' active phase and the interburst intervals, as well as the periods of quiescence were reasonably well estimated (compare the simulated and inferred membrane potentials in Fig 6C and 6D). In addition and as shown in Fig 6C, for each burst the reconstructed spikes have correctly inferred incomplete repolarizations and are located on top of a plateau; this is a common bursting characteristic of many neurons, including hippocampal cells [28,29,58]. The non-saturating [Ca^{2+}] kinetics can also be accurately inferred (Fig 6B) from these saturated traces with highly accumulated transients (Fig 6A). In summary, we found that the method can read out spikes within bursts observed in synthetic fluorescence traces (with fast rise kinetics) when the temporal measurement resolution is high enough, e.g. 700 *Hz*.

Biological data

In vitro recorded fluorescence transients (with slow rise times). Having accurately reconstructed spikes from synthetic data, we now apply the proposed approach to the experimental data recorded in our lab from neonate hippocampal tissue (i.e. first data set; see above). An exclusive feature of these data is the slow rise time (up to several hundred milliseconds) of fluorescence transients, consistent with previous work [27]. For model inversion based on these data, we use the same values of the parameters as for both synthetic data sets with fast rise time and slow rise time; namely, independent of our *in vitro* data. As shown above on synthetic data with slow rise time, we expect that the method can intrinsically adapt to the *in vitro* fluorescence transients without requiring any training/conditioning phase, unlike [5,13,25].

For the analysis, we used six *in vitro* fluorescence image sequences of CA3 immature tissues, as well as the simultaneously recorded transmembrane current signals recorded from two (one per image sequence) patched cells in our experiment (see Experimental methods). For these two cells, the veridical spike times provided by the electrophysiological recordings enabled us to validate the inferred onset times of spiking events (i.e. burst or single spike).

A hallmark of the measured data is spontaneous, synchronized network activities which are expressed as so-called giant depolarizing potentials (GDPs) in individual neurons [97]. In the CA3 hippocampal region, each GDP is usually seen as a slow wave-like propagation (e.g., lasting 200 *ms*) of cellular activation traveling across neurons in the direction, for example, from the CA3c area to the CA3b area [27,98]. An important variable of GDPs is the onset times of cellular activation during GDPs. If one knew the precise onset times of neurons participating in a GDP, one can analyze the underlying spatiotemporal characteristics of GDPs, i.e. the GDP's propagation direction or velocity across the network, the GDP initiators cells, or any systematic cellular activation orders across multiple GDPs [27]. The reconstruction of such network characteristics would enable an improved analysis of the development of immature neuronal circuits, as compared to a GDP analysis based on the smeared fluorescence image sequences [27,99].

We observed the GDP-mediated spiking activity of individual neurons as single or burst of spikes, consistent with [97,100]. In the previous section, we showed that for transients of adult neurons with a fast rise time (e.g. 3 *ms*) and acquired at a high enough temporal resolution (700 *Hz*), the within-burst spikes can be reconstructed accurately using fluorescence measurements. For neonatal neurons, the rise time of each single-spike-evoked transient lasts much longer, e.g. 100 *ms* [27]. This long rise time may be caused by strongly nonlinear mechanisms of Ca^{2+} pumping and buffering [101,102]. In addition, GDP-mediated spiking events occur during synaptically-driven long-lasting depolarizations (up to several hundred milliseconds) with large amplitudes (e.g. -10 *mV*, thus mostly above the half-activation of HVA calcium

PLOS | COMPUTATIONAL BIOLOGY

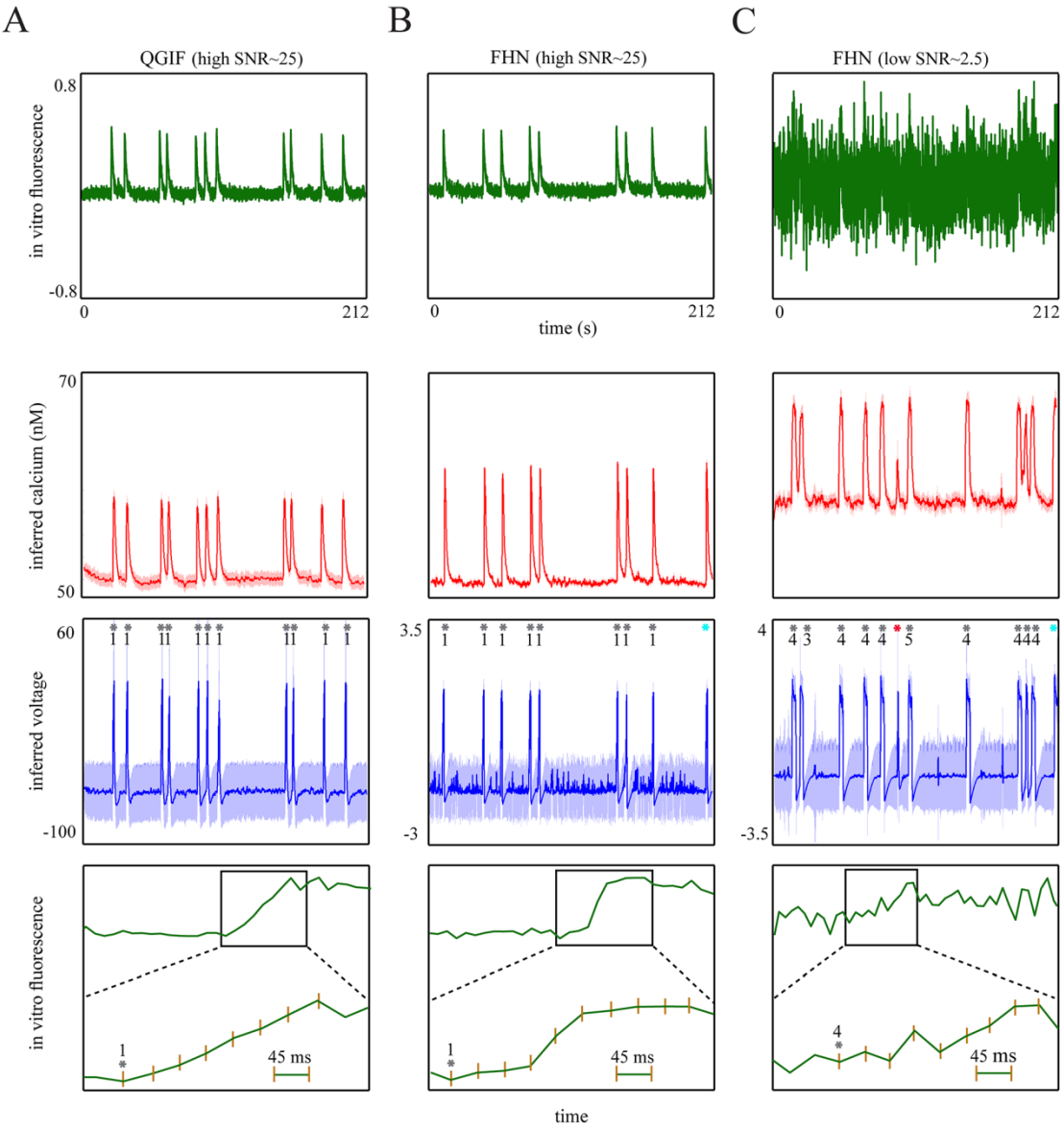

Fig 7. Results of the proposed approach for *in vitro* fluorescence traces with slowly rising transients (around 400 ms). (**A**): QGIF model, (**B**): FHN model with high SNR, (**C**) FHN model with low SNR. First row (**A-C**): The *in vitro* fluorescence traces containing transients with relatively variable and slow rise times, mediated by spontaneous GDPs. The low SNR trace in **C** was generated by contaminating the *in vitro* trace by background noise. Second row (**A-C**): Inferred non-saturating [Ca^{2+}] kinetics, Third row (**A-C**): Inferred membrane potentials, where the onset times of GDP-mediated events (single spike or burst) determined by electrophysiological recordings (grey stars) and inferred spikes are highly concurrent. The two light blue stars indicate that there was no recorded transmembrane current available for the observed events in the fluorescence trace(s). Note that for a GDP-mediated burst event the onset time refers to the occurrence of its first spike. Fourth row (**A-C**): Zoom into the slow rise time of the first fluorescence transient in the traces shown in the first row. The numbers and stars indicate the veridical spike count and the onset time of each GDP. The rise time from GDP onsets to the fluorescence transient peaks was around 300–450 *ms*. The decay kinetics of the transients was lasting around 3.5–4.5 seconds.

doi:10.1371/journal.pcbi.1004736.g007

PLOS | COMPUTATIONAL BIOLOGY

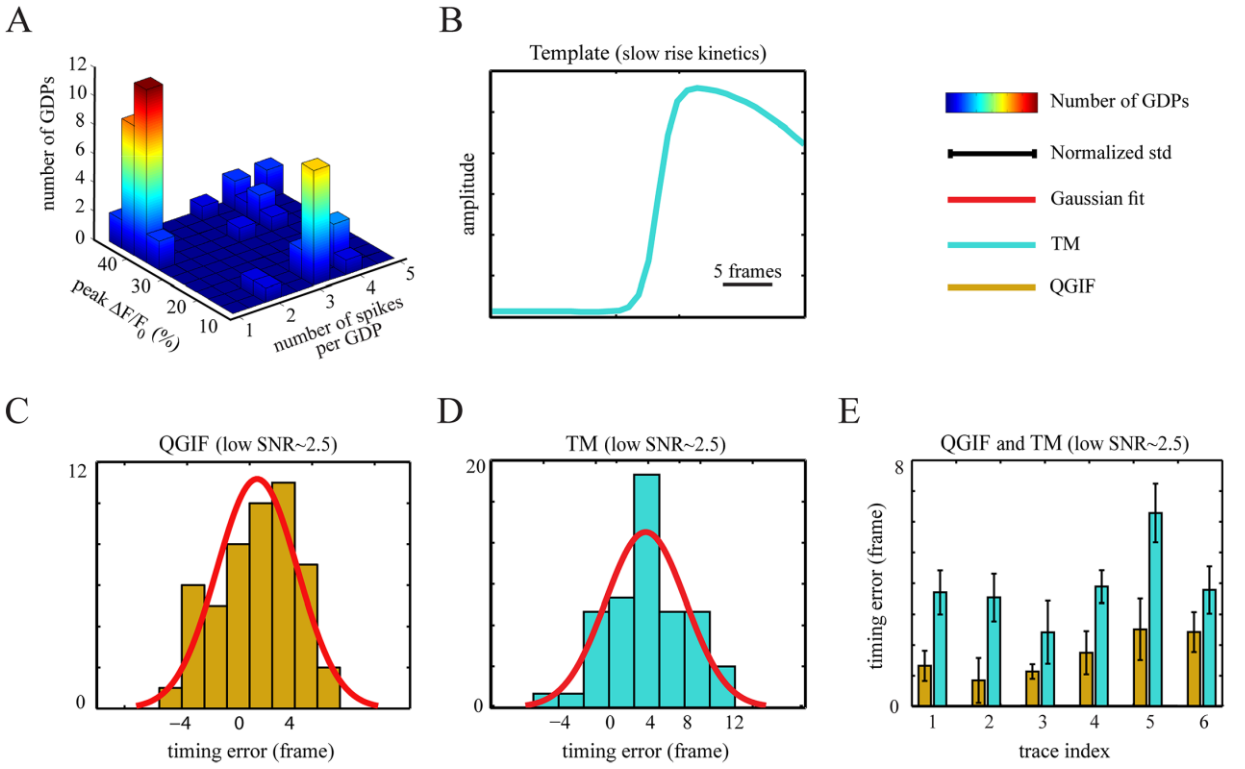

Fig 8. Accuracy of the reconstructed GDP onset times of the proposed approach and template matching method on *in vitro* data. (**A**) The 3D histogram shows the relation between the number of spikes per spontaneous GDPs and the peak of the fluorescence transients (n = 51 GDPs). (**B**) The two-term Boltzmann template for the template matching (TM) method derived from the first experimental data set. (**C**) Timing error distributions computed for the QGIF model inversion for all six fluorescence traces, under low SNR. Gaussian fit: mean = 1.7 and std = 3.2 time bins (i.e. frames). (**D**) Timing error distribution for the TM method, under low SNR. Gaussian fit: mean = 3.7 and std = 3.8 time bins. (**E**) Timing errors estimated by the QGIF model and the TM method plotted for each *in vitro* trace of the first data set.

doi:10.1371/journal.pcbi.1004736.g008

channels) [97], thereby modulating the Ca^{2+} kinetics with added, pronounced nonlinearities. Effectively, for our neonatal neuronal data acquired at 22.6 *Hz*, we could not resolve the GDP-mediated within-burst spikes. This means that in the recorded fluorescence traces, both GDP-mediated burst-evoked and GDP-mediated single-spike-evoked transients were characterized by a single rising phase and a single decaying phase.

In all of these recorded fluorescence traces, there was evidence of slowly varying drifts. To ensure reliable estimates of biophysical parameters and states, we removed these drifts from the traces by using a fourth degree polynomial detrending method (see Methods). In Fig 3B, the original (blue line) and drift-corrected (red line) versions of one of the recorded fluorescence traces are plotted. In addition, we emulated the measurements at a low SNR level by scaling and adding the background noise to the fluorescence traces (see Methods).

In Fig 7 (see also S1 Fig) the precise detection of GDPs is shown for three representative samples (out of six) of drift-corrected *in vitro* fluorescence traces (with slowly rising transients). Critically, as mentioned above, both GDP-mediated bursts and single spikes had similar transient kinetics with a single prolonged rise (up to 400 *ms*, see fourth row of Fig 7A–7C) and large amplitudes which were rather independent of spike count (see Fig 8A); unlike the data from adult neurons [9,103].

Accepting that one cannot differentiate between GDP-mediated single-spike- and burst-evoked transients, we used the two repetitive spiking models (QGIF and FHN) to infer the onset times of individual neurons' firing (single spike or burst) during the synchronous events. We found that both models can accurately detect the experimentally observed GDP-mediated spiking events under high SNR condition (Fig 7A and 7B), third row; QGIF: SNR $\approx$ 25, n = 11, M = 0 and FD = 0, FHN: SNR $\approx$ 25, n = 8, M = 0 and FD = 0). The inferred spike-evoked calcium transients have amplitudes mostly around 10 *nM*, consistent with [13,104]. These values were inferred from the data as we used rather uninformative priors (see Table 2). We also evaluated the performance of our approach for experimental fluorescence traces with low SNR using the FHN model (Fig 7C). The results (Fig 7C) indicate that the inversion can perform reliable inference even under low SNR: A single noise peak was miss-interpreted as a spike (third row, red star; SNR $\approx$ 2.5, n = 10, M = 0 and FD = 1). Although fluorescence measurements are commonly recorded with higher SNRs than the trace displayed in Fig 7C (first panel), this robustness against a high level of noise is important: In principle, for GDP experiments one may use faster cameras and scanners which will result in a lower SNR but an increased temporal resolution. Using the proposed method in combination with such fast imaging techniques, one may be able to better extract the differences in cellular activation latencies during GDP events.

Quantification of detection accuracy: Comparisons

Here, we compare the detection accuracy of our method, CaBBI, to two well-established, widely-used spike reconstruction methods: a template-matching method [85], and a deconvolution-based fast filter method [71].

Comparison on first data set. CaBBI: We first quantified the GDP detection errors (Table 4) as well as the accuracy of the inferred onset times of GDPs (Fig 8C–8E) for our method, under both low SNR (~2.5) and high SNR (~25) conditions. We inverted both the QGIF and FHN models for all six drift-corrected fluorescence traces of the first data set

Table 4. GDP detection results of three different methods (first data set).

Method		# Missed GDPs	# Falsely Detected GDPs
CaBBI	FHN	0	1
	QGIF	2	1
Template matching	$Thr_{TM} = 1$	0	74
	$Thr_{TM} = 1.5$	0	1
	$Thr_{TM} = 2$	3	2
	$Thr_{TM} = 2.5$	18	0
Fast filter	$Thr_{ff} = 0.65$	16	19
	$Thr_{ff} = 0.7$	21	8
	$Thr_{ff} = 0.75$	26	7

GDP detection results of the proposed approach (CaBBI), the template matching (TM) method, and the fast filter technique. For the proposed approach we used both the FHN and QGIF models, for the TM method we employed four detection-criterion thresholds (Thr_{TM}), and for the fast filter three event detection thresholds (Thr_{ff}). The methods were applied to the first data set (*in vitro* data with slowly rising transients) under a low SNR (~2.5). The total number of veridical GDPs was 51. The comparison shows that both the proposed approach and the TM method have a high GDP detection accuracy, while the fast filter cannot solve this task as it was developed for transients with fast rise times.

doi:10.1371/journal.pcbi.1004736.t004

acquired with simultaneous electrophysiological recordings. To read out the GDPs' onset times from the inferred spikes we extracted the time points at which the membrane potential crossed the detection threshold of zero (see Methods). Both the QGIF and FHN models detected the GDPs without error under a high SNR (n = 51, M = 0 and FD = 0). There were only few detection errors under low SNR (see Table 4).

Template matching: In an initial phase, the template (Fig 8B) was determined empirically from the first data set (see Methods). As is common practice, we used several detection-criterion thresholds and selected the best threshold manually. For the optimal threshold (Thr_{TM} = 1.5), the GDP detection accuracy of the TM method was as good as that of CABBI when using the FHN model (Table 4).

Fast filter: We applied the fast filter to the first data set under low SNR, and thresholded its outputs by using a set of event detection thresholds (see Methods). Its detection results for three different thresholds are shown in Table 4; including Thr_{ff} = 0.7 which extracted the events with relatively smaller errors (n = 51, M = 21 and FD = 8) than all other thresholds (i.e. Thr_{ff} = 0, 0.05, . . ., 1). Not surprisingly, this method could not perform a reliable GDP detection from these data, as it has been originally developed for deconvolving fast rising transients [71].

We also computed the 'timing errors' as the difference between the inferred onset times and the veridical GDP-mediated spike times measured by the simultaneously recorded transmembrane current signals (Fig 8C–8E). For GDP-mediated burst events we compared the inferred onset time to the veridical timing of the first spike of that burst. For 51 veridical GDP events the QGIF model showed a reasonably accurate inference about the onset times with a timing error of 1.7 ± 3.2 (mean ± std) for low (Fig 8C) and -0.5 ± 2.0 time bins (frames) for high SNR conditions (not shown). We found the FHN model to be clearly less accurate (timing error of 10.0 ± 10.3 time bins) than the QGIF model. We compared the timing errors of our method only to the TM method, as the fast filter technique showed an insufficient GDP detection accuracy for these data. For the optimal detection-criterion threshold of the TM method (i.e. Thr_{TM} = 1.5; see Table 4), the timing error was 3.7 ± 3.8 time bins (Fig 8D), which is significantly higher (paired-sample Wilcoxon signed-rank test (two-sided); $p < 0.001$) than the error of the QGIF model (Fig 8C). We also show this difference between the two reconstruction methods for single fluorescence traces in Fig 8E.

Overall, these results (Table 4 and Fig 8) indicate that the new method, CaBBI, can detect GDPs as accurately as the TM method and reconstruct the onset times more accurately than the TM method, for low SNR. In addition, CaBBI does not require an initial, interactive phase where the template is estimated and the detection-criterion threshold is selected manually.

Note that the good results of the TM method in comparison to CaBBI and the fast filter method should be interpreted with some caution. The TM method had two specific advantages not harnessed by the other two methods: 1) the fluorescence transients used to define the empirical template were extracted veridically, by harnessing the simultaneously measured electrophysiological data. In addition, the optimal detection-criterion threshold was verified through the electrophysiological data. A fairer comparison would have been to not use the electrophysiological data at all. However, this would have made the comparison operator-dependent when defining the template. 2) The TM template was derived from the same data set, for which spikes/events were detected with that template. In other words, the same data was used for 'training' the model, and again for spike/event detection (testing). In contrast, with CaBBI, we analyzed the data without using any prior information from the same data.

Comparison on second data set. To perform a comparison using data with fast rising transients, for which the fast filter technique was developed, we used twelve *in vitro* fluorescence traces (second data set, see above). These data have been used originally to evaluate the fast filter technique [71]. We performed this comparison in terms of the event, rather than

individual spike, detection accuracy (see Methods), since our method was not able to reconstruct the within-burst spikes from these data (see below). In the following, we explain the comparison results for all three methods.

CaBBI and fast filter: For our method, we used the same parameterization as for the first comparison, after setting *scale* = 1 (see Methods) for all twelve traces. The inversion results of our method (both the QGIF and FHN models) and the fast filter for three representative samples are shown in Fig 9A–9C. The results for these samples show that both methods have qualitatively similar, reasonably good detection accuracy of the spiking events (i.e. bursts or single spikes); note the veridical timing (grey star) and spike count per event on top of the second row, determined by the simultaneous electrophysiological recordings. Note that CaBBI inferred all the single-spike- or burst-evoked transients as if always evoked by single spikes, since the transients evoked by individual spikes are poorly resolved in these data (see [71]). In contrast to the GDP-evoked transients (see Fig 7, first row), in these data the higher spike count per event was mostly encoded by the transients with higher amplitudes (Fig 9A–9C, first row). Although hard to see from the fourth row of Fig 9A–9C, the fast filter used this feature of the data to partially infer the spikes within the burst events, when using a manually determined detection threshold (see Methods). For CaBBI, we observed that as the spike counts of events and therefore the amplitudes of the transients became more variable in a fluorescence trace (compare Fig 9A–9C, first row), inferring the events from transients with lower amplitude became more difficult. As a result, some of them were inferred as partial spikes. For instance, see the fluorescence trace in Fig 9A, which was a hard case also for the fast filter to invert.

In summary, for all twelve traces (Table 5) the FHN model had an event detection accuracy (n = 149, M = 10, and FD = 20) similar to the fast filter with the optimal threshold of 0.35 (n = 149, M = 11, and FD = 15). The QGIF model had, however, an inflated error of missed events and at the same time a considerably smaller error of falsely detected events (n = 149, M = 45, and FD = 2), as compared to the fast filter. When applying the template matching method, we first defined the empirical template, applied it to all twelve traces, and then selected the optimal detection-criterion threshold manually. Among the three methods, TM detected the events with the highest accuracy (n = 149, M = 7, and FD = 1), when using its optimal threshold which was $\mathrm{Thr}_{\mathrm{TM}} = 1.5$ (see Table 5). Although, note that the same two caveats for the TM method apply as in the comparison on the first data set (see above).

Inference on GDP propagation patterns

Above, we already showed the reasonably high accuracy of our method in reconstructing GDP onset times (see Fig 8). We now show the usefulness of this accuracy in inferring the propagation patterns of GDPs, as the complex characteristics of immature neuronal circuits.

We illustrate the reconstruction of GDP characteristics using one representative fluorescent image sequence (out of six) recorded in our experiment. For this image sequence, the fluorescence traces were extracted from 40 well identifiable neurons. The raster plot of color-coded high SNR fluorescence traces in Fig 10A (upper panel) shows clearly visible, spontaneous synchronous network events (i.e. GDPs). The same data under low SNR condition (around 2.5; after contaminating the traces by scaled background noise; see above) is shown in the lower panel of Fig 10A. Using the new method and as a proof of principle, we reconstructed the onset times of all 40 neurons during GDPs, under the low SNR condition. For inversions, we used the QGIF model because of its lower timing error in extraction of GDPs' onset times, as compared to the FHN model and the TM method (see above). The reconstructed events are shown in Fig 10B, where it can easily be seen that their timings show a close match to the large fluorescence changes in Fig 10A (upper panel).

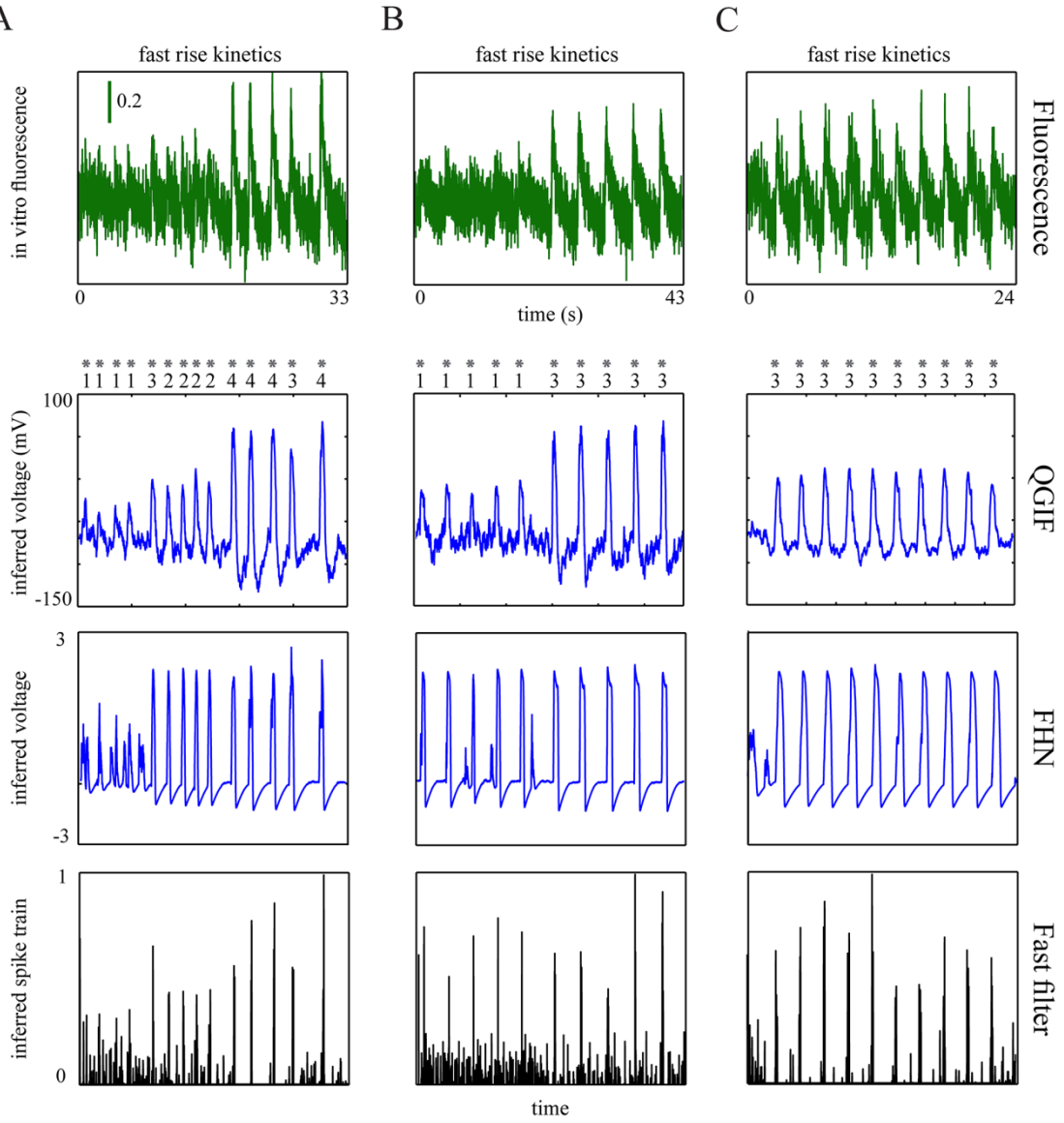

Fig 9. Comparison of the proposed approach and the fast filter for *in vitro* fluorescence traces with fast rising transients. First row: The *in vitro* fluorescence traces containing transients with fast rise times. Second and third rows: Inferred membrane potentials (posterior means) using CaBBI with the QGIF and FHN models. Fourth row: Inferred spike trains of the fast filter. The comparison of the veridical spiking events (grey stars) to the inferred ones (**A-C**, the last three rows) shows that both methods have similar event detection results for fast rising transients. The numbers below the grey stars indicate the spike count per each veridical event, determined by electrophysiological recordings.

doi:10.1371/journal.pcbi.1004736.g009

The histogram of onset latencies of neurons over all GDPs is plotted in Fig 10C. For each GDP, the latencies were computed with respect to the median onset time of neurons during that GDP. In this histogram, the medians are centered on 0 *ms* so that earlier and later activations of neurons have negative and positive values, respectively. The observed latency

Table 5. Event detection results of three different methods (second data set).

Method		# Missed events	# Falsely Detected event
CaBBI	FHN	10	20
	QGIF	45	2
Template matching	$Thr_{TM} = 1$	0	14
	$Thr_{TM} = 1.5$	7	1
	$Thr_{TM} = 2$	32	0
	$Thr_{TM} = 2.5$	53	0
Fast filter	$Thr_{ff} = 0.3$	3	40
	$Thr_{ff} = 0.35$	11	15
	$Thr_{ff} = 0.4$	19	10

Event detection results of the proposed approach (CaBBI), the template matching (TM) method, and the fast filter technique. This table uses the same format as Table 4. The methods were applied to the second *in vitro* data set with low SNR fast rising transients. The total number of veridical events was 149. The comparison shows that the TM method was the best method for the optimal detection-criterion threshold ($Thr_{TM} = 1.5$). CaBBI (the FHN model) and the fast filter ($Thr_{ff} = 0.35$) had similar event detection accuracy for these data.

doi:10.1371/journal.pcbi.1004736.t005

distribution can be approximated by a Gaussian distribution with a mean of -14.5 *ms* and standard deviation of 90 *ms*, which is consistent with previous reports for the developing hippocampus [27]. For visualization of the difference between onset times, we plotted the reconstructed onset times of the second and third GDPs in Fig 10D. In addition, in Fig 10E we show the inferred onset latencies for these two representative GDPs color-coded at their actual spatial positions in the field of view. In the first of these images (second GDP), the GDP pattern starts roughly in the center of the image and spreads to both left-upward and bottom-right, i.e. from the stratum pyramidale (SP) in CA3 towards both CA1 and dentate gyrus (DG). The second image (third GDP) shows, instead, a rather clear unidirectional orientation towards DG. Such wave-like patterns of propagation of these two illustrative GDPs are consistent with previous reports [27,105].

Inferring biophysical parameters

In this section, we show how our approach can be used for quantifying biophysically interpretable parameter changes based on calcium imaging data, e.g. for inferring changes of parameters due to pharmacological interventions. To provide a proof-of-concept, we used two synthetic data sets where we changed: 1) the calcium decay time-constant and 2) the conductance of M-type K^+ channels.

Change of calcium decay time-constant. In general the calcium/fluorescence transients may display variable kinetics. We use the parameterization of a previously reported experiment: Sasaki et al. (2008) [5] investigated the contribution of endogenous Ca^{2+} stores to calcium transients by pharmacologically depleting calcium in the endoplasmic reticulum. The authors treated the neurons with thapsigargin; an inhibitor of the Ca^{2+}-ATPase family of calcium pumps. Their results showed that the thapsigargin profoundly prolongs the decay kinetics of calcium transient while its effect on the transient amplitude is insignificant. We thus reproduced such fluorescence traces (Fig 11A and 11B), first row), by using the FHN as a generative model. Based on values reported by [5], we simulated the fluorescence traces by setting τ_{Ca} = 600 *ms* for the control and τ_{Ca} = 6000 *ms* for the thapsigargin-treated neuron. We inverted the

PLOS | COMPUTATIONAL BIOLOGY

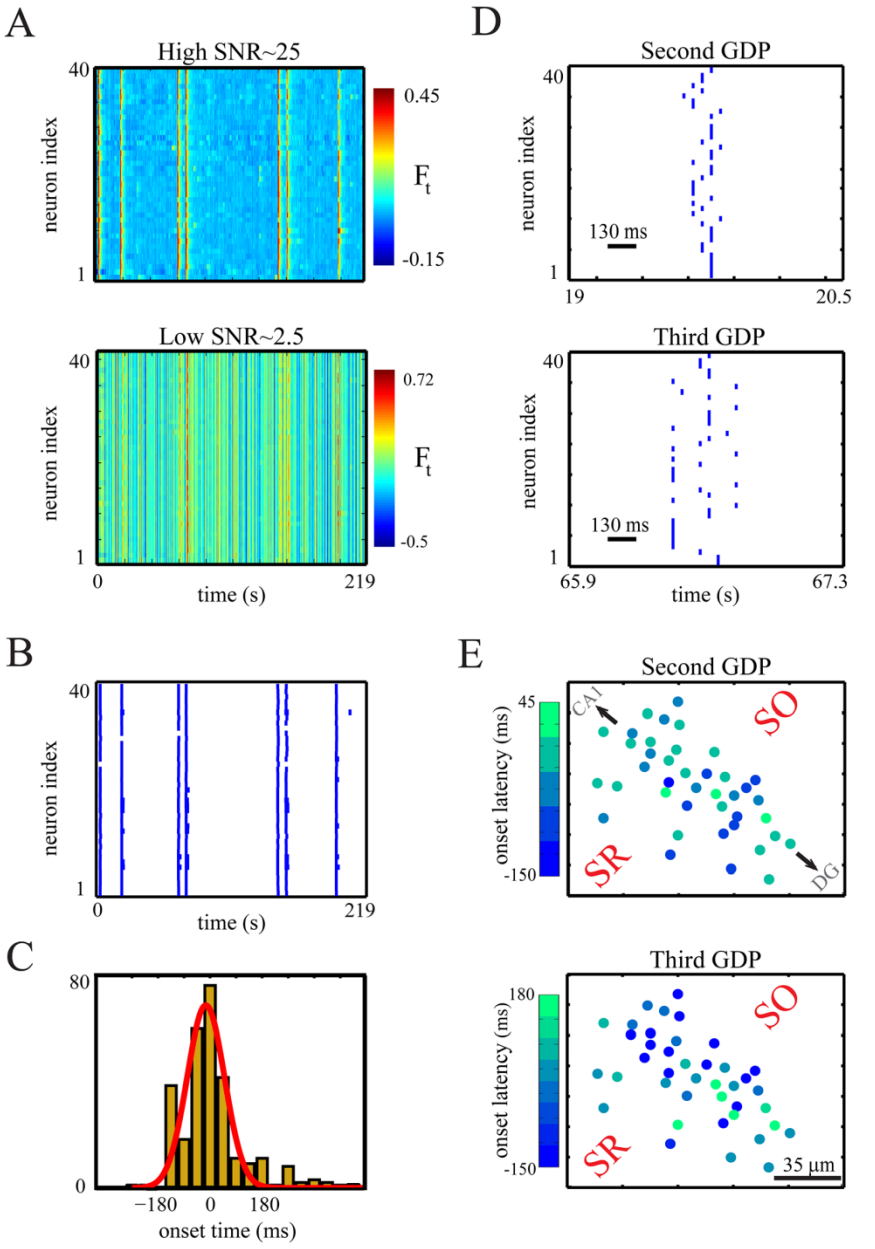

Fig 10. Using the proposed approach for large-scale reconstruction of the cellular activation latencies during GDPs. (**A**) Two raster plots of color-coded *in vitro* fluorescence traces for 40 CA3 immature neurons. Upper Panel: high SNR condition, Lower panel: low SNR condition. (**B**) The reconstructed patterns of onset times of spontaneous activities (both isolated and GDP-mediated events), identified by inverting the QGIF model for low SNR data (lower panel of **A**). (**C**) Histogram of cellular activation latency distributions over all reconstructed GDPs and neurons. The red curve shows a Gaussian fit: with mean = -14.5 and std = 90 *ms*. (**D**) Closer inspection of the reconstructed raster plots in B around the second and third GDPs, unveiling the cellular activation latencies during each GDP. (**E**) The spatiotemporal GDP propagation across neurons can be observed based on color-coded latencies of neurons during the second and third GDPs. SR and SO denote stratum radiatum and stratum oriens of the hippocampal CA3, and DG denotes dentate gyrus.

doi:10.1371/journal.pcbi.1004736.g010

PLOS | COMPUTATIONAL BIOLOGY

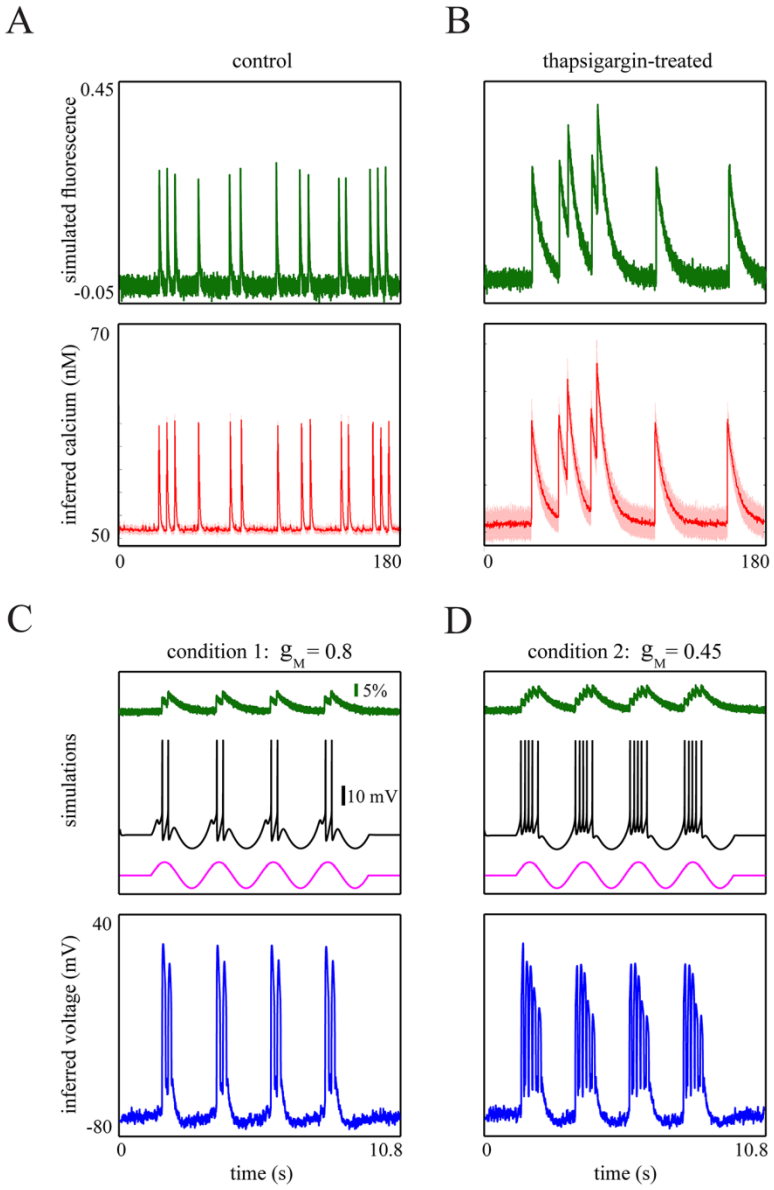

Fig 11. Inference about parameter changes in synthetic data. (**A** and **B**): The simulated fluorescence traces (green line) by the FHN model for (**A**) $\tau_{Ca} = 600\ ms$ and (**B**) $\tau_{Ca} = 6000\ ms$. Red lines show the inferred non-saturating $[Ca^{2+}]$ kinetics of the FHN model. (**C** and **D**): the simulated fluorescence traces (green line), membrane potentials (black line), and the applied input current (magenta line, shown in arbitrary units) to the bursting-QGIF neuron models for (**C**) $g_M = 0.8$ and (**D**) $g_M = 0.45\ mS/cm^2$. The bottom panels show the membrane potentials (posterior means; blue lines) inferred using the bursting-QGIF model for the two fluorescence traces. Parameters for simulating the data (different from Table 1): (**A**) $\tau_{Ca} = 600\ ms$, (**B**) $\tau_{Ca} = 6000\ ms$, (**C** and **D**) $I_{app} = 0.74\sin(0.003t)\ \mu A/cm^2$, $g_{NaP} = 0.18$, $g_L = 0.01\ mS/cm^2$, $\kappa_F = 1$, $K_d = 150\ nM$, $\tau_{Ca} = 500\ ms$, (**C**) $g_M = 0.8$, (**D**) $g_M = 0.45\ mS/cm^2$. Parameters for inversion (different from Tables 1 and 2): (**A**) $\Upsilon_F = 5$, $\tau_{Ca}^{real} \approx 1000\ ms$, (**B**) $\Upsilon_F = 5$, $\tau_{Ca}^{real} = 9000\ ms$, (**C** and **D**) $g_M^0 = 1\ mS/cm^2$ (the only free parameter, in addition to initial conditions), all other parameters were fixed at their values that we used for simulating **C** and **D**.

doi:10.1371/journal.pcbi.1004736.g011

model for each generated time series. For the two inversions, we used the same priors for all parameters, as in previous sections (see Tables 1 and 2), except for two of them: Firstly, for the calcium decay time-constant we used an increased prior mean to inform the inversion about the expected effect of the pharmacological manipulation. Accordingly, we set $\tau_{Ca}^{real} = 1000\ ms$ (consistent with calcium decay time-constant in the mammalian brain [9]) for the control and $\tau_{Ca}^{real} = 9000\ ms$ for the thapsigargin-treated fluorescence traces, respectively. Secondly, we slightly increased the observation precision from $\Upsilon_F = 3$ to 5 in order to make the model explain the data by changing the calcium decay time-constant parameter. The results show that the inferred decay time-constants for non-saturating $[Ca^{2+}]$ kinetics (Fig 11A and 11B), second row) were reasonably well estimated as $\tau_{Ca}^{real} \approx 580\ ms$ and 5820 *ms*.

Change of voltage-gated channel conductance. In a second simulation, we tested how reliably our approach can quantify changes of the conductance of a voltage-gated channel (Fig 11C and 11D). We focused on M-type K^+ channels, which are known to control the burstiness of action potential discharges [57,106]. Therefore, we considered an experiment based on the bursting-QGIF model in which the conductance of M-type K^+ channels was varied (e.g. see [106]). We simulated two neurons with exactly the same parameterization (see the caption of Fig 11), except for g_M (set to $g_M = 0.8$ and $g_M = 0.45\ mS\ /\ cm^2$). For stimulation, we used the same sinusoidal input current for both conditions (Fig 11C and 11D), magenta lines). As expected, this input triggered a lower number of spikes per burst for higher g_M (2 spikes; see Fig 11C, black lines), as compared to the second condition (4 spikes, Fig 11D). Note that, as the potassium channels act and integrate effectively in (sub-) millisecond ranges, only fluorescence traces acquired with a sufficiently high temporal precision might be informative about their kinetics. This is important for inferring about the changes in g_M. Accordingly, we subsampled the generated fluorescence traces from their original temporal precision (20 *kHz*) to a frame duration of about 0.5 *ms* (Fig 11C and 11D, green lines). Such near millisecond frame duration should be feasible with the advent of new fast imaging techniques (e.g. see [13,25]). Note that, given only these fluorescence traces, inferring about the induced changes in g_M is still a challenging task. This is because of the relatively similar values we used for g_M, in combination with an indirect, highly nonlinear relationship between the activation variable of this channel and the observed fluorescence traces (see Methods). To test for a change in g_M, we fixed all parameters at their true values (assuming that these parameters have been determined already in an initial baseline experiment), except the initial conditions and g_M (see the caption of Fig 11) which we kept as free parameters and for which we used the same priors as before (Table 2). This implies that the prior mean of the M-type K^+ conductance is effectively set to $g_M^0 = 1\ ms\ /\ cm^2$ [57]. The inversions were not informed about the input current. We found that our method was able to estimate g_M for both conditions close to the true values as $g_M \approx 0.73$ and $0.42\ mS\ /\ cm^2$, respectively. These estimates were obtained by making a reasonably good inference about the membrane potentials (Fig 11C and 11D, blue lines), and thus the gating variable of the M-type K^+ channels and $[Ca^{2+}]$ kinetics (not shown).

In sum, these two synthetic examples show that the new approach can infer and quantify the changes in hidden parameters of interest, given only the fluorescence traces. Particularly, the second example indicates how a focused constraint may enable the sensitive analysis of changes in biophysical parameters.

Discussion

We have presented a novel Bayesian, biophysically informed method (called CaBBI; an abbreviation of "*calcium* imaging analysis using *biophysical* models and *Bayesian inference*") for the analysis of calcium imaging data. Using both synthetic and *in vitro* data we have shown that

CaBBI provides an accurate spike reconstruction not only under low SNR conditions but also for different fluorescence transient kinetics, such as slowly rising fluorescence transients of immature neurons. Importantly, as we used a biophysically informed method, we performed the reconstruction without an initial training phase, which is usually required for template-based methods. Using synthetic data, we have shown that the method can accurately reconstruct within-burst spikes, if the temporal resolution is high enough. As two potential applications, we have quantified the onset times of cellular activation during network events such as giant depolarizing potentials (GDPs), as well as changes in biophysically interpretable parameters due to simulated pharmacological interventions.

Biophysical modelling

The biophysically informed model has the key advantage that the possible fluorescence trace variations are highly constrained by the equations of the generative model (see Table 3). This guards the model inference effectively against noise sources which are unlikely to be caused by noise in the modelled neuronal and calcium dynamics. In addition, CaBBI allows the incorporation of prior knowledge about the biophysically interpretable model quantities. The specification of prior distributions is a convenient compromise between fixing and freeing parameters when inverting the model. By varying the width of the prior distribution, one can effectively control how much each parameter or combinations of parameters are determined by the data or by prior knowledge. Although not shown here, formal model comparison can be used to select the best model among different prior specifications [107,108].

The biophysical modelling aspect enables CaBBI to directly infer and quantify biophysically interpretable changes caused by selective manipulations of physiological parameters using a pharmacological intervention (see Fig 11). Critically, one can test specific hypotheses by using suitable priors which are susceptible for the expected changes caused by an intervention. Using model comparison, one can proceed to test this change-sensitive model against an alternative model that does not expect this change. In this paper, we showed such an application for quantifying a particular pharmacologically-induced change: i) in the calcium decay time-constant (Fig 11A and 11B, and ii) in the conductance of M-type K^+ channels (Fig 11C and 11D). We found that CaBBI could reasonably reliably infer about the changes in these protocols, since we appropriately fixed and/or constrained its model quantities thereby informing it about the purpose of each intervention (see the caption of Fig 11). In general, such informative constraints can augment the accuracy of corresponding inference schemes, by guarding them against over-parameterization, non-identifiability, and non-interpretability. These issues may arise from the relative complexity of the generative models (see below), and the nonlinear relationship between the observed fluorescence kinetics and the neuronal dynamics. In principle, we expect that this approach (exemplified in Fig 11) can be applied to other physiological parameters under different experimental conditions, as long as suitable model constraints are used.

To our knowledge, CaBBI is the first method which enables analyzing calcium imaging data based on biophysical models of spike and burst generations. Accordingly, in addition to proposing a pure spike reconstruction method, our aim was to establish a calcium imaging modelling framework for incorporating and inferring neuronal quantities of conductance-based neuronal networks. The main feature of CaBBI is that, using the same parameterization, it can model fluorescence transients with rather different kinetics. Such variability can, in principle, render the spike reconstruction difficult for methods which are based on fixed or prototypical templates, e.g. [7,9,12–14,17,109]. In contrast, CaBBI, similar to some previously proposed methods [19,25,71], does not rely on a fixed template but can adapt itself to the transient kinetics of each individual neuron in order to precisely reconstruct spikes. We showed this for

fluorescence traces containing transients with significantly variable kinetics, i.e. with rather inhomogeneous rise and decay kinetics (e.g. see Fig 10). The reason for this adaptation ability is that CaBBI is informed by the generative biophysical model about the possible kinetics and infers the exact kinetics from the data. Therefore, CaBBI does not require an initial training phase neither for constraining the prior distributions [25] nor for setting the optimal method parameters manually.

One potential limitation is that CaBBI, as compared to alternative methods, requires rather long computer run times due to the Bayesian inference and the implementation in Matlab. For example, the reconstruction of the spikes of a single fluorescence trace with 6,000 frames using default parameters and the QGIF model requires less than an hour on a standard desktop computer. To compute all inversions reported in this paper in an acceptable time, we made use of compute servers. A second potential limitation is that due to the relative complexity of the generative models we had to fix many of the parameters at some suitable values reported by previous experimental and modelling studies (see Table 1). Without these constraints or using proper prior distributions (see Table 2), CaBBI may be too unconstrained. In this paper, we demonstrated that such suitable constraints exist for the generative models and data we have used. Finally, the current generative models of CaBBI are not able to reconstruct the spike counts from the burst-evoked transients which have similar shape as single-spike-evoked transients, e.g. due to a low sampling rate. For adult neurons, usually, such transients differ mainly in their amplitudes depending on the spike counts of their underlying events. Although only a few methods (like the fast filter [71]) are, at least in principle, able to decode the bursts' spike counts from such variability (e.g. in the amplitudes), our current generative models treat all such transients as having been evoked by single spikes (e.g. see Fig 9). This is because of the biophysical essence of our neuron models, which relate each resolved transient to a spike, and compensate for such variability in the rise kinetics through a proper regulation of the neuronal dynamics.

FHN and QGIF models

For CaBBI to be applied, one requires a biophysically informed model based on continuous over time, differentiable dynamics. In the literature, a wide range of both spiking and bursting models was reported [21], including Hodgkin-Huxley-type models [38], Morris-Lecar model [110], and Hindmarsh-Rose model [36]. Another criterion for CaBBI to work properly is that the generative model should have a rather low number of variables and parameters as the fluorescence trace is not too informative about the underlying neuronal variables due to the temporal smearing of the calcium responses. As a representative of such continuous models we have selected the widely-used FHN model (2D), which is able to produce single spikes [40–42]. Alternatives would have been analogous 2D models such as the Morris-Lecar model [110] or reduced versions of the Hodgkin-Huxley model [111]; see also [49]. We also used integrate-and-fire (I&F) models. To make them continuous and avoid the discontinuous reset conditions of I&F models, e.g. [33,112,113], we described two new models called QGIF (1D) and bursting-QGIF (2D), see Table 3. These two models adopt a minimum number of required variables for producing the single (QGIF) and burst (bursting-QGIF) spiking patterns. In addition, the QGIF model can be readily extended to describe different types of neurons with their specific active ionic currents [114], e.g. we showed this by creating the bursting-QGIF model for hippocampal pyramidal neurons.

With respect to the reconstruction efficiency we found that the FHN model is better suited for more accurate single spike and event (like GDP occurrence) detection than the QGIF model. Under a low SNR, the inferred membrane potentials of the QGIF model were usually

relatively noisy and the inferred spikes sometimes did not cross the detection threshold (see Methods) of zero, and were thus counted as missed events (e.g. see Table 4); this indicates that to increase the detection accuracy of the QGIF model one may need to use a lower detection threshold, like -10 mV. The greater robustness of the FHN model is possibly due to its recovery variable (Eq 2) whose negative feedback on membrane potential constrains the membrane potential kinetics.

For fluorescence transients with slow rise kinetics observed in our experimental data, we found that the QGIF model can reconstruct the onset times of GDP events more accurately than the FHN model (see Fig 8, and text). The precise GDP onset time reconstruction of the QGIF model was preserved even for low SNR traces. For the QGIF model, the optimization process converges usually quicker than the FHN model. Therefore, in terms of time consumption the QGIF model can be more reasonable to use for data of, e.g., a population of neurons imaged by regular experimental setups which usually acquire data at rather high SNR levels.

Further improvements and extensions

An advantage of CaBBI is that one can readily modify the generative models or replace them with other models. For instance, using CaBBI for the reconstruction of spikes from slowly rising fluorescence transients acquired at near-millisecond temporal resolution may further require a modification of the generative models. To do this, one can incorporate, e.g., an extended model of calcium dynamics (Eq 11) which prolongs the Ca^{2+} influx so that the mechanism of delay between the spike occurrence and the fluorescence transient peak is explicitly captured. For data providing such temporal resolution, one can also model the experimentally observed double-exponential decay kinetics of calcium transients including the typically observed rise time [13,115]. In general, this observation reflects the contribution of two $[Ca^{2+}]$ decay mechanisms with different time-constants, which can be modeled in Eq 11, similarly to [115]. This generalization should provide a better fit to data showing such kinetics, and thus enhance the reconstruction precision.

Large-scale calcium imaging from populations of individual neurons aims to provide a better understanding of neuronal circuit dynamics [1,7,11]. CaBBI provides a new model-based calcium imaging framework, and as an outlook, may be extended to analyze the data of imaged populations. More specifically, the presented approach is a first step towards incorporating the networks of biophysical spiking neuron models (e.g. see [116,117]), together with their ubiquitous mechanisms such as synaptic plasticity (e.g. see [117–119]). We expect that such a network extension enables studying the neuronal dynamics and biophysical parameters of complex neuronal circuits measured indirectly by calcium imaging.

Supporting Information

S1 Appendix. Model specifications and parameters.
(DOCX)

S2 Appendix. Polynomial filter.
(DOCX)

S1 Fig. Additional illustrative results of the proposed approach for *in vitro* fluorescence traces with slowly rising transients. The same format is used as in Fig 9. This figure shows the inferred membrane potentials (posterior means) when using the FHN and QGIF models for two representative *in vitro* fluorescence traces with slowly rising transients evoked by GDP-mediated single spikes, under low SNR.
(TIF)

Author Contributions

Conceived and designed the experiments: KK KH. Performed the experiments: KK. Analyzed the data: VR SJK. Contributed reagents/materials/analysis tools: VR SJK. Wrote the paper: VR KK DM KH SJK.

References

1. Grienberger C, Konnerth A (2012) Imaging calcium in neurons. Neuron 73: 862–885. doi: 10.1016/j.neuron.2012.02.011 PMID: 22405199
2. Brenowitz SD, Regehr WG (2007) Reliability and heterogeneity of calcium signaling at single presynaptic boutons of cerebellar granule cells. J Neurosci 27: 7888–7898. PMID: 17652580
3. Majewska A, Sur M (2003) Motility of dendritic spines in visual cortex in vivo: changes during the critical period and effects of visual deprivation. Proc Natl Acad Sci U S A 100: 16024–16029. PMID: 14663137
4. Maravall M, Mainen ZF, Sabatini BL, Svoboda K (2000) Estimating intracellular calcium concentrations and buffering without wavelength ratioing. Biophys J 78: 2655–2667. PMID: 10777761
5. Sasaki T, Takahashi N, Matsuki N, Ikegaya Y (2008) Fast and accurate detection of action potentials from somatic calcium fluctuations. Journal of Neurophysiology 100: 1668–1676. doi: 10.1152/jn.00084.2008 PMID: 18596182
6. Gobel W, Helmchen F (2007) In vivo calcium imaging of neural network function. Physiology (Bethesda) 22: 358–365.
7. Greenberg DS, Houweling AR, Kerr JN (2008) Population imaging of ongoing neuronal activity in the visual cortex of awake rats. Nat Neurosci 11: 749–751. doi: 10.1038/nn.2140 PMID: 18552841
8. Ohki K, Chung S, Ch'ng YH, Kara P, Reid RC (2005) Functional imaging with cellular resolution reveals precise micro-architecture in visual cortex. Nature 433: 597–603. PMID: 15660108
9. Kerr JND, Greenberg D, Helmchen F (2005) Imaging input and output of neocortical networks in vivo. Proceedings of the National Academy of Sciences of the United States of America 102: 14063–14068. PMID: 16157876
10. Luo L, Callaway EM, Svoboda K (2008) Genetic dissection of neural circuits. Neuron 57: 634–660. doi: 10.1016/j.neuron.2008.01.002 PMID: 18341986
11. Ikegaya Y, Aaron G, Cossart R, Aronov D, Lampl I, et al. (2004) Synfire chains and cortical songs: temporal modules of cortical activity. Science 304: 559–564. PMID: 15105494
12. Smetters D, Majewska A, Yuste R (1999) Detecting action potentials in neuronal populations with calcium imaging. Methods 18: 215–221. PMID: 10356353
13. Grewe BF, Langer D, Kasper H, Kampa BM, Helmchen F (2010) High-speed in vivo calcium imaging reveals neuronal network activity with near-millisecond precision (vol 7, pg 399, 2010). Nature Methods 7: 479–479.
14. Kerr JN, de Kock CP, Greenberg DS, Bruno RM, Sakmann B, et al. (2007) Spatial organization of neuronal population responses in layer 2/3 of rat barrel cortex. J Neurosci 27: 13316–13328. PMID: 18045926
15. Moreaux L, Laurent G (2007) Estimating firing rates from calcium signals in locust projection neurons in vivo. Front Neural Circuits 1: 2. doi: 10.3389/neuro.04.002.2007 PMID: 18946544
16. Mukamel EA, Nimmerjahn A, Schnitzer MJ (2009) Automated analysis of cellular signals from large-scale calcium imaging data. Neuron 63: 747–760. doi: 10.1016/j.neuron.2009.08.009 PMID: 19778505
17. Yaksi E, Friedrich RW (2006) Reconstruction of firing rate changes across neuronal populations by temporally deconvolved Ca2+ imaging. Nat Methods 3: 377–383. PMID: 16628208
18. Ramdya P, Reiter B, Engert F (2006) Reverse correlation of rapid calcium signals in the zebrafish optic tectum in vivo. J Neurosci Methods 157: 230–237. PMID: 16765450
19. Vogelstein JT, Watson BO, Packer AM, Yuste R, Jedynak B, et al. (2009) Spike Inference from Calcium Imaging Using Sequential Monte Carlo Methods. Biophysical Journal 97: 636–655. doi: 10.1016/j.bpj.2008.08.005 PMID: 19619479
20. Ermentrout B, Terman D (2010) Mathematical Foundations of Neuroscience: Springer.
21. Izhikevich EM (2004) Which model to use for cortical spiking neurons? Neural Networks, IEEE Transactions on 15: 1063–1070.
22. David O, Kiebel SJ, Harrison LM, Mattout J, Kilner JM, et al. (2006) Dynamic causal modeling of evoked responses in EEG and MEG. Neuroimage 30: 1255–1272. PMID: 16473023

23. Kiebel SJ, Garrido MI, Moran R, Chen CC, Friston KJ (2009) Dynamic causal modeling for EEG and MEG. Hum Brain Mapp 30: 1866–1876. doi: 10.1002/hbm.20775 PMID: 19360734
24. Cornelisse LN, van Elburg RA, Meredith RM, Yuste R, Mansvelder HD (2007) High speed two-photon imaging of calcium dynamics in dendritic spines: consequences for spine calcium kinetics and buffer capacity. PLoS One 2: e1073. PMID: 17957255
25. Ranganathan GN, Koester HJ (2010) Optical recording of neuronal spiking activity from unbiased populations of neurons with high spike detection efficiency and high temporal precision. J Neurophysiol 104: 1812–1824. doi: 10.1152/jn.00197.2010 PMID: 20610791
26. Yasuda R, Nimchinsky EA, Scheuss V, Pologruto TA, Oertner TG, et al. (2004) Imaging calcium concentration dynamics in small neuronal compartments. Sci STKE 2004: pl5.
27. Takano H, McCartney M, Ortinski PI, Yue C, Putt ME, et al. (2012) Deterministic and stochastic neuronal contributions to distinct synchronous CA3 network bursts. J Neurosci 32: 4743–4754. doi: 10.1523/JNEUROSCI.4277-11.2012 PMID: 22492030
28. Harris KD, Hirase H, Leinekugel X, Henze DA, Buzsaki G (2001) Temporal interaction between single spikes and complex spike bursts in hippocampal pyramidal cells. Neuron 32: 141–149. PMID: 11604145
29. Traub RD, Wong RKS, Miles R, Michelson H (1991) A Model of a Ca3 Hippocampal Pyramidal Neuron Incorporating Voltage-Clamp Data on Intrinsic Conductances. Journal of Neurophysiology 66: 635–650. PMID: 1663538
30. Wong RK, Stewart M (1992) Different firing patterns generated in dendrites and somata of CA1 pyramidal neurones in guinea-pig hippocampus. J Physiol 457: 675–687. PMID: 1297848
31. Daunizeau J, Friston KJ, Kiebel SJ (2009) Variational Bayesian identification and prediction of stochastic nonlinear dynamic causal models. Physica D-Nonlinear Phenomena 238: 2089–2118. PMID: 19862351
32. Hodgkin AL, Huxley AF (1952) A Quantitative Description of Membrane Current and Its Application to Conduction and Excitation in Nerve. Journal of Physiology-London 117: 500–544.
33. Izhikevich EM (2003) Simple model of spiking neurons. IEEE Trans Neural Netw 14: 1569–1572. doi: 10.1109/TNN.2003.820440 PMID: 18244602
34. McCormick DA, Huguenard JR (1992) A model of the electrophysiological properties of thalamocortical relay neurons. J Neurophysiol 68: 1384–1400. PMID: 1331356
35. Rinzel J (1985) Excitation dynamics: insights from simplified membrane models. Fed Proc 44: 2944–2946. PMID: 2415401
36. Rose RM, Hindmarsh JL (1989) The assembly of ionic currents in a thalamic neuron. I. The three-dimensional model. Proc R Soc Lond B Biol Sci 237: 267–288. PMID: 2571154
37. Xu J, Clancy CE (2008) Ionic mechanisms of endogenous bursting in CA3 hippocampal pyramidal neurons: a model study. PLoS One 3: e2056. doi: 10.1371/journal.pone.0002056 PMID: 18446231
38. Pospischil M, Toledo-Rodriguez M, Monier C, Piwkowska Z, Bal T, et al. (2008) Minimal Hodgkin-Huxley type models for different classes of cortical and thalamic neurons. Biol Cybern 99: 427–441. doi: 10.1007/s00422-008-0263-8 PMID: 19011929
39. Rinzel J (1987) A Formal Classification of Bursting Mechanisms in Excitable Systems. In: Teramoto E, Yumaguti M, editors. Mathematical Topics in Population Biology, Morphogenesis and Neurosciences: Springer Berlin Heidelberg. pp. 267–281.
40. Fitzhugh R (1961) Impulses and Physiological States in Theoretical Models of Nerve Membrane. Biophys J 1: 445–466. PMID: 19431309
41. Izhikevich EMaF, R. (2006) FitzHugh-Nagumo model. Scholarpedia 1: 1349.
42. Nagumo J, Arimoto S, Yoshizawa S (1962) Active Pulse Transmission Line Simulating Nerve Axon. Proceedings of the Institute of Radio Engineers 50: 2061–&.
43. FitzHugh R (1955) Mathematical models of threshold phenomena in the nerve membrane. Bulletin of Mathematical Biology 17: 257–278.
44. Knight BW (1972) Dynamics of encoding in a population of neurons. J Gen Physiol 59: 734–766. PMID: 5025748
45. Lapicque L (1907) Recherches quantitatives sur l'excitation electrique des nerfs traitee comme une polarization. J Physiol Pathol Gen 9: 620–635.
46. Stein RB (1967) Some Models of Neuronal Variability. Biophysical Journal 7: 37–68. doi: 10.1016/S0006-3495(67)86574-3 PMID: 19210981
47. Tuckwell HC (1988) Introduction to theoretical neurobiology. Cambridge Cambridgeshire; New York: Cambridge University Press.

48. Trocmé F, Hansel D, van Vreeswijk C, Brunel N (2003) How spike generation mechanisms determine the neuronal response to fluctuating inputs. Journal of Neuroscience 23: 11628–11640. PMID: 14684865

49. Izhikevich E (2007) Dynamical systems in neuroscience: the geometry of excitability and bursting: MIT Press.

50. Latham PE, Richmond BJ, Nelson PG, Nirenberg S (2000) Intrinsic dynamics in neuronal networks. I. Theory. J Neurophysiol 83: 808–827. PMID: 10669496

51. Izhikevich EM (2006) Bursting. Scholarpedia 1: 1300.

52. Cooper DC (2002) The significance of action potential bursting in the brain reward circuit. Neurochem Int 41: 333–340. PMID: 12176075

53. Kepecs A, Wang XJ, Lisman J (2002) Bursting neurons signal input slope. J Neurosci 22: 9053–9062. PMID: 12388612

54. Lisman JE (1997) Bursts as a unit of neural information: making unreliable synapses reliable. Trends Neurosci 20: 38–43. PMID: 9004418

55. Buckmaster PS, Amaral DG (2001) Intracellular recording and labeling of mossy cells and proximal CA3 pyramidal cells in macaque monkeys. J Comp Neurol 430: 264–281. PMID: 11135261

56. Azouz R, Jensen MS, Yaari Y (1996) Ionic basis of spike after-depolarization and burst generation in adult rat hippocampal CA1 pyramidal cells. The Journal of physiology 492 (Pt 1): 211–223. PMID: 8730596

57. Golomb D, Yue C, Yaari Y (2006) Contribution of persistent Na+ current and M-type K+ current to somatic bursting in CA1 pyramidal cells: combined experimental and modeling study. J Neurophysiol 96: 1912–1926. PMID: 16807352

58. Sipila ST, Huttu K, Voipio J, Kaila K (2006) Intrinsic bursting of immature CA3 pyramidal neurons and consequent giant depolarizing potentials are driven by a persistent Na+ current and terminated by a slow Ca2+ -activated K+ current. Eur J Neurosci 23: 2330–2338. PMID: 16706841

59. Su H, Alroy G, Kirson ED, Yaari Y (2001) Extracellular calcium modulates persistent sodium current-dependent burst-firing in hippocampal pyramidal neurons. J Neurosci 21: 4173–4182. PMID: 11404402

60. Daunizeau J, Adam V, Rigoux L (2014) VBA: a probabilistic treatment of nonlinear models for neurobiological and behavioural data. PLoS Comput Biol 10: e1003441. doi: 10.1371/journal.pcbi.1003441 PMID: 24465198

61. Catterall WA (2000) Structure and regulation of voltage-gated Ca2+ channels. Annu Rev Cell Dev Biol 16: 521–555. PMID: 11031246

62. Helmchen F, Imoto K, Sakmann B (1996) Ca2+ buffering and action potential-evoked Ca2+ signaling in dendrites of pyramidal neurons. Biophys J 70: 1069–1081. PMID: 8789126

63. Elliott EM, Malouf AT, Catterall WA (1995) Role of calcium channel subtypes in calcium transients in hippocampal CA3 neurons. J Neurosci 15: 6433–6444. PMID: 7472406

64. Ermentrout B (1998) Linearization of F-I curves by adaptation. Neural Comput 10: 1721–1729. PMID: 9744894

65. Helton TD, Xu W, Lipscombe D (2005) Neuronal L-type calcium channels open quickly and are inhibited slowly. J Neurosci 25: 10247–10251. PMID: 16267232

66. Tuckwell HC (2012) Quantitative aspects of L-type Ca2+ currents. Prog Neurobiol 96: 1–31. doi: 10.1016/j.pneurobio.2011.09.010 PMID: 22008116

67. Kudela P, Franaszczuk PJ, Bergey GK (2003) Reduction of intracellular calcium removal rate can explain changes in seizure dynamics: studies in neuronal network models. Epilepsy Res 57: 95–109. PMID: 15013051

68. Traub RD (1982) Simulation of intrinsic bursting in CA3 hippocampal neurons. Neuroscience 7: 1233–1242. PMID: 7110586

69. Mishchenko Y, Vogelstein J, Paninski L (2011) A Bayesian approach for inferring neuronal connectivity from calcium fluorescent imaging data. The Annals of Applied Statistics 5: 1229–1261.

70. Pologruto TA, Yasuda R, Svoboda K (2004) Monitoring neural activity and [Ca2+] with genetically encoded Ca2+ indicators. J Neurosci 24: 9572–9579. PMID: 15509744

71. Vogelstein JT, Packer AM, Machado TA, Sippy T, Babadi B, et al. (2010) Fast nonnegative deconvolution for spike train inference from population calcium imaging. J Neurophysiol 104: 3691–3704. doi: 10.1152/jn.01073.2009 PMID: 20554834

72. Beal M (2003) Variational algorithms for approximate Bayesian inference.

73. Tanaka T (1999) A theory of mean field approximation. Proceedings of the 1998 conference on Advances in neural information processing systems II: MIT Press. pp. 351–357.
74. Friston K, Mattout J, Trujillo-Barreto N, Ashburner J, Penny W (2007) Variational free energy and the Laplace approximation. Neuroimage 34: 220–234. PMID: 17055746
75. Daunizeau J, Stephan KE, Friston KJ (2012) Stochastic dynamic causal modelling of fMRI data: should we care about neural noise? Neuroimage 62: 464–481. doi: 10.1016/j.neuroimage.2012.04.061 PMID: 22579726
76. Stosiek C, Garaschuk O, Holthoff K, Konnerth A (2003) In vivo two-photon calcium imaging of neuronal networks. Proc Natl Acad Sci U S A 100: 7319–7324. PMID: 12777621
77. Helmchen F (2011) Calibration of Fluorescent Calcium Indicators. Cold Spring Harbor Protocols 2011: pdb.top120.
78. Chouhan VS, Mehta SS. Total Removal of Baseline Drift from ECG Signal; 2007 5–7 March 2007. pp. 512–515.
79. Lowe MJ, Russell DP (1999) Treatment of baseline drifts in fMRI time series analysis. J Comput Assist Tomogr 23: 463–473. PMID: 10348457
80. Smith AM, Lewis BK, Ruttimann UE, Ye FQ, Sinnwell TM, et al. (1999) Investigation of low frequency drift in fMRI signal. Neuroimage 9: 526–533. PMID: 10329292
81. Yizhao N, Chu C, Saunders CJ, Ashburner J. Kernel methods for fMRI pattern prediction; 2008 1–8 June 2008. pp. 692–697.
82. Friman O, Borga M, Lundberg P, Knutsson H (2004) Detection and detrending in fMRI data analysis. Neuroimage 22: 645–655. PMID: 15193593
83. Friman O, Borga M, Lundberg P, Knutsson H (2002) Exploratory fMRI analysis by autocorrelation maximization. Neuroimage 16: 454–464. PMID: 12030831
84. Worsley KJ, Liao CH, Aston J, Petre V, Duncan GH, et al. (2002) A general statistical analysis for fMRI data. Neuroimage 15: 1–15. PMID: 11771969
85. Clements JD, Bekkers JM (1997) Detection of spontaneous synaptic events with an optimally scaled template. Biophys J 73: 220–229. PMID: 9199786
86. Oh MM, Oliveira FA, Waters J, Disterhoft JF (2013) Altered calcium metabolism in aging CA1 hippocampal pyramidal neurons. J Neurosci 33: 7905–7911. doi: 10.1523/JNEUROSCI.5457-12.2013 PMID: 23637181
87. Chen TW, Wardill TJ, Sun Y, Pulver SR, Renninger SL, et al. (2013) Ultrasensitive fluorescent proteins for imaging neuronal activity. Nature 499: 295–300. doi: 10.1038/nature12354 PMID: 23868258
88. Horikawa K, Yamada Y, Matsuda T, Kobayashi K, Hashimoto M, et al. (2010) Spontaneous network activity visualized by ultrasensitive Ca(2+) indicators, yellow Cameleon-Nano. Nat Methods 7: 729–732. doi: 10.1038/nmeth.1488 PMID: 20693999
89. Reiff DF, Ihring A, Guerrero G, Isacoff EY, Joesch M, et al. (2005) In vivo performance of genetically encoded indicators of neural activity in flies. J Neurosci 25: 4766–4778. PMID: 15888652
90. Wilt BA, Fitzgerald JE, Schnitzer MJ (2013) Photon shot noise limits on optical detection of neuronal spikes and estimation of spike timing. Biophys J 104: 51–62. doi: 10.1016/j.bpj.2012.07.058 PMID: 23332058
91. Golshani P, Goncalves JT, Khoshkhoo S, Mostany R, Smirnakis S, et al. (2009) Internally mediated developmental desynchronization of neocortical network activity. J Neurosci 29: 10890–10899. doi: 10.1523/JNEUROSCI.2012-09.2009 PMID: 19726647
92. Onativia J, Schultz SR, Dragotti PL (2013) A finite rate of innovation algorithm for fast and accurate spike detection from two-photon calcium imaging. J Neural Eng 10: 046017. doi: 10.1088/1741-2560/10/4/046017 PMID: 23860257
93. Visscher K, Brakenhoff GJ, Visser TD (1994) Fluorescence saturation in confocal microscopy. Journal of Microscopy 175: 162–165.
94. Yuste R, Konnerth A (2005) Imaging in neuroscience and development: a laboratory manual. Cold Spring Harbor, N.Y.: Cold Spring Harbor Laboratory Press. xvi, 854 p. p.
95. Park IJ, Bobkov YV, Ache BW, Principe JC (2013) Quantifying bursting neuron activity from calcium signals using blind deconvolution. J Neurosci Methods 218: 196–205. doi: 10.1016/j.jneumeth.2013.05.007 PMID: 23711821
96. Lutcke H, Gerhard F, Zenke F, Gerstner W, Helmchen F (2013) Inference of neuronal network spike dynamics and topology from calcium imaging data. Front Neural Circuits 7: 201. doi: 10.3389/fncir.2013.00201 PMID: 24399936
97. Ben-Ari Y, Cherubini E, Corradetti R, Gaiarsa JL (1989) Giant synaptic potentials in immature rat CA3 hippocampal neurones. J Physiol 416: 303–325. PMID: 2575165

98. Valeeva G, Abdullin A, Tyzio R, Skorinkin A, Nikolski E, et al. (2010) Temporal coding at the immature depolarizing GABAergic synapse. Front Cell Neurosci 4.

99. Ben-Ari Y, Gaiarsa JL, Tyzio R, Khazipov R (2007) GABA: a pioneer transmitter that excites immature neurons and generates primitive oscillations. Physiol Rev 87: 1215–1284. PMID: 17928584

100. Leinekugel X, Khalilov I, Ben-Ari Y, Khazipov R (1998) Giant depolarizing potentials: the septal pole of the hippocampus paces the activity of the developing intact septohippocampal complex in vitro. J Neurosci 18: 6349–6357. PMID: 9698326

101. Eilers J, Callewaert G, Armstrong C, Konnerth A (1995) Calcium signaling in a narrow somatic submembrane shell during synaptic activity in cerebellar Purkinje neurons. Proc Natl Acad Sci U S A 92: 10272–10276. PMID: 7479766

102. Eilers J, Plant T, Konnerth A (1996) Localized calcium signalling and neuronal integration in cerebellar Purkinje neurones. Cell Calcium 20: 215–226. PMID: 8889210

103. Rochefort NL, Garaschuk O, Milos RI, Narushima M, Marandi N, et al. (2009) Sparsification of neuronal activity in the visual cortex at eye-opening. Proc Natl Acad Sci U S A 106: 15049–15054. doi: 10.1073/pnas.0907660106 PMID: 19706480

104. Schiller J, Helmchen F, Sakmann B (1995) Spatial profile of dendritic calcium transients evoked by action potentials in rat neocortical pyramidal neurones. J Physiol 487 (Pt 3): 583–600. PMID: 8544123

105. Bolea S, Sanchez-Andres JV, Huang X, Wu JY (2006) Initiation and propagation of neuronal coactivation in the developing hippocampus. J Neurophysiol 95: 552–561. PMID: 16177178

106. Yue C, Yaari Y (2004) KCNQ/M channels control spike afterdepolarization and burst generation in hippocampal neurons. J Neurosci 24: 4614–4624. PMID: 15140933

107. Rigoux L, Stephan KE, Friston KJ, Daunizeau J (2014) Bayesian model selection for group studies—revisited. Neuroimage 84: 971–985. doi: 10.1016/j.neuroimage.2013.08.065 PMID: 24018303

108. Stephan KE, Penny WD, Daunizeau J, Moran RJ, Friston KJ (2009) Bayesian model selection for group studies. Neuroimage 46: 1004–1017. doi: 10.1016/j.neuroimage.2009.03.025 PMID: 19306932

109. Sato TR, Gray NW, Mainen ZF, Svoboda K (2007) The functional microarchitecture of the mouse barrel cortex. PLoS Biol 5: e189. PMID: 17622195

110. Morris C, Lecar H (1981) Voltage oscillations in the barnacle giant muscle fiber. Biophys J 35: 193–213. PMID: 7260316

111. Moehlis J (2006) Canards for a reduction of the Hodgkin-Huxley equations. J Math Biol 52: 141–153. PMID: 16195925

112. Burkitt AN (2006) A review of the integrate-and-fire neuron model: I. Homogeneous synaptic input. Biol Cybern 95: 1–19. PMID: 16622699

113. Smith GD, Cox CL, Sherman SM, Rinzel J (2000) Fourier analysis of sinusoidally driven thalamocortical relay neurons and a minimal integrate-and-fire-or-burst model. J Neurophysiol 83: 588–610. PMID: 10634897

114. Hille B (2001) Ion Channels of Excitable Membranes (3rd Edition): Sinauer Associates Inc 2001–07.

115. Majewska A, Brown E, Ross J, Yuste R (2000) Mechanisms of calcium decay kinetics in hippocampal spines: role of spine calcium pumps and calcium diffusion through the spine neck in biochemical compartmentalization. J Neurosci 20: 1722–1734. PMID: 10684874

116. Shriki O, Hansel D, Sompolinsky H (2003) Rate models for conductance-based cortical neuronal networks. Neural Comput 15: 1809–1841. PMID: 14511514

117. Standage D, Trappenberg T, Blohm G (2014) Calcium-dependent calcium decay explains STDP in a dynamic model of hippocampal synapses. PLoS One 9: e86248. doi: 10.1371/journal.pone.0086248 PMID: 24465987

118. Hennig MH (2013) Theoretical models of synaptic short term plasticity. Front Comput Neurosci 7: 154. doi: 10.3389/fncom.2013.00154 PMID: 24198783

119. Tsodyks M, Uziel A, Markram H (2000) Synchrony generation in recurrent networks with frequency-dependent synapses. J Neurosci 20: RC50. PMID: 10627627

4.2. Manuscript II

Ultra-fast accurate reconstruction of spiking activity from calcium imaging data

Vahid Rahmati, Knut Kirmse, Knut Holthoff, Stefan J. Kiebel

J Neurophysiol 119: 1863–1878, 2018.
First published February 21, 2018; doi:10.1152/jn.00934.2017.

INNOVATIVE METHODOLOGY | *Cellular and Molecular Properties of Neurons*

Ultra-fast accurate reconstruction of spiking activity from calcium imaging data

Vahid Rahmati,[1] Knut Kirmse,[2] Knut Holthoff,[2] and Stefan J. Kiebel[1]
[1]*Department of Psychology, Technische Universität Dresden, Dresden, Germany; and* [2]*Hans-Berger Department of Neurology, University Hospital Jena, Jena, Germany*

Submitted 29 December 2017; accepted in final form 15 February 2018

Rahmati V, Kirmse K, Holthoff K, Kiebel SJ. Ultra-fast accurate reconstruction of spiking activity from calcium imaging data. *J Neurophysiol* 119: 1863–1878, 2018. First published February 21, 2018; doi:10.1152/jn.00934.2017.—Calcium imaging provides an indirect observation of the underlying neural dynamics and enables the functional analysis of neuronal populations. However, the recorded fluorescence traces are temporally smeared, thus making the reconstruction of exact spiking activity challenging. Most of the established methods to tackle this issue are limited in dealing with issues such as the variability in the kinetics of fluorescence transients, fast processing of long-term data, high firing rates, and measurement noise. We propose a novel, heuristic reconstruction method to overcome these limitations. By using both synthetic and experimental data, we demonstrate the four main features of this method: *1*) it accurately reconstructs both isolated spikes and within-burst spikes, and the spike count per fluorescence transient, from a given noisy fluorescence trace; *2*) it performs the reconstruction of a trace extracted from 1,000,000 frames in less than 2 s; *3*) it adapts to transients with different rise and decay kinetics or amplitudes, both within and across single neurons; and *4*) it has only one key parameter, which we will show can be set in a nearly automatic way to an approximately optimal value. Furthermore, we demonstrate the ability of the method to effectively correct for fast and rather complex, slowly varying drifts as frequently observed in in vivo data.

NEW & NOTEWORTHY Reconstruction of spiking activities from calcium imaging data remains challenging. Most of the established reconstruction methods not only have limitations in adapting to systematic variations in the data and fast processing of large amounts of data, but their results also depend on the user's experience. To overcome these limitations, we present a novel, heuristic model-free-type method that enables an ultra-fast, accurate, near-automatic reconstruction from data recorded under a wide range of experimental conditions.

action potential; burst; calcium imaging; model free; reconstruction

INTRODUCTION

Calcium imaging is a widely used technique to indirectly record spiking activity of both individual neurons and neuronal populations (Grienberger and Konnerth 2012). With this technique, fluorescence calcium indicators are genetically encoded, or are directly injected, to the target neural structure. This enables imaging of the changes in intracellular Ca^{2+} concentration, thereby monitoring the underlying spiking activities as fluorescence transients. This technique is applicable to both in vivo and in vitro conditions and can have a temporal resolution up to a millisecond scale (Grewe et al. 2010; Grienberger and Konnerth 2012).

However, reconstructing spiking activity from the recorded fluorescence traces is still challenging. This is mainly due to the different types of noise and artifacts, and to the intrinsic low temporal resolution of fluorescence transients compared with the timescale of action potentials. To reconstruct spiking activity from these data, several methods have been proposed, based on different techniques, including template matching (Grewe et al. 2010; Kerr et al. 2005), nonlinear supervised classifying (Sasaki et al. 2008), and deconvolution (Rahmati et al. 2016; Vogelstein et al. 2010; Yaksi and Friedrich 2006).

Although the established methods have improved the reconstruction accuracy over recent years, there is still a need for new methods that can *1*) further increase this accuracy, *2*) work fast on long-term data, *3*) be readily adaptable to data with different types of fluorescent transients, and *4*) minimize the need for user interaction and expertise in a specific method. In particular, long-term calcium imaging data, or data acquired at high sampling frequency (e.g., 500 Hz), may contain hundreds of thousands of frames, thereby effectively making most of the previously proposed methods impractical because of long computation times. Moreover, the amplitude as well as the rise and decay kinetics of fluorescence transients may differ within a fluorescence trace or under different experimental conditions, e.g., in recordings with different fluorescence calcium indicators or in recordings from immature (Rahmati et al. 2016; Takano et al. 2012) vs. adult neurons (Grewe et al. 2010; Kerr et al. 2005; Vogelstein et al. 2010). These differences are a challenging issue for most previously proposed techniques because of their dependency on a particular shape or specific kinetics (e.g., fast vs. slow rise kinetics) of fluorescence transient (e.g., see Grewe et al. 2010; Sasaki et al. 2008; Vogelstein et al. 2010). In practice, processing of new data often requires a manual reparameterization of the method, e.g., in the form of building a new transient template (Clements and Bekkers 1997; Grewe and Helmchen 2009; Kerr et al. 2005) or determining a new threshold for extracting inferred spiking activities (Vogelstein et al. 2010). These user interactions usually render the

Address for reprint requests and other correspondence: V. Rahmati, Neuroimaging, Technische Universität Dresden, Chemnitzer Str. 46B, 01187 Dresden, Germany (e-mail: vahid.rahmati@tu-dresden.de).

reconstruction accuracy of most established methods dependent on the user's experience.

In this article, we present a novel, heuristic method that can overcome these four challenges by encompassing the following four main features. First, from a given noisy fluorescence trace, the method can accurately reconstruct, simultaneously, not only the isolated spikes but also burst spikes and the spike count per fluorescence transient. Second, it is computationally fast, where spiking activities from a fluorescence trace with 1,000,000 time points are reconstructed in less than 2 s using a standard modern desktop computer. Third, it is based on a heuristic model-free algorithm, making it intrinsically adaptable to fluorescence transients with different rise and decay kinetics or amplitudes, both within or across single neurons. Fourth, it is a near-automatic method with only one central parameter, which can be set by the user to increase the reconstruction accuracy: this setting can be done once, based on a couple of fluorescence traces, for the whole data set, and thus effectively avoid the typical search for optimal parameters. Furthermore, to correct for several types of artifacts, the method uses a set of new algorithms or the techniques translated from analytical chemistry and machine learning. These artifacts include rather complex, slowly varying drifts or large, short-lasting deflections in fluorescence traces as frequently found in in vivo data.

As a proof-of-concept of the proposed method, we illustrate and quantify its high reconstruction accuracy by using both synthetic and experimental data. As synthetic data, we use data simulated under different noise conditions, neuronal firing rates, and sampling frequencies. As experimental data, we use two in vitro and one in vivo data set. With the in vitro data we show that the method can cope with both slow and fast rise kinetics. With the in vivo data set we demonstrate the artifact correction capabilities of the method. Finally, we compare the reconstruction accuracy of this new method with that of a set of established reconstruction methods.

METHODS

Overview

The method is composed of five main components (Fig. 1): *1*) preprocessing, *2*) reconstruction, 3) timing correction, 4) spike count estimation, and 5) demerging. Given a raw fluorescence trace, the method can reconstruct the timing and count of spiking activities. We refer to our approach as "UFARSA," an acronym for "ultra-fast accurate reconstruction of spiking activity." We describe each of the five components below.

Preprocessing

The preprocessing consists of four steps: *1*) normalization, *2*) slow drift removal, *3*) deflection removal, and *4*) smoothing. Normalization and smoothing (*steps 1* and *4*) are both mandatory steps, and the removal of slow drifts and deflections (*steps 2* and *3*) is optional.

Normalization. For a fluorescence trace $F(t)$ (given in pixel values or photon counts), we first use the following normalization: $F(t) \leftarrow [F(t) - F_0]/\max(F_0, 1)$, where F_0 is the time-averaged intensity of the

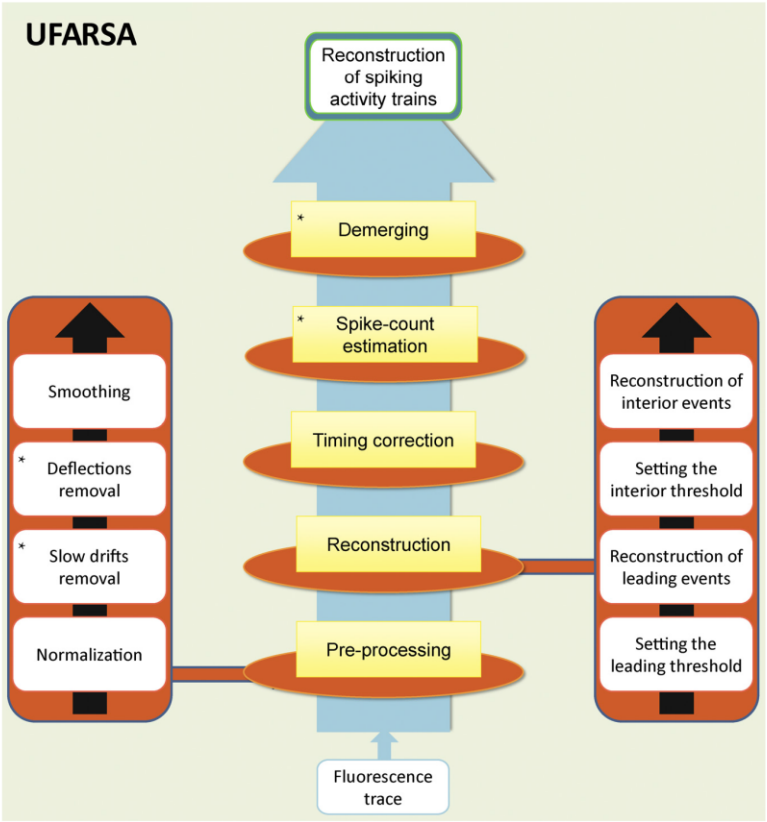

Fig. 1. Illustration of the ultra-fast accurate reconstruction of spiking activity (UFARSA) method. Flowchart illustrates the main components of UFARSA (yellow blocks): *1*) preprocessing, *2*) reconstruction, *3*) timing correction, *4*) spike count estimation, and *5*) demerging. The given fluorescence trace (*bottom*) is processed by these 5 steps, and the output is the reconstructed event and spike count trains (see METHODS for details). The side blocks illustrate the substeps of the preprocessing and the reconstruction. Blocks designated by a star are optional to use.

given $F(t)$; i.e., F_0 = mean [$F(t)$]. Hereafter, we refer to this normalized trace as the given fluorescence trace $F(t)$.

Slow drift removal. Fluorescence traces may contain slowly varying drifts due to, for example, photobleaching or animal and mechanical movements. To increase the reconstruction accuracy, these low-frequency components (the baseline) are usually removed before the reconstruction process. This common step is typically performed by other reconstruction methods using rather simple detrending or filtering methods (Rahmati et al. 2016; Vogelstein et al. 2010). However, we found in preliminary analyses that such drift removal methods may not be able to effectively handle the relatively complex slowly varying drifts, which are frequent in in vivo data. Accordingly, we adopted a well-established method termed BEADS (baseline estimation and denoising with sparsity; Ning et al. 2014). BEADS was originally applied successfully to noisy chromatogram data but to our knowledge has not been applied to calcium imaging data before.

In brief, BEADS (Ning et al. 2014) models a given trace $y(t)$ as $y(t) = x(t) + f(t) + w(t)$, where $x(t)$ represents the numerous peaks and is modeled as a sparse derivative signal, $f(t)$ represents the slow-drift, baseline signal and is modeled as a low-pass signal, and $w(t)$ represents a stochastic residual and is modeled as a stationary white Gaussian process. To encapsulate these nonparametric models, BEADS uses a convex optimization problem formulation and converges to a unique optimal solution through a robust, computationally efficient iterative algorithm. BEADS aims at a simultaneous estimation of $x(t)$ and f(t) from the given trace. This can, in principle, enable BEADS to correct for the baseline with a higher accuracy, compared with, for example, using a high-pass filter solely. In addition, for the filtering, BEADS uses zero-phase, noncausal, recursive filters. Accordingly, it does not introduce shifts in the timing of fluorescence transients. For the full details of BEADS, see Ning et al. (2014). The filter has two parameters, namely, its order and its normalized cutoff frequency (f_{beads}), which we set to 1 and 0.002 cycles/sample in this article; in general, $0 < f_{\mathrm{beads}} < 0.5$ cycles/sample. Moreover, we set three regularization parameters of the optimization problem as well as the asymmetric ratio parameter to 1; the latter renders the BEADS's penalty function symmetric. When applied to new data, f_{beads} may need to be adjusted. To implement BEADS as a part of UFARSA, we used its publicly available MATLAB code (https://de.mathworks.com/matlabcentral/fileexchange/49974-beads–baseline-estimation-and-denoising-w-sparsity-chromatogram-signals-). We also implemented a fast version of this code, which provides for qualitatively similar results.

For UFARSA, we use the BEADS method only for a reliable slow drift removal (see RESULTS), but without any noise reduction typically done by BEADS. This is because we found that this noise reduction may lead to an oversmoothing of the fluorescence transients. Accordingly, for a given fluorescence trace $F(t)$, the detrended (or drift free) trace $F_{\mathrm{det}}(t)$ is computed as $F_{\mathrm{det}}(t) = F(t) - f(t)$. The baseline of $F_{\mathrm{det}}(t)$ is zero. Importantly, the locations of the transients' onsets and peaks remain reliably unchanged relative to the given fluorescence trace. This is of course relevant for an accurate timing reconstruction of spiking activities, because the onset of a fluorescence transient is closely related to the timing of its underlying spiking activity (Grewe et al. 2010).

Deflections removal. Recorded fluorescence traces may suffer from short-lasting or impulse-like, large deflections. These artifacts may occur due to, for example, brief animal movements or flashes used for synchronizing optical and electrical recordings. In practice, such traces are usually either manually corrected through an interactive, time-consuming procedure based on visualization of the data or simply discarded from further analysis. To address this issue, we propose a simple algorithm that can effectively remove the deflections automatically, thereby providing more suitable input to the following analysis steps. The algorithm is based on the idea that these artifacts will usually appear as outliers in the distribution of fluorescence intensities of a given trace. To apply this algorithm, the trace needs to be free of slowly varying drifts (see *Slow drift removal*).

We treat positive and negative outliers in different ways. For the negative outliers, we first compute the Pct_{neg}-th percentile of the negative fluorescence intensities (or simply, negative percentile level) of the drift-free trace. We then set the intensities, which are more negative than the computed percentile value, equal to one-half this percentile value. For representative results showing the performance of this algorithm in this article (see RESULTS), we set Pct_{neg} to 2, where a larger Pct_{neg} can lead to a less negative percentile value.

For the positive outliers, we restrict our algorithm only to the large impulses to avoid misinterpretation of large fluorescence as outliers. We first compute the Pct_{pos}-th percentile of the positive fluorescence intensities (or simply, positive percentile level) of the drift-free trace. For any impulse with intensity greater than three times the computed percentile value, we replace its value by the average intensity of its two adjacent neighboring time points. By default, we set Pct_{pos} to 98, where a larger Pct_{pos} can lead to a more positive percentile value.

Smoothing. Fluorescence traces acquired, for example, in high-speed recordings and in vivo recordings, are usually contaminated by relatively high levels of high-frequency noise. To increase the reconstruction accuracy of UFARSA, this noise needs to be reduced. To do this, we use a well-established smoothing method, which allows for an unsupervised and robust noise reduction of one-dimensional (1-D) or N-D gridded data; this method is usually called SMOOTHN (Garcia 2010). This method is fast, fully automated, and has been already successfully applied to a wide range of data such as particle image velocimetry (Garcia 2011). In this work, we propose to apply this method to fluorescence traces.

For equally spaced data (e.g., calcium imaging data recorded at a fixed recording sampling frequency), SMOOTHN performs the smoothing based on the discrete cosine transform and a penalized least-squares method. In SMOOTHN, the degree of smoothing is controlled by a real positive scalar number S (smoothing parameter); increasing S yields a stronger smoothing of the given data. Of note, this parameter has a direct effect on the penalty term in SMOOTHN, which reflects the roughness of the smoothed data. The value of S is determined automatically in SMOOTHN by means of minimizing a generalized cross-validation score. For more details, see Garcia (2010, 2011). To implement this method as a part of UFARSA, we used the publicly available MATLAB codes (https://de.mathworks.com/matlabcentral/fileexchange/25634-robust-spline-smoothing-for-1-d-to-n-d-data?focused=6600598&tab=function). For a given fluorescence trace, we denote the smoothed trace by $F_{\mathrm{smth}}(t)$.

Reconstruction

We classify the spiking activities into two classes: leading events and interior events. A leading event refers mainly to an isolated spike, the first spike of a burst, or the spike underlying the first fluorescence transient of several superimposed transients (see RESULTS). An interior event refers mainly to a within-burst spike, or the spike underlying a superimposed fluorescence transient following that first, i.e., the leading, transient.

Reconstruction of spiking activity is done in four steps: *1*) setting a leading threshold, *2*) reconstruction of leading events, *3*) setting an interior threshold, and *4*) reconstruction of interior events. Below, we describe these four steps.

Setting the leading threshold. The reconstruction accuracy of UFARSA relies effectively on the leading-event detection threshold (or simply, leading threshold), denoted by Thr_{leading}. This threshold is used to detect the fluorescence transients mediated by the leading events (or simply, leading transients). To set Thr_{leading}, we use a new simple algorithm that sets it as a scale of the noise level. First, we compute the trace (i.e., time series) of the noise, $Noise(t)$, as the residual of the difference between the smoothed trace $F_{\mathrm{smth}}(t)$ and the trace to which the smoothing was applied ($F^{\mathrm{pre}}_{\mathrm{smth}}(t)$); i.e., $Noise(t)$ =

$F^{pre}_{smth}(t) - F_{smth}(t)$. Second, we compute the standard deviation of the noise as $SD_{noise} = 1.4826 \times MAD_{noise}$, where MAD_{noise} is the median absolute deviation of the $Noise(t)$; i.e., $MAD_{noise} = \text{median}\{|Noise(t) - \text{median}[Noise(t)]|\}$. Third, we estimate a minimum leading threshold as $Thr^{min}_{leading} = Pct^{val}_{pre\text{-}pos}/Coeff^{pre}_{Pct}$, where $Pct^{val}_{pre\text{-}pos}$ is the value of the Pct^{pre}_{pos}-th percentile of the positive fluorescence intensities in $F^{pre}_{smth}(t)$, and the minimum leading threshold scaling constant $Coeff^{pre}_{Pct}$ is used to scale $Pct^{val}_{pre\text{-}pos}$. We set $Pct^{pre}_{pos} = 98$ and $Coeff^{pre}_{Pct} = 6$; a larger $Coeff^{pre}_{Pct}$ can lead to a smaller $Thr^{min}_{leading}$ that acts as a lower bound for $Thr_{leading}$ (see the following text). Finally, the leading threshold is set as $Thr_{leading} = \max(Thr^{min}_{leading}, Coeff^{SD}_{leading} \times SD_{noise})$, where $Coeff^{SD}_{leading}$ is a constant scaling of SD_{noise}; we call it the leading threshold scaling constant. Note that $Coeff^{SD}_{leading}$ effectively controls the value of the $Thr_{leading}$ and is the only parameter that is required to be set by the user. To support the user in this task, $Coeff^{SD}_{leading}$ can be directly estimated from fluorescence data. First, for all traces of the same recording, the user needs to apply UFARSA to a couple of fluorescence traces and read off the UFARSA-estimated SD_{noise} values for each of them. This is followed by an inspection of the smoothed version of these traces [i.e., $F_{smth}(t)$ traces] to estimate the expected minimum noise-free amplitude of the leading transients ($A^{min}_{leading}$; minimum leading amplitude). The user can then roughly estimate (but not overestimate) $Coeff^{SD}_{leading}$ as the ratio of $A^{min}_{leading}$ and SD_{noise} based on these traces. To avoid overestimating $Coeff^{SD}_{leading}$, the user can *1*) preferably select traces with apparently more variable transient amplitudes, and *2*) after estimating $A^{min}_{leading}$, set it as, e.g., $A^{min}_{leading} \leftarrow A^{min}_{leading} \times 0.8$.

We found that this data-driven approach yields robust and accurate results (see RESULTS). Moreover, note that whereas $Coeff^{SD}_{leading}$ is constant for the whole data set, $Thr_{leading}$ is adapted internally in a trace-specific manner, because of the dependence on the estimated SD_{noise}. In this article, to report our results, we set $Coeff^{SD}_{leading} = 2.25$ (default value), unless stated otherwise.

Reconstruction of leading events. Based on the smoothed fluorescence trace $F_{smth}(t)$ and the computed leading detection threshold $Thr_{leading}$, UFARSA uses the following new algorithm to reconstruct the leading events. First, we extract all fluorescence transients that are potentially caused by a leading event or an interior event (e.g., a spike in a burst after the leading spike): for the whole $F_{smth}(t)$, we search for the individual time points around which the sign of the first derivative of $F_{smth}(t)$ [i.e., $\dot{F}_{smth}(t)$] changes from negative (or zero) to positive. We assume such time points as the onsets of candidate fluorescence transients and collect them in a vector called T^{onset}_{cands}. We then find the individual time points at which the rising phase of each candidate transient ends: following the onset of a candidate transient, we consider the first time point at which the sign of $\dot{F}_{smth}(t)$ changes from positive (or zero) to negative as the end of the rising phase of that transient. We denote the onset time point and the end time point of the i-th candidate transient by t^i_{onset} and t^i_{end} and define its amplitude as $A^i = F_{smth}(t^i_{end}) - F_{smth}(t^i_{onset})$. In general we find that the identified onset time points, end time points, and amplitudes are not affected considerably by noise, because we use the smoothed fluorescence trace for computing them. Nevertheless, in the timing correction step below, we still attempt to compensate for potential noise effects, which may be pronounced under high-noise conditions.

Second, for each candidate, we check whether its amplitude is larger than $Thr_{leading}$. If yes, we consider that candidate as a detected leading transient, which encodes a leading event occurring at the reconstructed time equal to the t_{onset} of that candidate. If not, we then check whether this candidate encodes an interior event (see *Setting the interior threshold* and *Reconstruction of interior events*). If it was not encoding an interior event, we remove that transient from the candidates and set its value in T^{onset}_{cands} to zero.

Setting the interior threshold. Following the detection of leading events as described above, UFARSA can start reconstructing the interior events. To this end, it first estimates the interior-event detection threshold (or simply, the interior threshold), denoted by $Thr_{interior}$. By using this parameter, the candidate fluorescence transients for being mediated by the interior events will be selected for further checks (see *Reconstruction of interior events*). To compute $Thr_{interior}$, we use the following simple algorithm in which $Thr_{interior}$ is set as a scale of the minimum amplitude of the interior transients, estimated from the detected leading transients.

First, we estimate the minimum amplitude of interior transients in $F_{smth}(t)$ (we denote this parameter by $A^{min}_{interior}$ and refer to it as minimum interior amplitude). To do this, we compute the median of the amplitudes of the detected leading transients (see *Reconstruction of leading events*) and take the average over those detected leading amplitudes that are smaller than this median. We then bound this parameter: if the ratio of the maximum detected leading amplitude ($A^{max}_{leading}$) to $A^{min}_{interior}$ (i.e., $A^{max}_{leading}/A^{min}_{interior}$) is larger than the maximum spike count constant n^{max}_{count}, we use the following mapping: $A^{min}_{interior} \leftarrow A^{max}_{leading}/n^{max}_{count}$. Although in our implementation we also made it possible to skip this bounding, in general it can preclude UFARSA from underestimating $A^{min}_{interior}$; such underestimation may cause an overestimation of the spike counts per transient (see *Reconstruction of interior events*). For example, because in regular calcium imaging recordings from somata each fluorescence transient may encode up to five spikes, the best results may be obtained by informing UFARSA about such biological constraints. Accordingly, in this article, we set $n^{max}_{count} = 5$. In addition, in a mandatory bounding step, we constrain $A^{min}_{interior}$ to be greater than $Thr_{leading}$ by setting $A^{min}_{interior} \leftarrow \max(Thr_{leading}, A^{min}_{interior})$.

Having determined $A^{min}_{interior}$, we compute the interior threshold as $Thr_{interior} = Coeff^{amp}_{interior} \times A^{min}_{interior}$, where the minimum interior amplitude scaling constant $Coeff^{amp}_{interior} = 0.2$; that is, $Thr_{interior}$ is equal to 20% of $A^{min}_{interior}$. Clearly, increasing $Coeff^{amp}_{interior}$ will make UFARSA select candidate interior transients with larger amplitudes. To increase the accuracy of reconstruction of interior events, we further lower-bound the estimated interior threshold by taking the noise level into account. To do this, we set $Thr_{interior} \leftarrow \max[\min(Coeff^{thr}_{interior}, Coeff^{SD}_{leading}) \times SD_{noise}, Thr_{interior}]$, where $Coeff^{thr}_{interior}$ is the minimum interior threshold scaling constant, which we set to 0.75 (i.e., 75%), and $\min(Coeff^{thr}_{interior}, Coeff^{SD}_{leading})$ ensures that the lower bound is effectively smaller than $Thr_{leading}$. Clearly, setting $Coeff^{thr}_{interior} = 0$ will remove this lower bound.

Reconstruction of interior events. After computing $Thr_{interior}$, UFARSA will reconstruct the interior events. For those candidate fluorescence transients that were not detected as leading transients (see *Reconstruction of leading events*), we check whether they encode interior events. To do this, for each of such candidates (starting from the first one), we check the following three conditions: *1*) its amplitude must be larger than $Thr_{interior}$; *2*) in the vector T^{onset}_{cands}, the preceding onset time must be non-zero (this indicates that the current candidate follows a reconstructed leading event); and *3*) the fluorescence intensity at its onset must be at least $Plateau_{interior}$ percent greater than the amplitude of its preceding detected leading transient; we set $Plateau_{interior} = 0.25$ (i.e., 25%) and call it the interior plateau scaling constant. If the candidate transient fulfills all of these three conditions, an interior transient is identified. This transient is assumed to encode an interior event with a firing time equal to the onset time of the transient (i.e., t_{onset}). Otherwise, if not all three conditions are fulfilled, the candidate transient is ignored and we set its value in T^{onset}_{cands} to zero.

Timing Correction

Above, we described reconstruction of the timing of both leading and interior events. The reconstructed times were based on the onset times of the detected fluorescence transients in the smoothed trace $F_{\mathbf{smth}}(t)$. Clearly, these onset times may have experienced some time shifts compared with the given trace [$F(t)$] due to the applied preprocessing steps described earlier, especially the smoothing. Therefore, the reconstructed event times may need to be corrected. For this purpose, we propose the following algorithm in which we use both $F_{\mathbf{smth}}(t)$ and the nonsmoothed preprocessed trace [i.e., $F^{\mathrm{pre}}_{\mathrm{smth}}(t)$], rather than only $F_{\mathbf{smth}}(t)$ (see above), to correct the reconstructed onset times of both leading and interior detected transients.

First, we determine the rising phase of the s-th detected leading or interior transient in $F_{\mathbf{smth}}(t)$, based on its onset and end time points (i.e., t^s_{onset} and t^s_{end}), as $R^s_{\mathrm{smth}} = F_{\mathrm{smth}}(\Gamma^{'}_s)$, where $\Gamma^{'}_s = [t^s_{\mathrm{onset}}, t^s_{\mathrm{onset}} + 1, ..., t^s_{\mathrm{end}} - 1, t^s_{\mathrm{end}}]$. We then find the fluorescence intensities in $F^{\mathrm{pre}}_{\mathrm{smth}}(t)$ that correspond to this rising phase (i.e., during $\Gamma^{'}_s$) and define the vector of corresponding nonsmoothed intensities in $F^{\mathrm{pre}}_{\mathrm{smth}}(t)$ as $L^s_{\mathrm{noisy}} = F^{\mathrm{pre}}_{\mathrm{smth}}(\Gamma^{'}_s)$. We set $R^s_{\mathrm{smth}} \leftarrow R^s_{\mathrm{smth}} - \min(L^s_{\mathrm{noisy}})$ and $L^s_{\mathrm{noisy}} \leftarrow L^s_{\mathrm{noisy}} - \min(L^s_{\mathrm{noisy}})$.

Second, we search for the lag-free end time point of this detected transient in L^s_{noisy}, which we denote by $t^{s,\mathrm{actu}}_{\mathrm{end}}$. To do this, we first find the location of the maximum of the first derivative of R^s_{smth} and denote it by $t^{s,\mathrm{max}}_{\mathrm{smth}}$. We then find the location of the maximum of L^s_{noisy} during time points $[t^{s,\mathrm{max}}_{\mathrm{smth}} + 1, ..., t^s_{\mathrm{end}} - 1, t^s_{\mathrm{end}}]$ and denote it by $t^{s,\mathrm{max}}_{\mathrm{noisy}}$. We consider $t^{s,\mathrm{max}}_{\mathrm{noisy}}$ as an approximation to $t^{s,\mathrm{actu}}_{\mathrm{end}}$. We found that this algorithm provides a robust estimation of the actual end time point $t^{s,\mathrm{actu}}_{\mathrm{end}}$. In contrast, note that estimating $t^{s,\mathrm{actu}}_{\mathrm{end}}$ by simply setting it equal to the location of the maximum in L^s_{noisy} might be inaccurate. This is because whereas R^s_{smth} monotonically increases during $\Gamma^{'}_s$, L^s_{noisy} usually has some noisy fluctuations within this period. In particular, in high-noise fluorescence traces, there might be, for example, large noise-induced fluctuations in L^s_{noisy} that occur earlier than the actual end time point but within $\Gamma^{'}_s$.

Third, in L^s_{noisy} we search for the potential time points preceding the lag-free onset time point ($t^{s,\mathrm{new}}_{\mathrm{onset}}$), where we denote the vector containing those potential time points by $\Gamma^{''}_s$. To do this, we first define an upper bound for the small fluorescence intensities in the current detected transient as $UB^s = \min(R^s_{\mathrm{smth}}) + 0.25 \times A^s$, where the amplitude $A^s = F_{\mathrm{smth}}(t^s_{\mathrm{end}}) - F_{\mathrm{smth}}(t^s_{\mathrm{onset}})$. We compute the median of the intensities in R^s_{smth} that are smaller than UB^s and denote it by $median^s_{\mathrm{UB}}$. We refine UB^s by setting $UB^s \leftarrow median^s_{\mathrm{UB}} + 0.25 \times A^s$. We subtract UB^s from all intensities in L^s_{noisy}; i.e., $L^s_{\mathrm{noisy}} \leftarrow L^s_{\mathrm{noisy}} - UB^s$. We consider the time points with negative intensities in L^s_{noisy}, which precede $t^{s,\mathrm{actu}}_{\mathrm{end}}$ (see above), as $\Gamma^{''}_s$.

Finally, we estimate the corrected onset time point $t^{s,\mathrm{new}}_{\mathrm{onset}}$. To do this, we compute the first derivative of L^s_{noisy} for the time points between t^s_{onset} and one time point after $\Gamma^{''}_s$. Among the time points with negative derivate sign, we select the last one and add one time point. The result is our estimate of the actual onset $t^{s,\mathrm{new}}_{\mathrm{onset}}$ of the detected transient. We apply these correction steps to each of the detected leading transients and interior transients separately and obtain the corrected onset time vector $\mathrm{T}^{\mathrm{rec}} = \{t^{s,\mathrm{new}}_{\mathrm{onset}}\}$.

As was shown previously for the fluorescence traces acquired at high sampling frequencies (e.g., 500 Hz, OGB-1; Grewe et al. 2010), the spike underlying a fluorescence transient occurs almost at the transient's onset. However, this may not hold at lower sampling frequencies, e.g., 30 Hz, where it is likely that the spike-evoked calcium surge could have been sampled only after reaching its peak. Thus we implemented $\theta_{\mathbf{shift}}$ as an onset-shifting parameter in UFARSA, which is added to the corrected reconstructed event times; i.e., $\mathrm{T}^{\mathrm{rec}} = \{t^{s,\mathrm{new}}_{\mathrm{onset}} + \theta_{\mathrm{shift}}\}$. In this article, we set $\theta_{\mathbf{shift}} = 1$ time point.

We found in preliminary analyses that using the original detected amplitudes A^s typically yields more robust spike count estimation, in particular for high-noise data (see below). Therefore, we skip updating the amplitudes of the detected transients after correcting the timing.

Spike Count Estimation

Variability in the amplitudes of fluorescence transients in a given trace may encode the variability in the number of spikes underlying those transients. This case is usually observed in recordings with a sampling frequency lower than the underlying firing rate, where the transients of multiple spikes may be recorded as a single transient only; i.e., as a merged transient with one rising and one decaying phase [note that, in such a case, we found that there is not sufficient information in the recorded data about the onsets of individual within-burst (-like) transients]. In general, estimating the spike count per transient is challenging. This is mainly because of a nonlinear relationship between spike count and transient amplitude, which is often unknown (Rahmati et al. 2016; Vogelstein et al. 2010). To address this, we propose the following simple algorithm for estimating the "relative spike count" from the transient amplitude.

This processing step is applied to each fluorescence trace separately, and the spike count per detected transient is computed relative to the amplitudes of other detected transients in that trace. This is why we refer to it as a relative spike count. We restrict this estimation to the detected leading transients to avoid overestimating the spike count per detected interior transient. This is because the interior transients are, in general, less likely to encode >1 spike. Based on our computed minimum interior amplitude $A^{\mathrm{min}}_{\mathrm{interior}}$ (see *Setting interior threshold*), the relative spike count per detected leading transient is computed by dividing its amplitude by $A^{\mathrm{min}}_{\mathrm{interior}}$. More formally, the relative discrete spike count per the k-th reconstructed leading event is $count^k_{\mathrm{leading}} = \max[\mathrm{g}(A^k/A^{\mathrm{min}}_{\mathrm{interior}}),1]$, where the function $\mathrm{g}(\xi)$ is an imbalanced rounding: $\mathrm{g}(\xi^k) = \xi^k_{\mathrm{int}} + 1$ if the fractional-part of ξ^k is ≥ 0.75; otherwise $\mathrm{g}(\xi^k) = \xi^k_{\mathrm{int}}$, where ξ^k_{int} is the integer part of ξ. Compared with a simple rounding rule, we found that this function provides for more robust spike count estimations (see RESULTS). For the interior events, we set their spike count equal to 1.

Demerging

Because of the smoothing, the rising phases of neighboring fluorescence transients may be merged and appear as a single rising phase in the smoothed trace $F_{\mathbf{smth}}(t)$, mostly in low-frequency sampling. Accordingly, to increase the reconstruction accuracy of UFARSA, we introduce an optional demerging algorithm that attempts to reconstruct events from these merged transients.

We apply this algorithm only to those reconstructed leading events with $count_{\mathbf{leading}} > 1$. This is because such events, compared with, for example, the interior events, are more likely to have been reconstructed from a detected merged transient. To perform the demerging, we compute the second derivative of the refined (i.e., after application of the timing correction step), smoothed rising phase of each of the selected leading transients. We search for the time point around which the sign of this second derivative changes from negative (or zero) to positive. We consider any time point following the corresponding $t^{s,\mathrm{new}}_{\mathrm{onset}}$ of the transient, which fulfills this condition, as the timing of a new event. We denote the m-th such reconstructed event (or simply, reconstructed merged event) from the k-th leading event by $t^{k,\mathrm{m}}_{\mathrm{onset}}$. We found in preliminary analyses that these $t^{k,\mathrm{m}}_{\mathrm{onset}}$ do not usually deviate from their actual onset time points. Therefore, when applying the timing correction step to these reconstructed merged events, we only

apply the onset-shifting correction; i.e., we set $t^{k,m}_{onset} \leftarrow t^{k,m}_{onset} + \theta_{shift}$. We classify these reconstructed merged events as interior.

We also update the estimated relative spike counts. For any leading k-th event with at least one merged event, i.e., with $\eta^k \geq 1$ reconstructed merged events, we define $countd^{k,new}_{leading} = \max(countd^{k}_{leading} - \eta^{k}, 1)$. For all other leading and interior events, we set this quantity equal to their originally estimated spike counts.

Reconstruction of Spiking Activity Trains

After reconstructing the spiking activities, we next introduce four different representations of reconstructed spiking activity trains for a given fluorescence trace. These four representations will be used below to represent the reconstructed spiking activities using different measures (event times or spike counts) and reconstruction features (with or without applying the demerging step), as follows: *1*) event train $E(t)$, a binary vector with values of 1 at reconstructed event times, i.e., at $t^{s,new}_{onset}$; *2*) spike count train $C(t)$, which is the same as the first train, but the values of 1 are replaced by the reconstructed, relative discrete spike counts, i.e., $countd^{s}_{leading}$; *3*) demerged event train $E^{dem}(t)$, which is the same as the first train but superimposed by values of 1 at the reconstructed merged event times $t^{s,m}_{onset}$; and *4*) demerged spike count train $C^{dem}(t)$, which is the same as the demerged event train, but the values of 1 are replaced by $countd^{s,new}_{leading}$, to also take the reconstructed merged events into account. These four vectors have the same number of elements as the number of time points of the given fluorescence trace.

Generating Synthetic Data

To simulate fluorescence traces, we use the following standard procedure (e.g., see Vogelstein et al. 2010). First, we generate a train of events (i.e., spikes) through a Poisson process, with an expected mean firing rate of $\bar{\lambda}$ and a sampling frequency f_s. Second, we convolve this Poisson spike train with a decaying exponential having a time constant of τ_d and an initial amplitude of A_{exp} (we set $A_{exp} = 1$). This will produce a trace of Ca^{2+} concentration ($[Ca^{2+}]$) kinetics, where each single-spike-evoked calcium transient has an expected amplitude of A_{exp}. Finally, to map the $[Ca^{2+}]$ kinetics to fluorescence intensities, we assume the following relationship: $F(t) = [Ca^{2+}] + \varepsilon_t$, where ε_t is the additive white Gaussian noise with a standard deviation of σ_{noise} and zero mean.

Comparison to Other Methods

We compare the reconstruction accuracy of UFARSA with that of three spike reconstruction methods, the first two of which are widely used: *1*) a template-matching method (Clements and Bekkers 1997), *2*) a deconvolution-based method (Vogelstein et al. 2010), and *3*) a neuronal deconvolution-based method (Rahmati et al. 2016). We compare methods on the basis of two different data sets that differ profoundly in the rise kinetics of the fluorescence transients.

As a template matching method, we used a widely used method that is based on an optimally scaled template (Clements and Bekkers 1997), as implemented in the pCLAMP 10.2 software package (Molecular Devices, Sunnyvale, CA). In the following we refer to this method as TM. To use TM, we first determined a distinct template for each of the two data sets. This was done in an initial, interactive phase by manually extracting a number of veridical fluorescence transients, using the available jointly measured electrophysiological signals. This was followed by fitting a template to an averaged transient. When this averaged template was used to extract spiking activities in a fluorescence trace, a detection criterion threshold (Thr_{TM}) needed to be set manually. This parameter captures the optimum scaling factor and the quality of fit (see Clements and Bekkers 1997 for more details). We used four different thresholds to reconstruct spiking activity from each individual trace in both data sets: $Thr_{TM} = 1$, 1.5, 2, and 2.5. To perform all these steps, we used pCLAMP 10.2 (for the exact details see Rahmati et al. 2016).

As a deconvolution-based method, we used another well-established state-of-the-art method called the fast filter technique (Vogelstein et al. 2010). In a probabilistic framework, this method infers the most likely spiking activities by performing a fast, nonnegative deconvolution of a given fluorescence trace. To do this, it uses a first-order generative model: a decaying exponential is convolved with a Poisson spike train to generate $[Ca^{2+}]$ kinetics, which are then converted to the fluorescence traces by using a linear (or saturating) mapping and additive Gaussian noise. The method assumes an instantaneous rise time for each evoked transient and a linear direct relationship between the transient amplitude and the spike count per time point. Based on this model, the method finds an approximation to the maximum a posteriori spike train for the given fluorescence trace. This approximation is the output of the fast filter, which needs a thresholding to extract the inferred spiking activities. This threshold, which we denote by Thr_{ff}, needs to be set manually (see RESULTS); for comparison, we covered the range between 0.05 and 1 in steps of 0.05. We used the publicly available MATLAB code of this method (https://github.com/jovo/fast-oopsi/) and initialized the parameters according to the main paper (Vogelstein et al. 2010).

As a neuronal deconvolution-based method, we used a recently published method called calcium imaging analysis using biophysical models and Bayesian inference (CaBBI; Rahmati et al. 2016). Similarly to the fast filter, it uses a probabilistic technique for deconvolving calcium imaging data. However, as generative models, this method uses biophysical neuronal models that link the membrane potential (rather than only the spikes) to the fluorescence intensities. We used two different generative models proposed by CaBBI that are based on the quadratic Gaussian integrate-and-fire (QGIF) neuron model or the FitzHugh-Nagumo (FHN) neuron model. For a given fluorescence trace, the generative model is inverted by using a variational Bayesian inference method. The outputs of CaBBI are the inferred neuronal dynamics such as membrane potential and $[Ca^{2+}]$ kinetics. By thresholding the inferred membrane potential, the spiking activity times can be extracted. We followed the main paper (Rahmati et al. 2016) to parameterize CaBBI as well as to set the threshold; we used a threshold of 0 mV. We implemented it by using its publicly available MATLAB code (http://mbb-team.github.io/VBA-toolbox/wiki/CaBBI/), implemented in the VBA toolbox (Daunizeau et al. 2014).

Measures of Reconstruction Accuracy

To quantify the event reconstruction and spike count reconstruction accuracies of UFARSA, we use two measures: *1*) the recently developed measure called spike time tiling coefficient (STTC; Cutts and Eglen 2014) and *2*) the Pearson correlation coefficient. STTC provides a more robust quantification of the pairwise correlation between two spike trains, compared with the widely used measures such as Pearson correlation coefficient. The only free parameter of STTC is the synchronicity window Δt: a range of $\pm\Delta t$ around each spike is considered for computing STTC (see Cutts and Eglen 2014 for more details). In this article, we use this measure to quantify the accuracy of reconstructed times of events (e.g., spikes) by computing the STTC between the trains of the reconstructed events and the true events (as determined using jointly measured electrophysiological data or simulated data). We denote this measure by $STTC_{event}$ and report its value by using a $\Delta t = 3$ time points (unless stated otherwise). Because STTC was originally developed for spike trains, we instead use the following measure to quantify the accuracy of the reconstructed spike counts: we compute the Pearson correlation coefficient between the firing rate traces generated on the basis of the trains of reconstructed spike count and the true spike count. We denote this measure by $PCorr_{count}$. To generate the corresponding firing rate traces, we convolve each spike count train with

a Gaussian kernel having a standard deviation σ_{FR} of 4 time points (unless stated otherwise). We report the values of $PCorr_{count}$, based on the chosen σ_{FR}.

In addition, we compute two error measures when comparing UFARSA's reconstruction accuracy to that of TM, CaBBI, and the fast filter methods: the number of missed events (*M*) and the number of falsely detected events (*FD*) (Rahmati et al. 2016) (see RESULTS).

RESULTS

We applied the proposed method UFARSA (ultra-fast accurate reconstruction of spiking activity) to both synthetic and experimental data. A flowchart illustrating the main components of the UFARSA is shown in Fig. 1 (see METHODS for more details). All parameter values of UFARSA were set according to Table 1, unless stated otherwise.

For all results shown, we report the reconstructed trains of events or spike counts, which were computed after the demerging step was applied (see METHODS); i.e., $E^{dem}(t)$ and $C^{dem}(t)$. For brevity, we drop the term "demerged" hereafter.

Synthetic Data

In the following we present several analyses with an increasing level of difficulty. Whereas the first examples, which correspond to low firing rates, should probably pose few problems to any reconstruction method and are considered illustrative examples, the later examples are more challenging representatives emulating cases with relatively high firing rate.

Example fluorescence traces. We first applied UFARSA to simulated calcium imaging data to show that it can accurately reconstruct spiking activities from fluorescence traces. Two examples of simulated fluorescence traces are shown in Fig. 2, *A* and *B*, which encode the spiking activity generated using the same Poisson spike train with a mean firing rate ($\bar{\lambda}$) of 0.4 Hz. The fluorescence trace in Fig. 2*B* was contaminated by a higher level of white noise [signal-to-noise ratio (SNR) $\approx$ 4] compared with that in Fig. 2*A* (SNR $\approx$ 20). Both traces contain fluorescence transients with typical (i.e., fast) rise kinetics. UFARSA can accurately reconstruct spiking events from both traces (Fig. 2, compare blue and red lines). To quantify the reconstruction accuracy, we computed $STTC_{event}$ as the spike timing tiling coefficient (Cutts and Eglen 2014) between the trains of reconstructed events and true events (see METHODS). $STTC_{event}$ was 1 and 0.97 for the examples in Fig. 2, *A* and *B*, respectively. Both these values indicate a highly accurate reconstruction.

The event reconstruction procedure in UFARSA can be described briefly as follows. For a given fluorescence trace (Fig. 2, *A* and *B*), UFARSA starts by a sign-change analysis of the first time derivative (Fig. 2, *C* and *D*) of its smoothed version, to find the candidate transients. Next, the rising phase and amplitude of each candidate are extracted. Based on these transient characteristics, transients encoding spiking events are detected, followed by a correction of their onsets. For more details, see Fig. 1 and METHODS, *Reconstruction*.

UFARSA also estimates the number of spikes per transient (Fig. 2, bluish lines) relative to the amplitudes of other detected transients in the given fluorescence trace: relative spike count (see METHODS); for brevity, we drop the term "relative" hereafter. This is useful because, for example, a single transient might have been evoked by >1 spike. Compared with the true spike counts (Fig. 2, orange circles), it can be seen that UFARSA can accurately estimate the spike counts under both noise conditions (Fig. 2, *A* and *B*). To quantify this accuracy, we compute $PCorr_{count}$ as the Pearson correlation coefficient between the firing rate traces generated on the basis of the reconstructed and true spike counts (see METHODS). $PCorr_{count}$ was 0.99 and 0.97 for Fig. 2, *A* and *B*, respectively.

Next, we applied UFARSA to simulated data with relatively high firing rates compared with the sampling frequency (f_s) of the optical recordings. One simulated example fluorescence trace ($\bar{\lambda} = 3, f_s = 40$ Hz) is shown in Fig. 3*A* (SNR $\approx$ 15). It can be seen that the fluorescence transients strongly overlap in this trace. This superimposition makes the reconstruction quite challenging, even under a high-SNR condition (Fig. 3*A*), mainly because the fluorescence transients are poorly discriminated. Reconstruction of such data becomes even more challenging when we contaminate this trace with a higher level of noise (Fig. 3*B*; SNR $\approx$ 3.5). We found that UFARSA can reconstruct event times and spike counts from both of these traces with high accuracy ($STTC_{event}$ = 0.99 and $PCorr_{count}$ =

Table 1. *Parameter values*

	Parameter	Value	Definition
Slow drift removal	f_{beads}	0.002 cycles/sample	Normalized cutoff frequency
Deflection removal	Pct_{neg}	2	Negative percentile level
	Pct_{pos}	98	Positive percentile level
Setting the leading threshold	$Coeff^{SD}_{leading}$	2.25	Leading threshold scaling constant
	$Coeff^{pre}_{Pct}$	6	Minimum leading threshold scaling constant
Setting the interior threshold	$Coeff^{thr}_{interior}$	0.75 (75%)	Minimum interior threshold scaling constant
	n^{max}_{count}	5	Maximum spike count constant
	$Coeff^{amp}_{interior}$	0.2 (20%)	Minimum interior amplitude scaling constant
Reconstruction of interior events	$Plateau_{interior}$	0.25 (25%)	Interior plateau scaling constant
Timing correction	θ_{shift}	1 time point	Onset shift
Generating synthetic data	f_s	30 Hz	Sampling frequency
	$\bar{\lambda}$	1 Hz	Mean firing rate
	A_{exp}	1	Transient amplitude
	τ_d	0.8 s	Transient decay time constant
Measures of reconstruction accuracy	Δt	3 time points	Synchronicity window
	σ_{FR}	4 time points	SD of Gaussian kernel

Value are default values of main parameters used. Main entries at left correspond to parts of METHODS where each parameter has been defined. All parameter values are consistent across the figures and tables, unless stated otherwise.

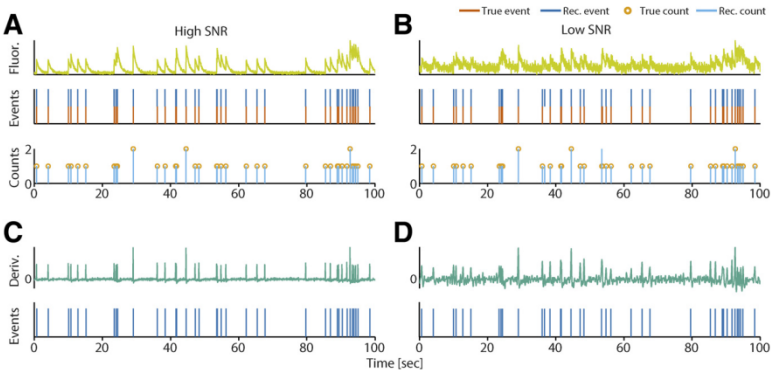

Fig. 2. Results of the proposed method (UFARSA) for synthetic data generated with a relatively low firing rate. *A*: reconstruction of spiking activities from a fluorescence trace with a high signal-to-noise ratio (SNR ≈ 20). *Top*, simulated fluorescence trace; *middle*, timing of true (red lines) and reconstructed (blue lines) spiking events; *bottom*, true (orange circles) and reconstructed (light blue lines) spike counts per event (or transient). *B*: same spiking events as in *A*, but with a higher level of white noise (SNR ≈ 4). UFARSA was able to accurately reconstruct both event times and spike counts, under both noise conditions. The reconstruction accuracy was quantified by the correlation between true and reconstructed spiking activities (see METHODS). In *A*, the spike time tiling coefficient between the trains of reconstructed and true events ($STTC_{event}$) = 1, and the Pearson correlation coefficient between the firing rate traces generated on the basis of reconstructed and true spike counts ($PCorr_{count}$) = 0.99; in *B*, $STTC_{event}$ = 0.97 and $PCorr_{count}$ = 0.97. *C*: the initial step of the event reconstruction in UFARSA relies on a derivative analysis of fluorescence intensities. *Top*, normalized, first time derivative of the smoothed version of the fluorescence trace shown in *A*; *bottom*, timing of reconstructed spiking events. *D*: same as *C*, but for the fluorescence trace shown in *B*. Simulation parameters in *A* and *B* were the mean firing rate ($\bar{\lambda}$) = 0.4 Hz and the sampling frequency of fluorescence traces (f_s) = 30 Hz. All other parameter values can be found in Table 1. Fluorescence intensity values are given in arbitrary units. The units and conventions are consistent across all figures, unless otherwise stated. Fluor., fluorescence; Deriv., first time derivative; Rec., reconstructed.

0.99 in Fig. 3*A*, and $STTC_{event}$ = 0.92 and $PCorr_{count}$ = 0.92 in Fig. 3*B*). Importantly, whereas some spikes seem to have been missed in the train of reconstructed event times, the reconstructed spike counts are still accurate. That is, based on the reconstructed spike counts, UFARSA was in fact able to extract those spikes, although with some timing error compared with their exact timing (see *insets* showing zoom-in views in Fig. 3, *A* and *B*). When we applied UFARSA to the same traces as in Fig. 3, *A* and *B*, but acquired at a higher sampling frequency (f_s = 400 Hz; Fig. 3, *C* and *D*), the reconstruction accuracy further increased ($STTC_{event}$ = 1 and $PCorr_{count}$ = 0.99 in Fig. 3*C*, and $STTC_{event}$ = 0.98 and $PCorr_{count}$ = 0.97 in Fig. 3*D*).

In sum, these results (Figs. 2 and 3) provide first evidence that UFARSA can accurately reconstruct event times and spike counts from fluorescence traces, even under conditions of relatively high firing rates and low SNR, acquired at low or high sampling frequencies.

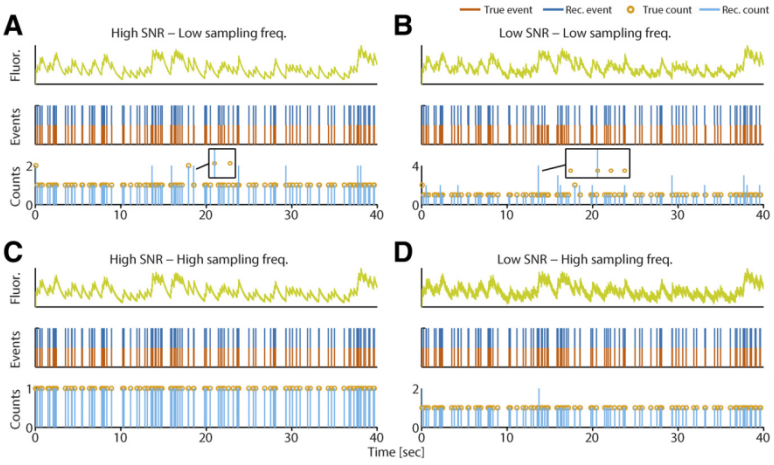

Fig. 3. Results of the proposed method (UFARSA) for synthetic data generated with a relatively high firing rate. *A*: same format as in Fig. 2*A*. The example fluorescence trace with a high signal-to-noise ratio (SNR ≈ 15) is generated by a Poisson spike train with a relatively high firing rate ($\bar{\lambda}$ = 3 Hz) compared with the sampling frequency (f_s = 40 Hz). *B*: the same fluorescence trace as in *A*, but under a low SNR (SNR ≈ 3.5). *Insets*: zoom-in views of spike counts around an example reconstructed event encoding >1 spike. UFARSA reconstructs both spike times and spike counts from these traces (*A* and *B*) with high accuracy. In *A*, the spike time tiling coefficient between the trains of reconstructed and true events ($STTC_{event}$) = 0.99, and the Pearson correlation coefficient between the firing rate traces generated on the basis of reconstructed and true spike counts ($PCorr_{count}$) = 0.99, and in *B*, $STTC_{event}$ = 0.92 and $PCorr_{count}$ = 0.92. *C* and *D*: same as *A* and *B*, respectively, but with a higher sampling frequency (f_s = 400 Hz). Results in *C* and *D* show that the reconstruction accuracy of UFARSA is increased at higher sampling frequencies: in *C*, $STTC_{event}$ = 1 and $PCorr_{count}$ = 0.99, and in *D*, $STTC_{event}$ = 0.98 and $PCorr_{count}$ = 0.97. Fluor., fluorescence; Freq., frequency; Rec., reconstructed.

Detailed quantification of UFARSA's performance. After showing high reconstruction accuracy of UFARSA in the anecdotal examples above, we next provide a detailed quantification of its performance based on synthetic fluorescence traces, simulated under experimentally plausible conditions. We investigated the reconstruction accuracy for different combinations of firing rate, SNR, and sampling frequency, as shown in Fig. 4, *A–D*. We varied the mean firing rate $\bar{\lambda}$ between 0.5 and 10 Hz, and the SNR between 3 and 20. As before, we quantified the accuracy on the basis of the correlation coefficient measures: $STTC_{event}$ and $PCorr_{count}$ (see METHODS). Note that each of these measures has a free parameter. For the $STTC_{event}$, the free parameter is the synchronicity window Δt, defining a range of $\pm\Delta t$ around each spike. For $PCorr_{count}$, it is the standard deviation of the Gaussian kernel (σ_{FR}) used to generate the firing rate traces of reconstructed and true spike counts. In Fig. 4, we show the results for $\Delta t = 2$ and 3 time points, and $\sigma_{FR} = 2$ and 4 time points.

The results in Fig. 4*A*, *left* ($\Delta t = 2$ time points) show that UFARSA can accurately reconstruct the event times for a wide range of the combinations of $\bar{\lambda}$ and SNR. Using a wider synchronicity window of $\Delta t = 3$ time points yielded higher $STTC_{event}$ values, implying a higher reconstruction accuracy (Fig. 4*A*, *right*). Practically, this means that the reconstructed event times had a higher correlation to the true event times when a larger timing error of ~3 time points was considered (Fig. 4*A*, *right*). Not surprisingly, the accuracy was reduced for a high mean firing rate $\bar{\lambda}$ (>5 Hz) and a low SNR (Fig. 4*A*). As with the anecdotal case studies (see Fig. 3), we found that a higher sampling frequency considerably improves the accuracy ($f_s = 400$ Hz; Fig. 4*B*). This is due to a better discrimination of the transients in the fluorescence trace at higher sampling frequencies, thereby enhancing the accuracy of reconstruction.

Furthermore, we quantified the accuracy of the reconstructed spike counts on the basis of $PCorr_{count}$. We found similar dependencies on the SNR and $\bar{\lambda}$ (Fig. 4*C*), as well as on f_s (compare Figs. 4*C* and 4*D*). In addition, increasing the parameter σ_{FR} (see Table 1) from 2 to 4 time points effectively improved $PCorr_{count}$ (i.e., accuracy). Especially at a low sampling frequency of 40 Hz, $PCorr_{count}$ values (Fig. 4*C*, *right*) were higher than $STTC_{event}$ values (Fig. 4*A*, *right*) for high $\bar{\lambda}$ (>5 Hz) and low SNR. In addition, this difference between the $STTC_{event}$ and $PCorr_{count}$ effectively vanished when a high sampling frequency was used (see Fig. 4*B*, *right*, and Fig. 4*D*, *right*, $f_s = 400$ Hz). These findings suggest that at a low sampling frequency, such as 40 Hz, for high $\bar{\lambda}$ (>5 Hz) and low SNR, some apparently missed event times might have been extracted with some timing error in the reconstructed spike counts (see also the *insets* in Fig. 3).

We also assessed how reconstruction accuracies are affected by the leading threshold $Thr_{leading}$, i.e., the central parameter of UFARSA, whose value is controlled by the leading threshold scaling constant $Coeff^{SD}_{leading}$ (via scaling the estimated SD of the noise in the fluorescence trace; see METHODS). To this end, we lowered $Coeff^{SD}_{leading}$ from its default value of 2.25 (Fig. 4,

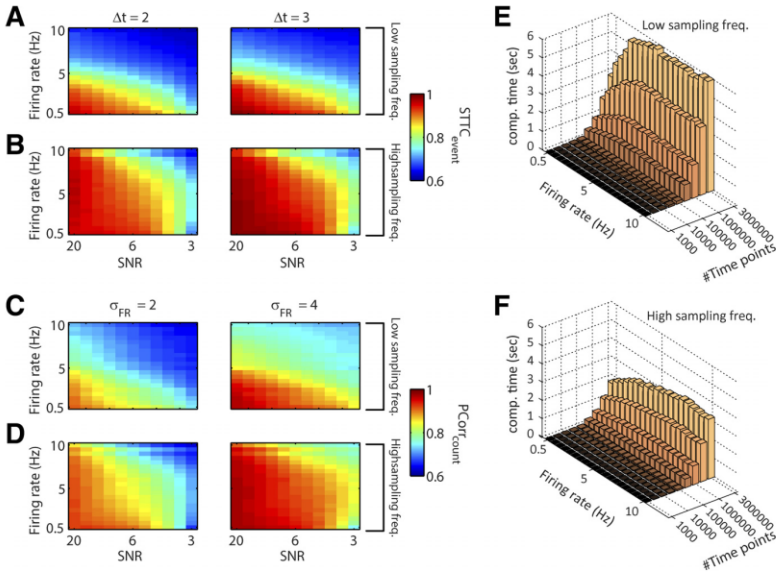

Fig. 4. Influence of experimental setting on reconstruction accuracy of UFARSA. *A*: event time reconstruction accuracy in terms of the spike time tiling coefficient ($STTC_{event}$) for fluorescence traces simulated with a mean firing rate ($\bar{\lambda}$) = 0.5, 1, ..., 10 Hz and a signal-to-noise (SNR) level ranging from 3 to 20. For each combination of $\bar{\lambda}$ and SNR, the shown color-coded value is the mean $STTC_{event}$ over 100 randomly generated fluorescence traces of 10 s. The leading threshold scaling constant ($Coeff^{SD}_{leading}$) and the sampling frequency (f_s) were 2.25 and 40 Hz, respectively. *Left*, $\Delta t = 2$ time points; *right*, $\Delta t = 3$ time points. *B*: same as *A*, but for $f_s = 400$ Hz. *C*: same as *A*, but for spike count reconstruction accuracy in terms of the Pearson correlation coefficient ($PCorr_{count}$). *Left*, standard deviation of the Gaussian kernel used to generate the firing rate traces (σ_{FR}) = 2 time points; *right*, $\sigma_{FR} = 4$ time points. *D*: same as *C*, but for $f_s = 400$ Hz. *E*: computation times. The 3-dimensional plot shows the computation times for reconstruction of a fluorescence trace (SNR ≈ 4, $f_s = 40$ Hz), including the mandatory preprocessing steps. For each combination of $\bar{\lambda}$ and number of time points (up to 3,000,000), each bar represents the mean reconstruction time over 10 randomly generated traces. *F*: same as *E*, but for a higher sampling frequency ($f_s = 400$ Hz). Freq., frequency; comp. time, computation time.

A–D) to 1.25 and recomputed the values of $STTC_{event}$ and $PCorr_{count}$ (not shown). The results were very similar to those in Fig. 4, *A–D*. This indicates that for these synthetic data, varying $Thr_{leading}$ in the suggested plausible range of $Coeff^{SD}_{leading}$ had minor effects on the reconstruction accuracy. However, we found that this is not always the case, as shown below.

Finally, we aimed at demonstrating typical computation times of UFARSA on a standard modern computer (Intel 3.70 GHz, 4 Cores, RAM usage <2 GB). We measured the overall time required by UFARSA to complete the reconstruction from a given fluorescence trace (referred to as "computation time" below). We included the mandatory steps of preprocessing (i.e., normalization and smoothing) and all other steps required to reconstruct event and spike count trains (see Fig. 1). We performed this quantification for different combinations of $\bar{\lambda}$ and number of simulated time points at f_s = 40 Hz (Fig. 4*E*) and f_s = 400 Hz (Fig. 4*F*). Strikingly, even for a fluorescence trace with 1 million time points and a high firing rate of $\bar{\lambda}$ = 10 Hz, the computation time was still less than 2 s when f_s = 40 Hz (Fig. 4*E*) and less than 1 s when f_s = 400 Hz (Fig. 4*F*); this implies the "ultra-fast" feature of our method. Naturally, the computation times showed a tendency to increase for higher number of time points (Fig. 4, *E* and *F*). The computation time for data with f_s = 40 Hz (Fig. 4*E*) took around 2 times longer than that for data with f_s = 400 Hz (Fig. 4*F*). This is expected because, for the same $\bar{\lambda}$ and number of time points, the expected number of spikes in a trace sampled at 40 Hz is around 10 times larger than that in a trace sampled at 400 Hz. This in turn increases the computation time, mainly due to the timing correction step (see METHODS).

In sum, these results (Fig. 4) show that UFARSA is, in practice, an ultra-fast reconstruction method whose high reconstruction accuracy can be preserved under a relatively wide range of SNRs, firing rates, and sampling frequencies.

Experimental Data

After showing the ability of UFARSA to accurately reconstruct event times and spike counts from synthetic data, we next applied it to recorded data. We used three previously published data sets: *1*) a data set of 25 in vivo fluorescence traces (with typical rise kinetics) recorded from layer 2/3 primary visual cortex neurons bolus loaded with the acetoxymethyl ester of the high-affinity calcium indicator Oregon green 488 BAPTA-1 (OGB1-AM; Kummer et al. 2012), *2*) a set of 6 in vitro joint fluorescence traces (with slow rise kinetics) and transmembrane current, recorded from immature CA3 neurons bolus loaded with OGB1-AM (publicly available at https://figshare.com/s/e524c1d214d411e5869c06ec4b8d1f61; Rahmati et al. 2016), and *3*) a data set of 12 in vitro joint fluorescence traces (with typical rise kinetics) and membrane potential, recorded from juvenile layer V somatosensory cortex neurons (publicly available at https://github.com/jovo/fast-oopsi/tree/master/data/), where cells were loaded with OGB1 through the recording pipette or bulk loaded with an acetoxymethyl ester of fura 2 (Vogelstein et al. 2010). For a detailed description of the data acquisition procedures (e.g., image segmentation or selection of regions of interest), see Kummer et al. (2012) for *data set 1*, Rahmati et al. (2016) for *data set 2*, and Vogelstein et al. (2010) for *data set 3*.

Artifact removal. Recorded calcium imaging data are usually contaminated by several types of artifacts, including slow and fast temporal drifts. Such artifacts can be pronounced and complex, especially under in vivo conditions. This makes reconstruction challenging for any reconstruction method. Accordingly, we briefly start by presenting the ability of UFARSA to correct for such artifacts. Although these presented illustrations are anecdotal showcases, we consistently found in all our analyses of experimental data that these artifact removal steps are reliable enough to enable accurate reconstructions.

Four in vivo fluorescence traces (of 25 in *data set 1*) are shown in Fig. 5. Rather complex, slowly varying drifts are evident in the first two traces (Fig. 5, *A* and *B*, green). These drifts are mainly due to minor tissue movements along the *Z*-axis. UFARSA was able to effectively remove such low-frequency components from the traces (Fig. 5, *A* and *B*, purple) by adopting a well-established method termed BEADS (see METHODS). BEADS was originally applied successfully to noisy chromatogram data (Ning et al. 2014). The baseline of the drift-corrected traces is zero. The two

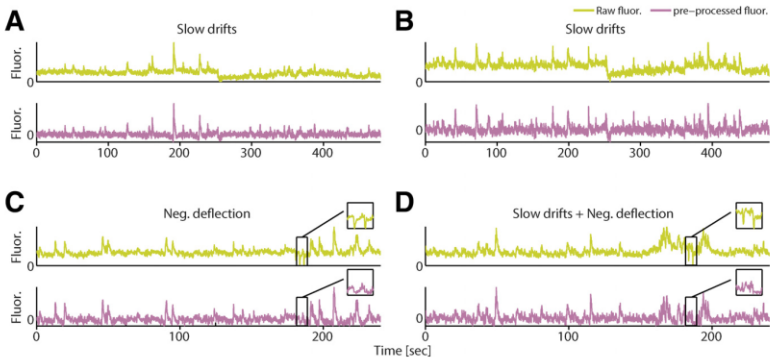

Fig. 5. The artifact-correcting capabilities of UFARSA. *A*: removing slowly varying drifts from an example in vivo fluorescence trace. *Top*, raw fluorescence trace with drifts; *bottom*, preprocessed fluorescence trace. *B*: same as *A*, but for a different example in vivo fluorescence trace. *C*: removal of large, short-lasting negative deflection artifact, in this example lasting ~0.5–1 s. *Inset*: zoom-in view around the deflection time. *Top*, raw fluorescence trace with deflections; *bottom*, preprocessed fluorescence trace. *D*: same as *C*, but for a different example in vivo trace, contaminated by both slow drifts and deflection artifacts. The results show that UFARSA is able to effectively correct for slowly varying drifts and large, short-lasting negative deflections. In *A–D*, the normalized cutoff frequency for drift removal (f_{beads}) = 0.005 cycles/sample, and the sampling frequency (f_s) = 8 Hz. Fluor., fluorescence; Neg., negative.

traces in Fig. 5, *C* and *D*, contain relatively large, short-lasting, negative deflection artifacts (here, lasting ~0.5–1 s). The deflections were due to brief animal movements. Note the trace in Fig. 5*D* has, in addition, rather complex drifts. We used a new, simple deflection correction (see METHODS; see Fig. 5, *C* and *D*, purple). No further reconstruction was applied to these traces because there were no joint electrophysiological recordings available to compare with the true spiking events.

Fluorescence transients with slow rise kinetics. Data recorded with new genetically encoded calcium indicators (Chen et al. 2013; Reiff et al. 2005) or recorded from neonate tissues (Kummer et al. 2016; Rahmati et al. 2016; Takano et al. 2012) may contain slow rise kinetics, lasting up to several hundred milliseconds. Although the majority of established reconstruction methods were applied to or developed on the basis of data with fast rise kinetics (see below), we believe it is useful that a method is robust against kinetic variations.

We applied UFARSA to in vitro fluorescence traces in *data set 2*, recorded from immature neurons (Fig. 6). These data had originally a very high SNR. Therefore, to make the reconstruction more challenging, we contaminated them with the background noise, similarly to Rahmati et al. (2016). Two representative fluorescence traces (of 6 in *data set 2*) under a high-SNR (~40) and a low-SNR (~2.75) condition are shown in Fig. 6. The fluorescence transients in these traces were evoked during spontaneous synchronized network activities that are expressed as so-called giant depolarizing potentials (GDPs) in individual immature neurons (Ben-Ari et al. 2007); note the *inset* in Fig. 6*A* shows an example slow-rising phase, which is typical for these transients. Because almost no information can be obtained from the shape of these GDP-mediated fluorescence transients about their underlying spike counts, we only report the reconstruction accuracy based on reconstructed event times (see Rahmati et al. 2016 for more details). UFARSA was able to accurately detect the onsets of GDPs (or simply GDPs) under both high SNR (Fig. 6, *A* and *C*) and, especially, low SNR (Fig. 6, *B* and *D*). To quantify the accuracy, similarly to the original study in which these data were analyzed (Rahmati et al. 2016), we computed the number of true events (n), missed events (M), and falsely detected events (FD), where the term "event" refers to GDP. Based on this quantification, $n = 8$, $M = 0$, and $FD = 0$ in Fig. 6, *A* and *B*; $n = 11$, $M = 0$, and $FD = 0$ in Fig. 6*C*; and $n = 11$, $M = 1$, and $FD = 0$ in Fig. 6*D*.

Overall, these results (Fig. 6) show that UFARSA can accurately detect the GDPs with slow rise kinetics from the fluorescence data recorded from immature tissues. This indicates that UFARSA is also, in principle, applicable to data recorded with new genetically encoded calcium indicators containing slowly rising transients.

Fluorescence transients with fast rise kinetics. We further applied UFARSA to *data set 3*, to assess its reconstruction accuracy for low-SNR in vitro fluorescence transients with typical (i.e., fast) rise kinetics and, in particular, considerably varying amplitudes. Two representative in vitro fluorescence traces (of 12 in *data set 3*) are shown in Fig. 7, *A* and *C*. The fluorescence transients in Fig. 7*A* were evoked by bursts, whereas those in Fig. 7*C* were evoked by either single spikes or bursts; note the true number of spikes per burst (third rows, brown). The transients evoked by individual within-burst spikes are poorly resolved in these traces, thereby making the reconstruction of within-burst spikes in principle challenging (see also Vogelstein et al. 2010). This can be seen in Fig. 7*A*, where UFARSA reconstructs all of the burst events (i.e., the onset of each burst) but cannot reconstruct the individual within-burst spikes. Moreover, UFARSA estimated the count per burst event as 1, whereas each burst has veridically 3 spikes (Fig. 7*A*, brown numbers). This is because UFARSA uses the variability in the amplitudes of leading transients (i.e., mainly, the non-within-burst transients; see METHODS) detected from a single fluorescence trace to estimate the spike counts per transient. However, in this example trace (Fig. 7*A*) there is almost no informative variability in the amplitudes of detected transients. In contrast, the trace shown in Fig. 7*C* contains transients with variable amplitudes. Accordingly, an increase in the reconstructed spike counts can be seen (Fig. 7*C*, bluish lines), but several event times were missed. These misses are due to the low SNR of this trace (see also Vogelstein et al. 2010). Nevertheless, for this trace, both event time and spike count reconstructions could be improved (Fig. 7*D*) by using a lower Thr_{leading}, through decreasing $Coeff^{\text{SD}}_{\text{leading}}$ from its de-

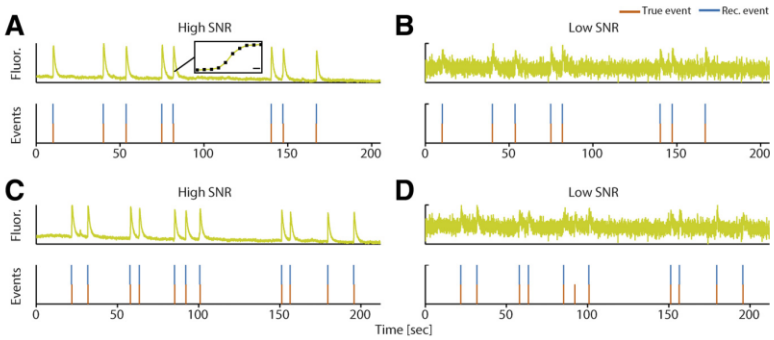

Fig. 6. Results of UFARSA for recorded data with slowly rising transients. *A*: same format as in Fig. 2*A*. The example is an in vitro fluorescence trace with high signal-to-noise ratio (SNR ≈40) containing the giant depolarizing potential (GDP)-mediated transients with slow rise times of around 350 ms. The true and reconstructed events refer to the onset (i.e., first spike) of each GDP event. The true event times were determined by using jointly measured electrophysiological recordings. *Inset*: zoom-in view around the rising phase of a representative GDP-mediated fluorescence transient. Scale bar, 45 ms. *B*: same fluorescence trace as in *A*, but under low-SNR condition (SNR ≈ 2.75). *C*: same conventions as *A*, but for a different example trace (SNR ≈ 40). *D*: same fluorescence trace as in *C*, but under low-SNR condition (SNR ≈ 2.75). Results in *A–D* show that UFARSA internally adapts to slowly rising transients, thereby performing an accurate reconstruction of the GDP's onset. The fluorescence traces were acquired at sampling frequency (f_s) = 22.6 Hz. Fluor., fluorescence; Rec., reconstructed.

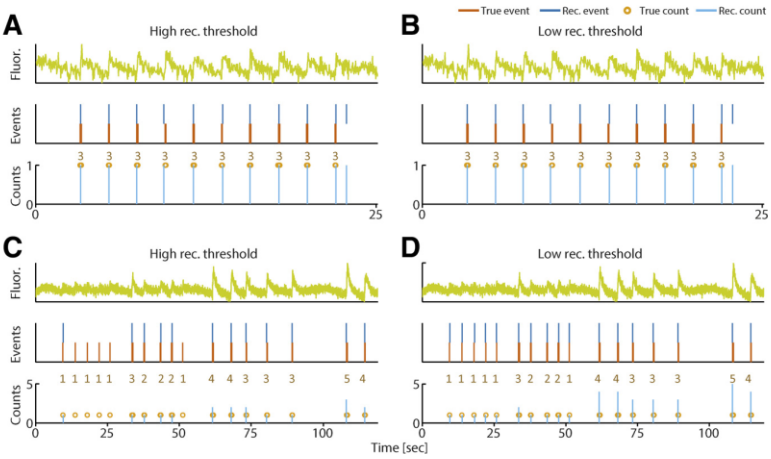

Fig. 7. Results of UFARSA for experimental data with typical fast rise kinetics. *A*: same format as in Fig. 2*A*. The example in vitro fluorescence trace contains transients with typical (i.e., fast) rise kinetics under low-SNR conditions. Brown numbers represent the true number of spikes per burst-evoked transient, according to the joint electrophysiological recordings. *B*: same as *A*), but a lower leading threshold (Thr_{leading}) was used for the reconstruction. Results in *A* and *B* show that for this trace, UFARSA was able to accurately reconstruct only the onset time of each burst event, but not its spike count, due to lack of informative variability in the detected fluorescence transients. *C*: same as *A*, but for a different fluorescence trace that contains transients evoked by single isolated spikes or burst of spikes (up to 5 spikes; brown numbers). *D*: same as *C*, but the reconstruction was performed using a lower Thr_{leading}. For this trace, the threshold lowering yielded detection of the transients evoked by isolated spikes, thereby improving the reconstructed spike counts. To set Thr_{leading}, the following values were used for the leading threshold scaling constant ($Coeff^{\text{SD}}_{\text{leading}}$): 2.25 (*A* and *C*) and 1.7 (*B* and *D*). Fluorescence traces were acquired at a sampling frequency (f_s) = 33 Hz.

fault value of 2.25 (Fig. 7*C*) to 1.7 (Fig. 7*D*). With this lower threshold, all missed events, and in particular the first four missed events (evoked by single spikes), in Fig. 7*C* can be reconstructed (Fig. 7*D*). These previously missed events have transients with the smallest amplitudes in this trace. This yielded an increase in the reconstructed spike counts of the next burst events in this trace (Fig. 7*D*). The remaining underestimation of some spike counts is mainly due to the strong fluorescence saturation and noise in this trace (Vogelstein et al. 2010). Figure 7*B* shows that lowering the threshold Thr_{leading} could not improve the spike count reconstruction of the trace in Fig. 7*A*. Again, there is a lack of informative variability in the amplitudes of transients in this trace. These results (Fig. 7) show that UFARSA is in general able to accurately reconstruct the event times and spike counts from fluorescence traces.

Quantitative Comparison to Other Methods

We next compared the reconstruction accuracy of our method, UFARSA, with that of three spike reconstruction methods (see METHODS): a template-matching method (TM) (Clements and Bekkers 1997), a deconvolution-based fast filter method (fast filter) (Vogelstein et al. 2010), and a neuronal deconvolution-based, Bayesian method (CaBBI) (Rahmati et al. 2016). To perform the comparison, we used *data set 2* (6 traces) and *data set 3* (12 traces), for which the joint electrophysiological signals were available as ground truth. Before the methods were applied, all fluorescence traces were corrected for slowly varying drifts. These in vitro drifts were relatively noncomplex (not shown) and thus could be sufficiently corrected by using the corresponding simple detrending method applied to each data set in its original paper: fourth-degree polynomial detrending for *data set 2* (Rahmati et al. 2016) and high-pass filtering for *data set 3* (Vogelstein et al. 2010). Note that the exact detrending method used does not seem important: applying the BEADS method in UFARSA yielded similar results (not shown) to the detrending methods originally used, without affecting the following comparison results. Because *data set 2* had high-SNR fluorescence traces, we lowered their SNRs to ~2.5 by adding the background noise so that the methods could be compared in a more challenging case (similarly to Rahmati et al. 2016; see also Fig. 6).

For the TM method, as is common practice, we used several detection criterion thresholds: Thr_{TM} = 1, 1.5, 2, and 2.5. For the fast filter method, we extracted the reconstructed spiking activities from the filter's output by using a threshold of Thr_{ff}. To set Thr_{ff}, we covered the range between 0.05 and 1 in steps of 0.05. For CaBBI, we considered 0 mV for thresholding the inferred membrane potentials. For UFARSA, we report the results by changing only its Thr_{leading}, based on the leading threshold scaling constant $Coeff^{\text{SD}}_{\text{leading}}$. To do this, we report the results in two cases: *1*) we vary $Coeff^{\text{SD}}_{\text{leading}}$ in the range between 0.75 and 2.5 in steps of 0.5, and *2*) we estimate $Coeff^{\text{SD}}_{\text{leading}}$, and thus Thr_{leading}, directly from fluorescence data (i.e., based on the data-driven approach) for each data set separately. For more details about the parameterization, see METHODS.

Comparison using data set 2. We first compared the four methods using the data with slow rise kinetics, *data set 2* (see above). Of interest is the detection of GDPs, where we compared methods on the basis of their GDP detection errors (n = 51 GDPs).

The detection errors of the four methods are listed in Table 2. Three of the methods (UFARSA, TM, and CaBBI) performed well with similar performance. UFARSA was optimal for a parameter of $Coeff^{\text{SD}}_{\text{leading}}$ = 1 or 1.5, CaBBI performed well for both the FHN and QGIF generative models, and TM performed best for Thr_{TM} = 2. The fast filter did not perform a reliable GDP detection from these data. This was expected,

Table 2. *GDP detection results for the four different methods (data set 2)*

Method	No. of Missed GDPs	No. of Falsely Detected GDPs
UFARSA		
$Coeff^{SD}_{leading} = 1$	0	0
$Coeff^{SD}_{leading} = 1.5$	1	0
$Coeff^{SD}_{leading} = 1.75$	5	0
$Coeff^{SD}_{leading} = 1.1$*	0	0
$Coeff^{SD}_{leading} = 1.3$*	1	0
CaBBI		
FHN	0	1
QGIF	2	1
Template matching		
$Thr_{TM} = 1$	0	74
$Thr_{TM} = 1.5$	0	1
$Thr_{TM} = 2$	3	2
$Thr_{TM} = 2.5$	18	0
Fast filter		
$Thr_{ff} = 0.65$	16	19
$Thr_{ff} = 0.7$	21	8
$Thr_{ff} = 0.75$	26	7

Values are GDP detection results of the proposed approach (UFARSA), calcium imaging analysis using biophysical models and Bayesian inference (CaBBI), template matching (TM), and the fast filter technique. For setting the leading threshold $Thr_{leading}$ in UFARSA, we used either 3 leading threshold scaling constants $Coeff^{SD}_{leading}$ (out of 0.75, 1.25, ..., 2.5) or two $Coeff^{SD}_{leading}$ values (*) estimated from fluorescence data; see text for more details. For CaBBI, we used both the FitzHugh-Nagumo (FHN) and quadratic Gaussian integrate-and-fire (QGIF) neuron models; for the TM method, 4 detection criterion thresholds (Thr_{TM}); and for the fast filter, 4 event detection thresholds (Thr_{ff}). For UFARSA and fast filter, the ranges of the three $Coeff^{SD}_{leading}$ (out of 0.75, 1, ..., 2.5) and three Thr_{ff} (out of 0.05, 0.1, ..., 1) include their optimal values. We applied the four methods to *data set 2* of in vitro fluorescence traces with slowly rising transients, under conditions of low signal-to-noise ratio (SNR $\approx$ 2.5). The total number of true GDPs was 51. The comparison shows that the proposed approach (UFARSA), CaBBI, and TM can detect the GDPs with high accuracy. However, there are 2 caveats for the results of TM; see main text. As expected, the fast filter method had relatively large detection errors because it was developed for fluorescence data with fast rising transients.

because the fast filter was originally developed for deconvolving transients with fast rise kinetics (Vogelstein et al. 2010).

In general, the results of each of these four methods depend on a specific parameter (in the case of CaBBI, which of the generative models is selected). For all methods, this parameter needs to be set manually to find the optimal value (Table 2). A practical issue is that without knowing the ground truth by relying on jointly measured electrophysiological data, determining the optimal value is, in practice, more of an art than a well-defined procedure. For example, without joint measurements, setting the thresholds Thr_{TM} and Thr_{ff} in the respective TM and fast filter methods will mainly depend on the user's experience with similar measurements. More precisely, in such a case, to set these thresholds, the user usually needs to (in each method separately) *1*) select an arbitrary, but plausible (based on user experience), range of Thr_{TM} and Thr_{ff} to perform the reconstruction, and then *2*) for each, or at least a few, fluorescence traces, visually compare the reconstructed events with the recorded transients, where *3*) the user needs to decide on optimal values of Thr_{TM} and Thr_{ff} based on that visual comparison. Clearly, this interactive search process may be challenging under high-noise conditions, for long-term recordings, or in regimes of particularly high firing rates. In practice, this search process may be time-consuming, and the results are dependent on the user's experience. For the TM method, the lack of joint measurements causes an additional difficulty in determining the template, due to lack of knowledge about the veridical fluorescence transients (see below).

Importantly, with UFARSA, one can effectively forgo such typical search processes and at the same time select robustly a near-optimal value for its central parameter (i.e., $Thr_{leading}$). To do this, one can in principle rely on estimating $Coeff^{SD}_{leading}$, and thus $Thr_{leading}$, directly from fluorescence data (see METHODS, *Setting the leading threshold*). Although this approach is based on manual selection, just as for TM and fast filter, it is based on determining a specific value that is directly accessible from the visualization of a couple of fluorescence traces. Importantly, this approach does not require any electrophysiological data, but of course having such data for only a few fluorescence traces is useful, for example, to derive a likely more accurate estimate of $Coeff^{SD}_{leading}$ (through deriving a more accurate estimate of $A^{min}_{leading}$; see METHODS), which can then be used for the rest of the data set, as well.

In Table 2, we also report the reconstruction results based on this data-driven approach for estimated $Coeff^{SD}_{leading}$ values by using only the fluorescence traces ($Coeff^{SD}_{leading} = 1.1$ and 1.3). Compared with varying, i.e., using different levels of $Coeff^{SD}_{leading}$, these results show that setting $Thr_{leading}$ by estimating $Coeff^{SD}_{leading}$ directly from data yields more robust results and, in principle, the search process for an optimal value can be avoided.

Note that there are two caveats for the TM method: *1*) TM requires an initial, interactive phase in which a template is determined for the actual reconstruction process, and *2*) TM takes advantage of having the template determined separately for each of the two data sets, based on the veridical fluorescence transients; i.e., those transients which had been extracted by harnessing the joint electrophysiological data. Without joint data, the determined template and thus the reconstruction results may become less accurate, especially for high-noise data, because deciding on the veridical transients for making the average template may be challenging. Beyond this, although not shown in this article, even by harnessing the joint measurements, the reconstruction accuracy of the TM method can considerably decrease in the presence of transients with different time courses than the template or the presence of overlapping transients (Clements and Bekkers 1997) in a given trace.

Comparison using data set 3. Next, we performed a comparison of the four methods on data with fast rise kinetics (*data set 3*), which were originally used to evaluate the fast filter (Vogelstein et al. 2010). In these data, the within-burst transients were poorly resolved where the burst spikes were mainly encoded by introducing an increase in the overall burst-evoked transient amplitude (e.g., see Fig. 7*D*). UFARSA and fast filter are capable of estimating the number of burst spikes by using the variability observed in transient amplitudes, whereas this is a limitation for CaBBI and TM (see also Rahmati et al. 2016). Accordingly, we performed the comparison in two stages. First, we compared all four methods on the basis of their accuracy in detecting the events of bursts (based on their onsets) and isolated spikes only (n = 149). Second, we compared only UFARSA and fast filter on the basis of their spike

count estimations, to quantify reconstruction performance of burst spikes.

We have listed the event detection errors of the four methods in Table 3. Based on both ways of setting $Thr_{leading}$ (see *Comparison using data set 2*), i.e., either by varying $Coeff^{SD}_{leading}$ or estimating $Coeff^{SD}_{leading}$ directly from data, UFARSA (for an optimal $Coeff^{SD}_{leading}$ of 1) was able to reconstruct the events equally as well as the TM method (for optimal Thr_{TM} of 1.5). For these data, both UFARSA and TM methods were better than fast filter (for the optimal Thr_{ff} of 0.35) and CaBBI. However, the two caveats of the TM method still apply: *1*) it requires an initial, interactive template-determining phase, and *2*) it uses the joint electrophysiological data to perform this phase.

Next, we compared the accuracy of reconstructed spike count traces of UFARSA and fast filter by using the correlation measure $PCorr_{count}$ (σ_{FR} = 4 time points). To do this, we considered the reconstruction results of UFARSA and fast filter obtained by their optimal event detection parameters in Table 3. Both UFARSA ($PCorr_{count} \approx 0.79 \pm 0.15$ for $Coeff^{SD}_{leading}$ = 1; 12 traces) and fast filter ($PCorr_{count} \approx 0.80 \pm 0.15$ for Thr_{ff} = 0.35; 12 traces) showed high and similar reconstruction performance. The difference between their results was not significant (paired, 2-sided Wilcoxon signed rank test).

Technical Guide for Using UFARSA

The MATLAB code implementation of UFARSA (with example scripts) can be downloaded as a UFARSA-master.zip file from https://github.com/VahidRahmati/UFARSA. The User_Guide.pdf describes how to use UFARSA, test it on demo scripts and sample data, and apply it to new data. In brief, UFARSA, as a near-automatic method, has only one central parameter, which can be set by the user to increase the reconstruction accuracy (see METHODS, *Setting the leading threshold* for a detailed description).

Note that UFARSA processes the fluorescence trace extracted for each region of interest (ROI; e.g., a single cell) separately. However, the user can provide UFARSA with a single data file containing the fluorescence traces of all ROIs, where UFARSA will process all traces as a batch job. Currently, UFARSA accepts the data files in either TXT or MAT formats, with the structures described in the User_Guide.pdf.

Table 3. *Event detection results for the four different methods (data set 3)*

Method	No. of Missed Events	No. of Falsely Detected Events
UFARSA		
$Coeff^{SD}_{leading}$ = 0.75	0	13
$Coeff^{SD}_{leading}$ = 1	6	5
$Coeff^{SD}_{leading}$ = 1.25	17	3
$Coeff^{SD}_{leading}$ = 1*	6	5
$Coeff^{SD}_{leading}$ = 1.15*	11	3
CaBBI		
FHN	10	20
QGIF	45	2
Template matching		
Thr_{TM} = 1	0	14
Thr_{TM} = 1.5	7	1
Thr_{TM} = 2	32	0
Thr_{TM} = 2.5	53	0
Fast filter		
Thr_{ff} = 0.3	3	40
Thr_{ff} = 0.35	11	15
Thr_{ff} = 0.4	19	10

Values are event detection results of the proposed approach (UFARSA), calcium imaging analysis using biophysical models and Bayesian inference (CaBBI), template matching (TM), and the fast filter technique. The same format is used as in Table 2. We applied the 4 methods to *data set 3* (in vitro fluorescence traces with typical fast rise kinetics), recorded under conditions with a low signal-to-noise ratio (SNR). The total number of true events was 149, where each event refers to an isolated spike or a burst onset. The comparison shows that UFARSA and TM perform better than CaBBI and fast filter.

DISCUSSION

We have presented a novel, heuristic, model-free method (called UFARSA, an acronym of ultra-fast accurate reconstruction of spiking activity) for the analysis of calcium imaging data. For both synthetic data and two sets of publicly available experimental test data, we showed that UFARSA can accurately reconstruct both individual spikes (isolated and in bursts) and the spike counts per fluorescence transient simultaneously. Importantly, we showed that its high reconstruction accuracy is robust under a wide range of experimentally plausible conditions, including a low SNR, different firing rates, and variability in transients' characteristics, including amplitudes as well as the rise and decay kinetics. We showed that UFARSA is, in practice, very fast and requires less than 2 s for processing a trace extracted from 1,000,000 frames. On the basis of in vivo data, we further demonstrated that it can effectively correct for a number of common artifacts in fluorescence traces. Critically, UFARSA has only one central parameter that can be set by the user once for the whole data set, based on a couple of fluorescence traces only; i.e., without requiring joint electrophysiological data.

Near-Automatic Reconstruction

To our knowledge, all established reconstruction methods have at least one parameter that needs to be set manually for new data acquired under a different setting. For example, setting such a parameter is required in template matching (extract a new template and threshold) or for the fast filter in the form of a threshold (e.g., see Table 2 and Clements and Bekkers 1997; Grewe et al. 2010; Kerr et al. 2005; Vogelstein et al. 2010). An issue is that finding an optimal setting without having jointly measured electrophysiological data is, in practice, not possible and is mainly based on the user's experience with the method and the data at hand. In contrast, UFARSA can perform reconstruction from different fluorescence data sets (e.g., differing in terms of transient shapes; see below) in a near-automatic manner. There are mainly two reasons for this. First, while still relying on a manual setting of its central parameter (i.e., the leading threshold), our described data-driven approach for setting this parameter (see METHODS) lets the user effectively avoid the search for an optimal value (e.g., see the description in RESULTS, *Comparison using data set 2*). This is in contrast to most established reconstruction methods (e.g., see Table 2 and Clements and Bekkers 1997; Grewe et al. 2010; Kerr et al. 2005; Vogelstein et al. 2010). Importantly, for all results shown in this article, we did not change the values of all other parameters of UFARSA (except for the optional, preprocessing drift-removal step) when we applied it to the

synthetic data and three different data sets (e.g., Figs. 4, 6, and 7). Nonetheless, the user should be aware that over- or underestimation of the leading threshold may decrease the reconstruction accuracy of UFARSA. This can be seen, for example, in Table 3, where decreasing the leading threshold determined from the data results in a larger number of falsely detected events, and increasing the leading threshold results in a larger number of missed events.

Second, UFARSA is a model-free method that can automatically (i.e., without requiring any manual setting) handle the variability in the transients' rise and decay kinetics presented within a trace or across traces, in contrast to most of the model- or template-based methods (Clements and Bekkers 1997; Grewe et al. 2010; Vogelstein et al. 2010). Such a difference can be found, for example, in recordings with different calcium indicators or between recordings from immature (Rahmati et al. 2016; Takano et al. 2012) (Fig. 6) and adult neurons (Kerr et al. 2005; Vogelstein et al. 2010). In addition, note that UFARSA uses the variability in transient amplitudes within a fluorescence trace to estimate the spike counts per transient, where the accuracy of this estimation may depend on the selected Thr_{leading} (e.g., see Fig. 7).

Ultra-Fast Reconstruction Process

Long-term calcium imaging and data acquired at a high sampling frequency (e.g., 1 kHz) can provide a rich data set for studying long-term neural activity patterns with a high temporal resolution (Grewe et al. 2010; Grienberger and Konnerth 2012), but there are at least two issues: *1*) increasing the sampling frequency in general effectively increases the noise, and *2*) there is a need for methods that can perform a fast reconstruction from these data with typically hundreds of thousands, or millions of frames. Regarding the first issue, we found that the benefits of a higher sampling frequency probably outweigh the disadvantage of an increased noise level (Figs. 3 and 4). Future studies are required to fully investigate this trade-off. With respect to the second issue, we have shown that UFARSA performs fast reconstruction, thereby enabling it to handle data sets with a large number of frames. In particular, we have shown that it takes less than 2 s for UFARSA to reconstruct spiking activities from a fluorescence trace with 1,000,000 time points. This means the reconstruction of data recorded from, for example, 20 neurons for 1,000 s at a 500-Hz sampling frequency will take less than 20 s. Evidently, UFARSA is much faster than previously proposed fast methods such as fast filter (Vogelstein et al. 2010), which requires around 1 s for deconvolving a trace of 50,000 time points.

Limitations

There are four limitations that, in practice, may cause suboptimal reconstruction results. First, the smoothing step of UFARSA may cause merging of some superimposed fluorescence transients. By proposing the demerging step (see METHODS), we made UFARSA able to demerge such transients and therefore reconstruct the underlying spikes. However, the demerging does not guarantee to demerge all such transients, especially under low-SNR conditions. Second, UFARSA performs the reconstruction mainly on the basis of the transient amplitudes. This can potentially make it sensitive to deflection artifacts in the fluorescence data, where it may misinterpret the upward phase of the deflections as the rising phase of fluorescence transients. Although we equipped UFARSA with a deflection removal algorithm (Fig. 5), there is still some room for improvement for handling the short-lasting "positive" deflections. Third, UFARSA estimates the spike counts per transient based on the variability in the amplitudes of transients presented in a trace, independently from other traces. However, in the absence of sufficient information, conveyed by transient amplitudes about their underlying spike counts, the accuracy of the reconstructed spike counts is likely to be reduced (e.g., Figures 7*A* and 7*B*). Fourth, although lowering the leading threshold can in principle increase the accuracy of estimated spike counts (e.g., compare Figs. 7*C* and 7*D*), it may in turn cause an overestimation of spike counts. This is because lowering the threshold makes the reconstruction more prone to a false detection of relatively small transients generated by the neuropil in close proximity to the soma under investigation. Because such transients usually have faster decay kinetics than somatic transients, UFARSA could potentially be further improved by considering the decay time constant of candidate transients.

Moreover, the optional, slow drift-removal algorithm of our method may misinterpret some very slow (relative to the timescale of spiking activity-evoked transients) fluorescence intensity changes, caused by nonspiking biological activities [e.g., generated by calcium-induced calcium release events or second messenger systems (Grienberger and Konnerth 2012)], as artifact and hence remove them. Although this should be a common limitation for unsupervised (or blind) baseline correction approaches (see also Rahmati et al. 2016; Vogelstein et al. 2010), the user should note that the slow drift removal may remove such slow activities, even with the BEADS approach (Ning et al. 2014) implemented in UFARSA.

Further Improvements and Extensions

A main component of UFARSA is the smoothing, where each fluorescence trace is smoothed separately. However, our adopted smoothing algorithm, called SMOOTHN (Garcia 2010, 2011), is applicable to 1-D or N-D gridded data. Therefore, a natural extension of UFARSA is to use the N-D feature of SMOOTHN by enabling it to be applied to the recorded image sequences (3-D) before the individual traces are extracted. This will provide a spatiotemporal smoothing of these data, which could prove more robust than a solely temporal 1-D smoothing based on single fluorescence traces. Such refined smoothing should in turn improve the reconstruction accuracy of UFARSA.

Similarly, UFARSA currently reconstructs the spike counts from each fluorescence trace separately. However, a more accurate spike count reconstruction may be achieved by considering the whole data set. That is, UFARSA can be extended to reconstruct spike counts based on the variability observed in the transient amplitudes of all traces, rather than of each trace independently. In this line, an alternative, but currently not implemented, way to improve the accuracy of the reconstructed spike counts might be to also consider the variability in the integral of transients (thus both decaying and rising phases), rather than the variability in the transient amplitudes solely.

GRANTS

This work was supported by Open Access Publication Funds of the Technische Universität Dresden, German Research Foundation Priority Program 1665 Grants HO 2156/3-1/2, KI 1816/1-1/2, and KI 1638/3-1/2, German Research Foundation Collaborative Research Center/Transregio 166/B3 (to K. Holthoff and K. Kirmse), Research Group FO 1738 Grant WI 830/10-2 (to K. Holthoff), Federal Ministry of Education and Research Grant 01GQ0923 (to K. Holthoff), and the Interdisciplinary Centre for Clinical Research Jena (to K. Kirmse and K. Holthoff).

DISCLAIMERS

The funders had no role in study design, data collection and analysis, decision to publish, or preparation of the manuscript.

DISCLOSURES

No conflicts of interest, financial or otherwise, are declared by the authors.

AUTHOR CONTRIBUTIONS

V.R., K.K., K.H., and S.J.K. conceived and designed research; V.R. performed experiments; V.R. analyzed data; V.R., K.K., K.H., and S.J.K. interpreted results of experiments; V.R. prepared figures; V.R. drafted manuscript; V.R., K.K., K.H., and S.J.K. edited and revised manuscript; V.R., K.K., K.H., and S.J.K. approved final version of manuscript.

REFERENCES

Ben-Ari Y, Gaiarsa JL, Tyzio R, Khazipov R. GABA: a pioneer transmitter that excites immature neurons and generates primitive oscillations. *Physiol Rev* 87: 1215–1284, 2007. doi:10.1152/physrev.00017.2006.

Chen TW, Wardill TJ, Sun Y, Pulver SR, Renninger SL, Baohan A, Schreiter ER, Kerr RA, Orger MB, Jayaraman V, Looger LL, Svoboda K, Kim DS. Ultrasensitive fluorescent proteins for imaging neuronal activity. *Nature* 499: 295–300, 2013. doi:10.1038/nature12354.

Clements JD, Bekkers JM. Detection of spontaneous synaptic events with an optimally scaled template. *Biophys J* 73: 220–229, 1997. doi:10.1016/S0006-3495(97)78062-7.

Cutts CS, Eglen SJ. Detecting pairwise correlations in spike trains: an objective comparison of methods and application to the study of retinal waves. *J Neurosci* 34: 14288–14303, 2014. doi:10.1523/JNEUROSCI.2767-14.2014.

Daunizeau J, Adam V, Rigoux L. VBA: a probabilistic treatment of nonlinear models for neurobiological and behavioural data. *PLoS Comput Biol* 10: e1003441, 2014. doi:10.1371/journal.pcbi.1003441.

Garcia D. Robust smoothing of gridded data in one and higher dimensions with missing values. *Comput Stat Data Anal* 54: 1167–1178, 2010. doi:10.1016/j.csda.2009.09.020.

Garcia D. A fast all-in-one method for automated post-processing of PIV data. *Exp Fluids* 50: 1247–1259, 2011. doi:10.1007/s00348-010-0985-y.

Grewe BF, Helmchen F. Optical probing of neuronal ensemble activity. *Curr Opin Neurobiol* 19: 520–529, 2009. doi:10.1016/j.conb.2009.09.003.

Grewe BF, Langer D, Kasper H, Kampa BM, Helmchen F. High-speed in vivo calcium imaging reveals neuronal network activity with near-millisecond precision. *Nat Methods* 7: 399–405, 2010. [Erratum in *Nat Methods* 7: 479, 2010.] 10.1038/nmeth0610-479d.

Grienberger C, Konnerth A. Imaging calcium in neurons. *Neuron* 73: 862–885, 2012. doi:10.1016/j.neuron.2012.02.011.

Kerr JN, Greenberg D, Helmchen F. Imaging input and output of neocortical networks in vivo. *Proc Natl Acad Sci USA* 102: 14063–14068, 2005. doi:10.1073/pnas.0506029102.

Kummer M, Kirmse K, Witte OW, Holthoff K. Reliable in vivo identification of both GABAergic and glutamatergic neurons using Emx1-Cre driven fluorescent reporter expression. *Cell Calcium* 52: 182–189, 2012. doi:10.1016/j.ceca.2012.05.004.

Kummer M, Kirmse K, Zhang C, Haueisen J, Witte OW, Holthoff K. Column-like Ca(2+) clusters in the mouse neonatal neocortex revealed by three-dimensional two-photon Ca(2+) imaging in vivo. *Neuroimage* 138: 64–75, 2016. doi:10.1016/j.neuroimage.2016.05.050.

Ning XR, Selesnick IW, Duval L. Chromatogram baseline estimation and denoising using sparsity (BEADS). *Chemometr Intell Lab Syst* 139: 156–167, 2014. doi:10.1016/j.chemolab.2014.09.014.

Rahmati V, Kirmse K, Marković D, Holthoff K, Kiebel SJ. Inferring neuronal dynamics from calcium imaging data using biophysical models and Bayesian inference. *PLoS Comput Biol* 12: e1004736, 2016. [Erratum in *PLoS Comput Biol* 12: e1004835, 2016.] doi:10.1371/journal.pcbi.1004736.

Reiff DF, Ihring A, Guerrero G, Isacoff EY, Joesch M, Nakai J, Borst A. In vivo performance of genetically encoded indicators of neural activity in flies. *J Neurosci* 25: 4766–4778, 2005. doi:10.1523/JNEUROSCI.4900-04.2005.

Sasaki T, Takahashi N, Matsuki N, Ikegaya Y. Fast and accurate detection of action potentials from somatic calcium fluctuations. *J Neurophysiol* 100: 1668–1676, 2008. doi:10.1152/jn.00084.2008.

Takano H, McCartney M, Ortinski PI, Yue C, Putt ME, Coulter DA. Deterministic and stochastic neuronal contributions to distinct synchronous CA3 network bursts. *J Neurosci* 32: 4743–4754, 2012. doi:10.1523/JNEUROSCI.4277-11.2012.

Vogelstein JT, Packer AM, Machado TA, Sippy T, Babadi B, Yuste R, Paninski L. Fast nonnegative deconvolution for spike train inference from population calcium imaging. *J Neurophysiol* 104: 3691–3704, 2010. doi:10.1152/jn.01073.2009.

Yaksi E, Friedrich RW. Reconstruction of firing rate changes across neuronal populations by temporally deconvolved Ca^{2+} imaging. *Nat Methods* 3: 377–383, 2006. doi:10.1038/nmeth874.

4.3. Manuscript III

Developmental Emergence of Sparse Coding: A Dynamic Systems Approach

Vahid Rahmati, Knut Kirmse, Knut Holthoff, Larse Schwabe, Stefan J. Kiebel

www.nature.com/scientificreports

SCIENTIFIC REPORTS

OPEN

Developmental Emergence of Sparse Coding: A Dynamic Systems Approach

Received: 31 January 2017
Accepted: 25 September 2017
Published online: 12 October 2017

Vahid Rahmati[1], Knut Kirmse[2], Knut Holthoff[2], Lars Schwabe[3] & Stefan J. Kiebel[1]

During neocortical development, network activity undergoes a dramatic transition from largely synchronized, so-called cluster activity, to a relatively sparse pattern around the time of eye-opening in rodents. Biophysical mechanisms underlying this sparsification phenomenon remain poorly understood. Here, we present a dynamic systems modeling study of a developing neural network that provides the first mechanistic insights into sparsification. We find that the rest state of immature networks is strongly affected by the dynamics of a transient, unstable state hidden in their firing activities, allowing these networks to either be silent or generate large cluster activity. We address how, and which, specific developmental changes in neuronal and synaptic parameters drive sparsification. We also reveal how these changes refine the information processing capabilities of an *in vivo* developing network, mainly by showing a developmental reduction in the instability of network's firing activity, an effective availability of inhibition-stabilized states, and an emergence of spontaneous attractors and state transition mechanisms. Furthermore, we demonstrate the key role of GABAergic transmission and depressing glutamatergic synapses in governing the spatiotemporal evolution of cluster activity. These results, by providing a strong link between experimental observations and model behavior, suggest how adult sparse coding networks may emerge developmentally.

The proper development of neural networks is strongly activity-dependent[1]. A common feature of the immature cortex is the generation of synchronized network activity in which discrete events are separated by relatively long quiescent periods[2,3]. During development, this so-called cluster activity transitions to a sparse firing pattern as typically observed in adult networks[4]. Sparse firing is supposed to represent an efficient coding regime for processing and storing information in the mature cortex during adulthood[5,6]. The developmental transition from dense to sparse coding has been observed in all cortical areas examined to date[2,3,7] and, in addition, in human cortex[8]. Moreover, since, unlike adult networks, eliciting large cluster activity is a ubiquitous feature of many immature neural structures[1,9], sparsification is believed to be a universal phenomenon of neural network maturation. Although sparsification is thought to represent an essential aspect of cortical development, the mechanisms underlying this process are currently not understood. Data obtained from rodents led to the conclusion that the process of sparsification is largely, though not entirely[3], independent of sensory inputs[2,7]. Strikingly, the time period of development during which sparsification occurs coincides with major changes in both intrinsic neuronal and synaptic properties. These include, for example, a profound decline in membrane resistance[2,10], a steep increase in the number/density of both GABAergic and glutamatergic synapses[11,12], an acceleration of the kinetics of postsynaptic currents[12] as well as pronounced changes in short-term synaptic plasticity[10,12].

Here, we describe a computational modelling approach based on experimentally measured trajectories of intrinsic neuronal and synaptic parameters in order to provide mechanistic insights into the generation of cluster activity and the transition from dense to sparse coding during development. To this end, we use the well-established extended Wilson-Cowan-type model accounting for mechanisms of short-term synaptic plasticity[13]. Despite the lack of well-established immature neuron models, as still many unspecified parameters need to be measured first, using this biophysically interpretable mean-field model enables the study of developing networks based on the average effects of these parameters at a network level. By combining this model with

[1]Department of Psychology, Technische Universität Dresden, 01187, Dresden, Germany. [2]Hans-Berger Department of Neurology, University Hospital Jena, 07747, Jena, Germany. [3]Department of Computer Science and Electrical Engineering, University of Rostock, 18059, Rostock, Germany. Correspondence and requests for materials should be addressed to V.R. (email: vahid.rahmati@tu-dresden.de)

experimentally reported trajectories of neurobiologically plausible parameters during postnatal development, we found that we can emulate typically observed *in vivo* features of developing network function.

By using the mathematical tool of stability analysis, we derive three key results which help to better understand the sparsification process. Firstly, in the model we find that at early postnatal days, while the network is resting at its low-activity spontaneous state, an unstable state is built up in its firing activities. This is important, because we find that this transient, hidden unstable state is key to the emergence of large postnatal cluster activity. Using the model, we show how sparsification is driven developmentally, and how during this process the network's information processing is refined. Secondly, we address the open question what mechanisms govern the spatiotemporal evolution of postnatal cluster activity. Thirdly, we quantify the effect of different maturational processes on sparsification. Together, this study provides the first mechanistic insights into the *in vivo* biophysical mechanisms underlying sparsification, and the implications of this process for the refinement of information processing.

Results

To study developmental changes in postnatal neuronal activity, we used simulations of a spatially localized recurrent neural network with short-term synaptic plasticity (STP-RNN)[13], where STP renders synaptic efficacies dynamic over time[14,15]; see Methods. This network is a mean-field Wilson-Cowan-type model of one excitatory (E) and one inhibitory (I) neuronal population with recurrent dynamic synaptic connections (Fig. 1a). This model has the advantage of being biophysically interpretable and mathematically accessible. The activity rates (E_t and I_t) can be properly scaled to represent locally the average recorded activities in the populations. Here, we use experimentally reported, postnatal changes in neurobiologically plausible parameters (Table 1) to assess how the network's spontaneous behavior and sensory processing properties are refined toward the postnatal onset of sensory transduction. To study the developmental states of visual cortical networks from before to after eye-opening, we selected four postnatal days (P) for modelling: P3 (period of physiological blindness), P10 (a few days before eye-opening), P14 (the day after eye-opening) and P20 (a few days after eye-opening)[3]. During this period, immature networks not only undergo the sparsification process but also a dramatic development in intrinsic neuronal and STP properties[10,12]; see Table 1 and Supplementary Methods. To derive the results, we used system dynamics methods described in the Methods section (see also Supplementary Methods). For quick reference, all important technical terms are explained in Table 2.

Transient unstable state hidden in firing activities. We first address what mechanisms may underlie the emergence of cluster activity in immature networks, by analyzing model behavior at P3 as a representative early postnatal stage.

Previous experimental[16,17] and modeling studies[18,19] usually considered adult networks to be bi- or multi-stable where, e.g., spontaneous (stimulus-absent) network activity can transition between two stable activity states: A relatively quiet activity state, and a higher activity state. For early postnatal stages, our stability analysis and simulations indicate that the proposed developing network model is actually mono-stable whose only stable state is a quiescent, spontaneous state (Fig. 1b). To demonstrate this, we plotted in Fig. 1b the so-called phase plane of network dynamics in terms of the average activity in the E- and I-populations (E_t-I_t-plane; Table 2). Figure 1b shows that the network's fixed point (FP; Table 2) is located at $E_t = I_t = 0$ which is essentially a stable activity state of the network (see Supplementary Methods). In the following, we will call this specific FP the rest state of the network. This analysis result fits well with experimental findings of near-zero hertz spontaneous activity of immature populations[3,20], and the absence of spontaneous network's persistent activity states mainly during periods of physiological blindness[7,21].

How can a quiescent, immature, mono-stable network generate large cluster activity? By analyzing network perturbations, we found strikingly that while a P3 network model was relaxed at its stable rest state, threshold-crossing perturbations of E-population were amplified profoundly (Fig. 1c, Supplementary Fig. 1c). This amplification resulted in population spikes (PSs, Table 2), which, in the model, we assume is the analogue to experimentally observed cluster activity. Note that this perturbation can be due to, e.g., a single-shock electrical stimulation[22], the onset of a longer-lasting external input (Supplementary Fig. 2c), or a random input driven by spontaneous retinal waves or the thalamus[3,20].

While previous studies showed the underlying mechanism of PSs generation mainly in adult bi-stable network models[18,19], here we sought to address this mechanism in an immature mono-stable network (Fig. 2). As the initial phase of PSs is known to be governed by the network's fast (i.e. firing activity) dynamics[18], we re-plotted the E_t-I_t-plane after freezing the network's slow (i.e. STP) dynamics at the rest state (Fig. 2d); thus, it is turned to a Static-RNN (Table 2) with frozen synaptic efficacies (Frozen STP-RNN). Surprisingly, we found that in addition to the stable rest state, there is an unstable FP hidden in the network's fast dynamics (i.e. in the respective Frozen STP-RNN, Fig. 2e), which does not exist in the (non-frozen) STP-RNN (Fig. 1b). This unstable FP (black dot, Fig. 2e), which is located close to the rest state, can confine the attraction domain (grey region, Table 2) of the stable rest state in the E_t-I_t-plane of the corresponding Frozen STP-RNN (Fig. 2d); but, clearly, not in the E_t-I_t-plane of the STP-RNN itself (Fig. 2c). We call the outer border of this domain in Fig. 2d (before perturbation) the amplification-threshold. Almost exactly the same border exists for activity-perturbation domains of the STP-RNN (Fig. 2c). Cluster activity is initiated by an activity perturbation exceeding this threshold, where the activity will be moved far from the rest state in both corresponding networks with frozen (Frozen STP-RNN) or dynamic (STP-RNN) synapses. Strikingly, when freezing synaptic efficacies at different times during a cluster activity (Fig. 2a), we can see that this unstable FP disappears roughly after the peak of cluster activity (Fig. 2e), thereby allowing network activity to converge back to its stable rest state in the STP-RNN (Fig. 2a). This disappearance is mainly because of the weakening of the excitatory synapses at high activity rates (Fig. 2b); these synapses provide positive feedback to the network. Importantly, as it can be seen in Fig. 2e (panel IV), while the

www.nature.com/scientificreports/

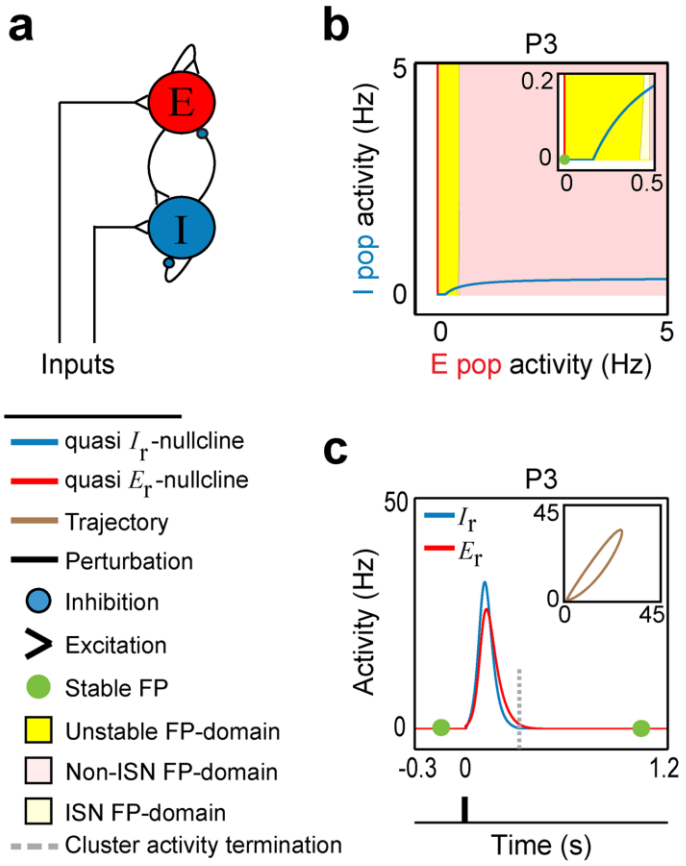

Figure 1. The stationary and cluster activity properties of a STP-RNN at P3. (**a**) Graph representing the spatially localized network of one excitatory, E, and one inhibitory, I, neuronal populations that are recurrently connected (RNN), and can receive inputs. (**b**) The E_r-I_r-plane of the RNN with dynamic synapses (STP-RNN) at postnatal day P3 (early period of physiological blindness). The colored regions show the fixed point (FP) domains of three possible operating regimes: unstable dynamics, inhibition-stabilized network (ISN), and Non-ISN; see Table 2 for details. (Inset) Zoom-in of the phase plane at lower activity ranges, overlaid by the FP of the STP-RNN. The ISN FP-domain is barely visible. The rest state and the vertical branch of the quasi E_r nullcline at $E_r = 0$ belong to the Non-ISN FP-domain. The horizontal branch of the quasi I_r- nullcline at $I_r = 0$, forming the bottom-border of the ISN (barely visible) and unstable regimes, belong to the unstable FP-domain (see Supplementary Methods). Only the non-negative branches of the quasi E_r- and I_r- nullclines (i.e. in $\geq$0 Hz ranges) were displayed (e.g. see Supplementary Fig. 4, for the negative branches of the quasi nullclines). (**c**) Cluster activity triggered by an impulse perturbation (e_E^{per}) to the E-population at time $t = 0$ when the network was relaxed at the stable rest state. (Inset) Trajectories of cluster activity in E_r-I_r-plane. Simulations were performed for $e_E^{per} = e_E(t = 0) = 30$ Hz. For all simulations, parameter values can be found in Table 1.

network is again at the origin after cluster activity, sufficient recovery time is required for the re-emergence of the unstable FP.

Our analyses further show that the experimentally observed variability in size (i.e. the number of network neurons recruited by cluster activity) and duration of spontaneous cluster activities at each postnatal day[2,3] is effectively governed by the relatively long recovery time of immature excitatory synapses (Supplementary Fig. 1). In addition, in our model, cluster activity was generated only if the perturbation strength was sufficiently large (Supplementary Fig. 1c and d) and was able to push network activity beyond the amplification-threshold (Fig. 2c and d). This is consistent with experimental reports of immature networks[7,23], and may underlie a relatively all-or-none characteristic of postnatal cluster activity.

	P3	P10	P14	P20
τ_E	0.045	0.030	0.020	0.010
τ_I	0.0225	0.0150	0.010	0.005
$\tau_{r\,E}$	5.5	3	0.7	0.5
$\tau_{r\,I}$	5	2.5	0.4	0.2
τ_{fE}	0.8	0.4	0.1	0.05
τ_{fI}	0.8	0.4	0.1	0.05
U_E	0.9	0.8	0.65	0.55
U_I	0.9	0.8	0.55	0.4
J_E	3.7	7	6.3	5.5
J_I	0.1	3	4	4.5
θ_E	0.3	0.47	0.7	1
θ_I	0.3	0.5	1.7	2

Table 1. Parameter values used in the developing STP-RNN model. This table lists the values of the developing STP-RNN parameters at postnatal days P3 (early period of physiological blindness), P10 (a few days before eye-opening), P14 (the day after eye-opening) and P20 (a few days after eye-opening). The time constants are in units of [s]. All parameters are consistent across the figures, unless stated otherwise. τ_i is an approximation to the decay time constant of postsynaptic responses, τ_{r_i} is the synaptic recovery time constant of depression, τ_{f_i} is the synaptic facilitation time constant, U_i is the release probability, J_i is the absolute synaptic efficacy, and θ_i is the population activity threshold (in units of [Hz]). The quantities express the mean parameter values for excitatory (i = E) and inhibitory (i = I) populations. Although not listed here, for simplicity, we fixed G_i (the linear input-output gain above θ_i) at 1, while considering its developmental changes in values of J_i. See "Parameterization of postnatal developing networks" section in Supplementary Methods for the list of experimental papers that we used to determine these developmental changes in parameter values.

The route towards sensory processing. The sparsification of activity patterns sets in around eye-opening[3,7]. We now use our model at the stages P10 to P20 to address the question what refinements of the developing network enable sparsification.

Firstly, similarly as for P3, at all later stages up to P20 in the model we found that for a developing network relaxed at its stable rest state (Fig. 3a), again an unstable FP is hidden in the network's fast (i.e. firing activity) dynamics (Fig. 3b). Consequently, a threshold-crossing perturbation of the E-population at rest state led to cluster activity (Fig. 3c). In addition, our analysis revealed that the amplification-threshold tends to move toward higher E-activity rates, from P3 to P20 (Fig. 3b, Supplementary Fig. 3). This result suggests that a stronger input may be required to trigger (large) cluster activities at late development stages.

Experimental *in vivo* findings show that the cluster activity size starts to drop dramatically around the end of the second postnatal week[2,3]. Here, we consider this developmental decrease in cluster activity size as an indicator for the developmental transitioning from dense to sparse coding (sparsification process); similarly to experimental studies[2,3]. In our model, we approximate the cluster activity size by a measure of the average activity of both E- and I-populations (PS_{net}^{amp}; see Table 2 and Methods). Using this measure, we observed, similarly as in experiments, that cluster activity size undergoes developmental reduction between P10 to P20 (Fig. 3c and d, see also Supplementary Fig. 2c): It was relatively large at P10 ($PS_{net}^{amp} \approx 85$), but starkly reduced after eye-opening (P14; $PS_{net}^{amp} \approx 30$), followed by some further reduction to P20 ($PS_{net}^{amp} \approx 15$).

Secondly, the results also show that immature networks probably lack any spontaneous, non-quiescent stable FP (i.e. a spontaneous attractor or persistent activity state) up to a few days prior to eye-opening. In Fig. 3a this is indicated by the existence of only one green dot at P3 and P10. However, after eye-opening, new spontaneous FPs with higher activity rates than the rest state emerged (note the non-origin FPs at P14 and P20 in Fig. 3a). This is compatible with experimental data showing the existence of spontaneous persistent cortical activity for stages mostly after the second postnatal week[3,21,24] and their absence during early development[7,21]. In our model, in the absence of a stimulus, these FPs emerge mainly because of the developmental increase and decrease in background activity[2,3,7] and membrane resistance[2,10], respectively. Their combined effects determine the increase in population activity thresholds θ_E and θ_I (see also Supplementary Fig. 4). While in the model the network's FP domains (FP-domains; Table 2) are not affected by these thresholds (see "Characterization of operating regimes" section in Supplementary Methods and also Supplementary equation (17)), the developmental reduction in the network instability (yellow regions, Fig. 3a) allows for these FPs to be stable. This means that attractors start emerging, under a wide range of E-activity; note the non-origin green dots at P14 and P20 in Fig. 3a.

Thirdly, the emergence of spontaneous attractors not only turns the developing mono-stable network (at P3 and P10) into a bi-stable (at P14 and P20) network (Fig. 3a), but also has a striking effect on the dynamical trajectory of cluster activity. That is, in the model, we found a fundamental difference between spontaneous postnatal cluster activities and those in more mature networks (Fig. 3c): before eye-opening (P3 and P10), the cluster activity is of the so-called mono-stable type (see Supplementary Methods), while after eye-opening the cluster activity can be also of the bi-stable type. The difference is that a mono-stable cluster activity (P3 and P10 in Fig. 3c) is initiated and terminated at the stable rest state, while a so-called bi-stable cluster activity is initiated at the stable rest state but converges to a spontaneous attractor (P14 and P20 in Fig. 3c, green dots). This difference may be

Abbreviation	Description
RNN	Recurrent neural network (RNN) of one E-I pair of synaptically coupled populations*.
STP-RNN & Static-RNN	A RNN composed of synaptic connections with short-term plasticity (STP-RNN) which renders the synaptic efficacies dynamic over time. The RNN with constant efficacies is a Static-RNN†.
Frozen STP-RNN	A STP-RNN with the synaptic efficacies frozen e.g. at the FP; thus, a Static-RNN-type model‡.
E_t-I_t-plane	A 2D phase plane of E- and I-population activity rates (I_t vs. E_t)‡.
FP	A fixed point (FP) is the steady state of a network, and is determined as the intersection of (quasi) E_t- and I_t- nullclines in the E_t-I_t-plane‡.
Spontaneous activity	Network activity in the absence of stimulus (or sensory input)*.
Attractor	A non-quiescent stable FP (in this paper); also known as memory or persistent activity state.
Attraction domain	For a stable FP (in this paper), a region in phase plane comprising all initial conditions that lead to that FP.
Amplification-threshold	The outer border of the attraction domain of the rest state in the Frozen STP-RNN, beyond which network perturbations undergo an overall continuous growing (in the Frozen STP-RNN) or will effectively trigger cluster activity (in the STP-RNN).
Nullcline	For example, an excitatory nullcline is a set of points (a curve) in E_t-I_t-plane for which $dE_t/dt = 0$‡.
FP-domain	For example, an unstable FP-domain is a domain of all potential FPs in the E_t-I_t-plane, at which the network will be unstable¶.
AOD	Area of domain (AOD); for example, AOD_{Unstable} is the area of the unstable FP-domain¶.
ISN	Inhibition-stabilized network (vs. Non-ISN) which requires sufficiently strong, dynamic inhibitory feedback to preserve its overall stability.§
$AOD_{\text{ISN/Unstable}}$	$=AOD_{\text{ISN}}/AOD_{\text{Unstable}}$; this ratio is used to measure the relative area of the ISN FP-domain vs. unstable FP-domain¶.
PS	The near coincident firing of many neurons is often referred to as population spike (PS)#.
Cluster activity	Network spike (PS_{net}), which involves both E- and I-populations; i.e. both PS_E and PS_I#.
ps_{net}^{amp}	The scaled amplitude of PS_{net}, which provides a qualitative approximation to the cluster activity size#.

Table 2. Overview of technical terms and analysis metrics. This table lists the descriptions for abbreviations and definitions which we used in our study. The sections in Supplementary Methods providing detailed descriptions: *Model description, †STP-RNN, §Frozen STP-RNN, ‡Computation of 2D phase planes, ¶Operational FP-domains, §Characterization of operating regimes, and #Population spike.

interpreted as a first expression of information processing where the newly emerged attractors, which a bi-stable cluster activity converges to, can be seen as representative states that are the basis of perception. In the model, the time required for an effective transition to the attractor, and thus an effective representation of perceptual stimuli, is probably equal to the duration of cluster activity (see dashed grey lines, Fig. 3c): ~240 ms at P14 and ~180 ms at P20; these transition times are consistent with experimental observations at these stages[17,24].

Moreover, our simulations showed that the spatiotemporal characteristics (i.e. size and duration) of mono-stable cluster activities are in general considerably more robust to interfering perturbations (P3 and P10, Supplementary Fig. 5), as compared to the bi-stable ones (P14 and P20, Supplementary Fig. 5). This suggests that the trajectories underlying mono-stable cluster activities (P3 and P10) can be seen as signals with high signal-to-noise ratio, which may act as a reliable neuronal communication mechanism in neonatal networks. The decreased robustness of bi-stable cluster activities after eye-opening (P14 and P20) can in principle augment the network's information processing capability by making it more flexible in responding to sensory input.

In addition, we found that at the new spontaneous attractors (non-origin green dots; Fig. 3a) the network operates as a so-called inhibition-stabilized network (ISN, light-yellow regions, see also Table 2)[25,26]. An ISN regime is thought to allow the cortex to process complex computations[27], and some experimental evidence indicates that adult cortical networks operate as ISNs[25,28]. Our results show that the ISN regime becomes effectively accessible after eye-opening, as the unstable FP-domain, which is confined to low E-activity ranges, is developmentally substituted by an ISN FP-domain. This indicates a developmental increase in the ratio of areas of the ISN (AOD_{ISN}) and unstable FP-domains (AOD_{Unstable}), which we quantified by $AOD_{\text{ISN/Unstable}}$ (Table 2) in Fig. 3e. In practice, this means that in parallel to the strengthening of the sensory inputs after eye-opening, a larger set of potential stimulus-evoked ISN attractors will be accessible for the network, presumably to perform complex sensory computations.

Overall in our model, the process of sparsification is translated not only to a potent reduction of postnatal network instability but also to a potential emergence of new attractors and information processing capabilities.

Spatiotemporal evolution of postnatal cluster activity. What mechanisms govern the spatiotemporal evolution (i.e., size and duration) of cluster activity during development *in vivo*? We addressed this question by analyzing how a postnatal cluster activity, once on a trajectory away from the rest state, is brought back to either the rest state or another FP with an activity level higher than the rest state.

In our model, there are two important factors: (i) the inhibitory transmission, which is believed to play a critical role in the stabilization of adult networks[25,28], and (ii) STP, which can dynamically control the gain of neuronal responses[14] and acts strongly depressing in immature networks[10,12].

Firstly, we found that cluster activity initiated at the rest state can still converge back to this state even when blocking GABAergic receptors, at all stages from P3 to P20 (Fig. 4a). This finding suggests that inhibitory

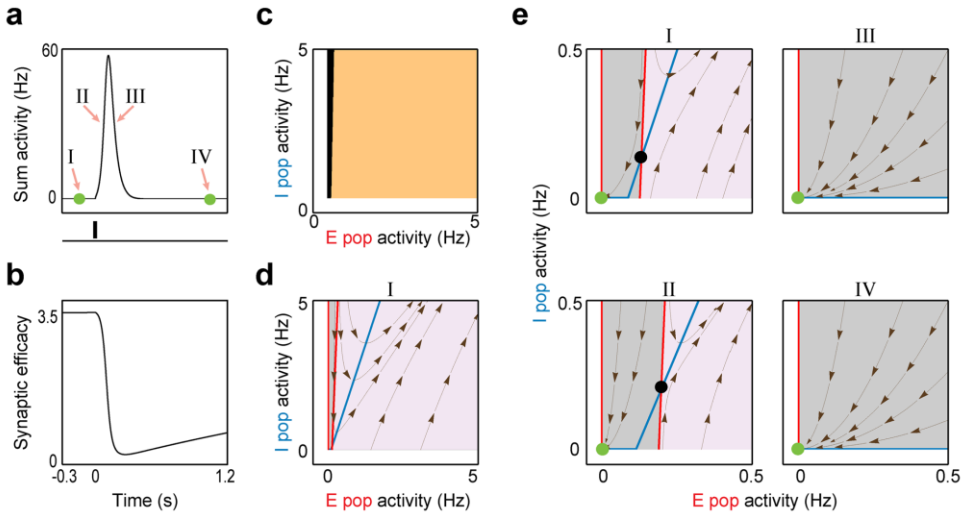

Figure 2. The transient unstable state hidden in fast (i.e. firing activity) dynamics of a STP-RNN at P3. (**a**) The same cluster activity as in Fig. 1c, but shown in terms of the sum activity $A_{\text{sum}} = E_r + I_r$. (**b**) The time-evolution of synaptic efficacy of the recurrent excitatory connection $J_E\, x_E\, u_E$, during the network activity shown in (**a**). (**c**) Activity-perturbation domains of STP-RNN. For the network relaxed at the rest state, setting the initial condition of the network activity at different E-and I-activity values revealed two different types of domains; amplification domain (cream-colored region): After perturbation, the sum activity was effectively amplified and cluster activity emerged; Non-amplification domain (black region): After perturbation, the sum activity monotonically decayed back to the rest state. Note, for the P3 network (mono-stable), both these domains are attraction domains of the rest state in the STP-RNN. (**d**) The E_r-I_r-plane and the E_r- (red) and I_r-nullclines (blue) of the STP-RNN with frozen synaptic efficacies (i.e. Frozen STP-RNN) at the rest state (see the time I in (**a**); $t = -150$ ms, relative to onset of input). Grey region: The attraction domain of the stable rest state in the Frozen STP-RNN. Purple region: The activities initiated here undergo an overall continuous growing (non-attraction domain). We call the border between these two regions the amplification-threshold. This border is approximately the same as the border between the two domains in (**c**). (**e**) Disappearance of the hidden unstable state during cluster activity. (I): Zoom-in of (**d**) at lower activity rates, overlaid by the FPs of the corresponding Frozen-RNN. (II-IV): Same as (I), but for synaptic efficacies frozen at different sample times (see (**a**)): (II): $t = 75$ ms, (III): $t = 175$ ms, (IV): $t = 1000$ ms. Black dots show the unstable FPs. Dark-brown streamlines show, at each point, the local direction of sample trajectories in the corresponding Frozen-RNN.

processing may not be necessary for stability in the developing network with depressing excitatory synapses. However, blockage of GABAergic receptors yielded an increase in cluster activity size (Fig. 4a and c), consistent with *in vivo* reports[20,29]. This blockage effect on cluster activity size became more pronounced during the course of development (Fig. 4c), in spite of the developmental reduction in the network instability (e.g. see $AOD_{\text{ISN/Unstable}}$ in Fig. 3e). This finding may underlie a developmental enhancement of an effective contribution of inhibitory transmission to network activity (see also Supplementary Fig. 2d showing the ability of inhibitory inputs to turn off activity at the attractor[22], after eye-opening). In addition, we found that the blockage of GABAergic receptors shortened the cluster activity duration, for example, from approximately 330 to 320 ms at P3 (Fig. 4a and b) and from approximately 265 to 210 ms at P10 (Fig. 4a). The range of these cluster activity durations in our model is compatible with previous experimental reports[7,30]. Moreover, we found that this blockage effect on cluster activity duration increased from P3 to P20 (Fig. 4d).

Secondly, in contrast to GABAergic transmission, we found that at P3 the simulated removal of the STP effect led to run-away excitation (Fig. 4e). After freezing the synaptic efficacies (see Supplementary Methods) at the stable rest state, a threshold-crossing perturbation of the E-population (similarly as in Fig. 1c) caused a seizure-like surge of network activity (Fig. 4e). Importantly, this means that the rest state in the corresponding Frozen STP-RNN is a locally, but not globally, stable FP (see Methods). Similar results were observed for P10 to P20 (data not shown). Accordingly, we conclude that the strongly depressing immature STP, but not inhibitory synaptic transmission, guarantees the stabilization of postnatal cluster activities during the course of development. This finding also holds, when GABAergic transmission is considered as excitatory at the network level during the first postnatal week (see Supplementary Methods and Supplementary Fig. 6b). Under this assumption, blocking GABAergic receptors led to a decrease in cluster activity size, which is not compatible with *in vivo* data[20,29]. Therefore, our modeling results (Fig. 4b) are in agreement with recent *in vivo* findings that while GABA

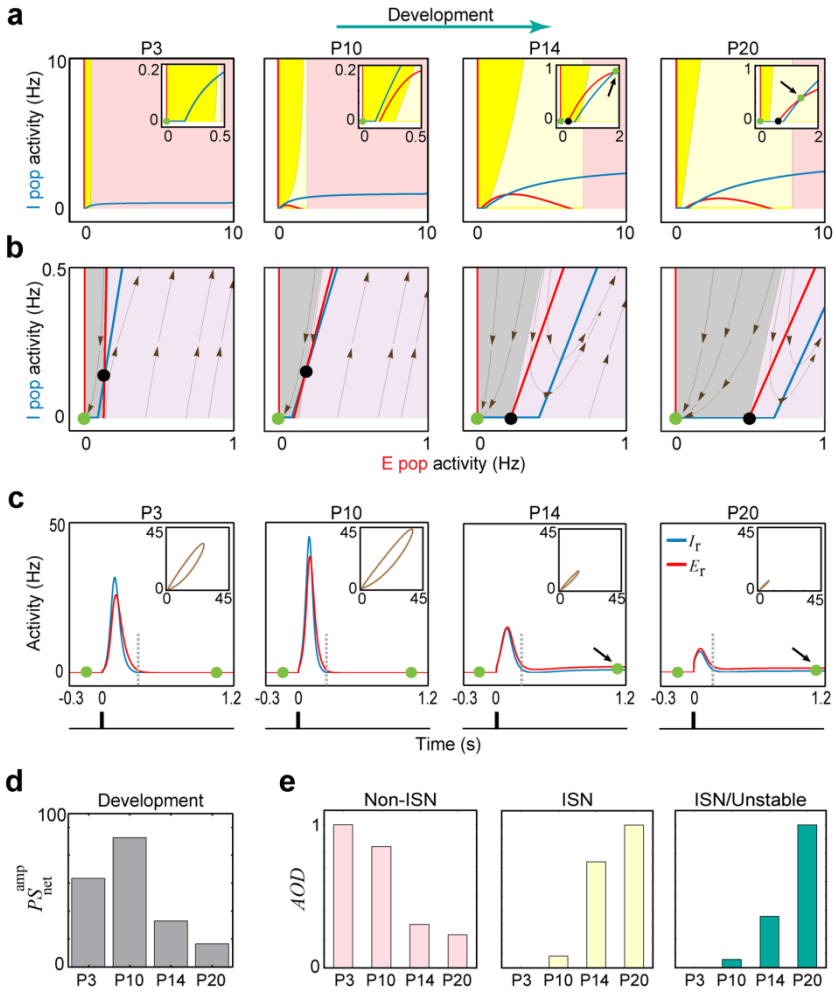

Figure 3. Sparsification process in developing cortex. (**a**) Postnatal changes of the network's stationary firing dynamics. The same format is used as in Fig. 1b; unstable dynamics (yellow region), ISN (light-yellow region), and Non-ISN (pink region). (**b**) The existence of a hidden unstable state (black dot) in the firing activity of developing networks. The same format is used as in Fig. 2e, panel I. The networks were frozen at the rest state ($t = -150$ ms). (**c**) Postnatal changes of the network's transient firing dynamics where cluster activity was triggered by an impulse perturbation. The same format is used as in Fig. 1c. P3: early period of physiological blindness, P10: a few days before eye-opening, P14: the day after eye-opening, and P20: a few days after eye-opening. Green dots represent the stable FPs. (**d**) Developmental changes in the size of cluster activities, estimated qualitatively by PS_{net}^{amp}. (**e**) Developmental changes in the area of the FP-domain (AOD) of Non-ISN and ISN operating regimes, and the ratio $AOD_{ISN/Unstable}$ of areas of ISN and unstable FP-domains. The developmental increase in $AOD_{ISN/Unstable}$ indicates that the unstable FP-domain was effectively decreased, and replaced by the ISN FP-domain. For each panel, the values were normalized to the maximum value during all four stages. At each of these stages, the AOD s were computed based on the square E_r-I_r-plane with the lower-left corner located at the rest state (origin) and the upper-right corner (i.e. $[E_r^{max}, I_r^{max}]$) at [10,10] Hz. Moreover, the developmental decrease in $AOD_{Non-ISN}$ just means that the E-activity rate after which the Non-ISN FP-domain starts in the E_r-I_r-plane, was shifted to higher levels. See Table 2 for details about technical terms.

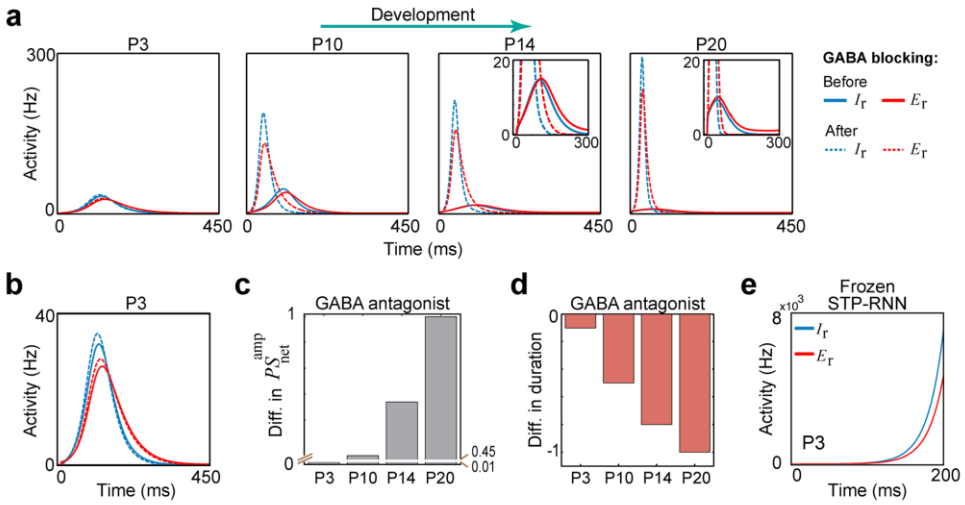

Figure 4. Contribution of GABAergic transmission to cluster activity during course of development. (**a**) The effect of blocking GABAergic receptors (i.e. $J_I = 0$) on cluster activities, during development. The plots show that even with this blockage, cluster activity that emerges from the rest state can still converge back to this state. Solid lines: cluster activity before the blockage, Dashed lines: cluster activity after the blockage. (**b**) Zoom-in of P3 in (**a**) at lower activity rates. Note the increase in E- and I-activities after the blockage. (**c**) Normalized differences in cluster activity size before and after the blockage (*after* minus *before*), at the four developmental stages. The values were normalized to the maximum difference observed throughout P3 to P20. (**d**) Same as (**c**), but for cluster activity duration. (**e**) The effect of freezing the synaptic efficacies at the stable rest state, at P3. A threshold-crossing perturbation (see light-purple region in Fig. 2d) leads to run away activities; note the scale of the y-axis.

acts as a mainly depolarizing transmitter during the first postnatal week, it exerts an inhibitory effect on the underlying network activity in the immature cortex and hippocampus[20,31].

Moreover, cluster activity was abolished by simulated blockage of glutamatergic receptors (data not shown), consistent with experimental *in vivo* data[20,29]. This is because the main source of the network instability in our model is determined by glutamatergic synapses which provide positive feedback to the network. Therefore, blocking glutamatergic receptors removed all unstable FPs as well as the attractors in Fig. 3a and forced spontaneous network activity to the rest state (as observed experimentally[17,22]), and removed the unstable FP hidden in the network's fast dynamics in Fig. 3b, throughout P3 to P20 (data not shown). In addition, note that the GABAergic transmission can play an important modulatory effect on this instability (see Supplementary Methods), where an increase in the efficacies of inhibitory synapses can effectively attenuate the instability (not shown). This implies that relatively weak GABAergic inhibition (Table 1) is permissive for the generation of the unstable states (e.g. see Fig. 3a and b) in developing networks; note that in our model these synapses strengthen during development (Table 1).

In sum, we found that strongly depressing excitatory synapses have a key role in the termination of postnatal cluster activities, whereas GABAergic transmission mainly regulates their spatiotemporal evolution.

Key maturational processes mediating sparsification. The most influential, maturational processes mediating sparsification are still not clearly understood[2,3]. By using our modelling approach, we mechanistically quantified the impact of different network parameters on the emergence of sparse coding.

To do this, we replaced single parameters or parameter combinations of the P10 network model by their respective values at P20 and measured to what extent this modification can account for the normal decrease in PS_{net}^{amp} and normal increase in $AOD_{ISN/Unstable}$, when transitioning from P10 to P20. To quantify effects we computed $ratio_{PS}$ and $ratio_{AOD}$ as the ratios of the modification-induced changes in PS_{net}^{amp} and $AOD_{ISN/Unstable}$, relative to their respective normal developmental changes during this period (Fig. 5). We found that only three parameters caused a substantial decrease in PS_{net}^{amp} (Fig. 5a): the two absolute synaptic efficacies (J_E and J_I) caused the largest decrease close to that in the normal transition and, to a minor degree, the excitatory release probability U_E. Strikingly, for the excitatory synaptic time constant (τ_E) the modification led to an increase in PS_{net}^{amp}, i.e. when this parameter is changed on its own, it tended to reverse sparsification (see also Supplementary Figs 6c and 7). We obtained qualitatively similar conclusions when analyzing the effect of replacing single parameters or parameter combinations of the P20 network model by their values at P10 (Supplementary Fig. 8a). When testing for changes

in $AOD_{ISN/Unstable}$, we found that the inhibitory synaptic depression time constant τ_{I_1} had the strongest contribution to the normal transition from P10 to P20, whereas all other single parameter substitutions had relatively weak effects (Fig. 5b). Note that the change in τ_{I_1} appears to be a necessary but not a sufficient condition for the normal transition from P10 to P20, as substituting J_E and J_I in the P20 model by their respective P10 values virtually abolished the developmental change in $AOD_{ISN/Unstable}$ (Supplementary Fig. 8b). Figure 5 further shows that the modification effect of the population activity thresholds (θ_E and θ_I) was virtually negligible for $ratio_{PS}$ and zero for $ratio_{AOD}$. However, as shown above, their maturation plays an important role for the emergence of spontaneous attractors (see also Supplementary Fig. 4).

Discussion

We modelled the *in vivo* activity of a developing cortical network during the first postnatal month by combining an extended Wilson-Cowan model with experimentally reported trajectories of neuronal and synaptic parameters. We revealed mechanistically that a particular combination of a transient, hidden unstable state in firing activities and strong synaptic depression enables an immature network to generate large cluster activity while otherwise being mostly silent. We further found that the normal developmental transition from dense to sparse coding is strongly dependent on an elaborate, parallel refinement of absolute synaptic efficacies, both short-term synaptic plasticity (STP) and intrinsic membrane properties, and background activity. Strikingly, in our model, sparsification translates not only to a reduction of postnatal instability of network activity but also to an effective availability of the inhibition-stabilized network (ISN) regime as well as the emergence of spontaneous attractors, providing a novel mechanistic explanation for how the network's information processing is refined towards eye-opening.

How can immature networks be quiescent for relatively long periods and occasionally generate large cluster activity[3,32]? Surprisingly, we found that while the developing networks (P3 to P20) are operating at their rest state (Fig. 3a), an unstable state is formed in their fast (i.e. firing activity) dynamics (Figs 2e and 3b). This may be a key to this biphasic behavior (Fig. 3c and Supplementary Fig. 2c). In addition, we found that at early stages prior to eye-opening (P3 and P10) immature networks are mono-stable, where the only FP of the network is its stable rest state (Fig. 3a). Accordingly, the underlying mechanism of cluster activity emergence in these networks is in stark contrast to models of cluster activity proposed for adult networks, based on the usual assumption of a bi-stable (or multi-stable) network[18,19]. Our finding about the strong effect of the hidden unstable state (Fig. 3b) during the initial phase of network activity at the rest state (see Figs 2 and 3c) may provide an explanation why neonatal networks, e.g. at P3 and P10, are more susceptible to seizures than mature networks[32,33]. Moreover, the lack of any spontaneous attractor in these networks (Fig. 3a) might also contribute to this susceptibility, since the attractors can, in principle, aid in stabilizing a network's activity.

Sparsification coincides with the peak of GABAergic and glutamatergic synaptogenesis[11,12] and overlaps with a developmental reduction in release probabilities, particularly at glutamatergic synapses[10,12]. Using a computational study, we here revealed how these changes are suited to drive the transition from dense to sparse coding during network maturation (e.g. see Figs 3 and 5). Since sensory deprivation affects the total synapse numbers only modestly[34], our results might also explain previous experimental findings: While sensory experience may have a modulatory effect on sparsification during the first days after eye-opening[3], this process is largely mediated internally, i.e. independent of sensory inputs[2,3,7].

How does the sparsification process prepare *in vivo* developing networks for effective sensory processing? While the answer to this question remains poorly understood by experimental studies, our computational study provides two mechanistic insights: Firstly, we found that Non-ISN and instability may play key roles as the dominating operating regimes prior to eye-opening (Fig. 3a), possibly reflecting an immaturity of inhibitory transmission. That is, our modeling results imply that during stimulation (e.g. in response to long-lasting external inputs) the immature networks will operate under a Non-ISN regime, rather than an ISN regime (P3 and P10; Supplementary Fig. 2b), due to the lack of an effective availability of the ISN regime during early development (P3 and P10; Fig. 3a). The Non-ISN regime will enable the immature networks to maintain their stability without requiring inhibitory transmission effects (see Methods). For adult networks, however, some experimental evidence indicates that cortical networks operate as ISNs[25,28]. Strikingly, in the model, during sparsification, the unstable FP-domain is effectively replaced by that of an ISN regime (Fig. 3a and e). This may enable cortical networks to process complex sensory computations[27] in parallel to the developmental strengthening of sensory inputs.

Secondly, we found that spontaneous attractors start emerging around eye-opening, which, in our model, is mainly due to the combined effect of developmental increase in background activity[2,3,7] and the developmental decrease in membrane resistance[2,10]. In general, attractors can represent the solution to a specific neural computation[35]. They are also thought to be the substrate of, and used to model, e.g., the working memory[36], eye position stability[37], and orientation selectivity[38]. Besides, in our developing model, the attractor emergence phenomenon can also underlie three developmental mechanisms. First, it provides the basis for transitioning between FPs (here, via bi-stable cluster activity at P14 and P20; Fig. 3c) and may be thought of as an early step towards representation of perceptual stimuli. Second, it enables inhibitory transmission to contribute effectively more to network activity, e.g. through providing a sufficiently strong balancing of the intrinsic instability of the E-activity under an ISN regime[26,27] (P14 and P20; Fig. 3c), or by becoming amenable to terminate activity at the attractor[22] (Supplementary Fig. 2d). This may be important for a presumably more effective processing of sensory inputs. Third, this phenomenon may also initiate the effective interaction of spontaneous activity with sensory cortical responses, as observed experimentally[17].

Evidence from *in vitro* studies suggests that GABA depolarizes neonatal neurons, e.g. in rodents during the first postnatal week[20,32]. However, the effect of GABA at the network level is still an open question. While most of

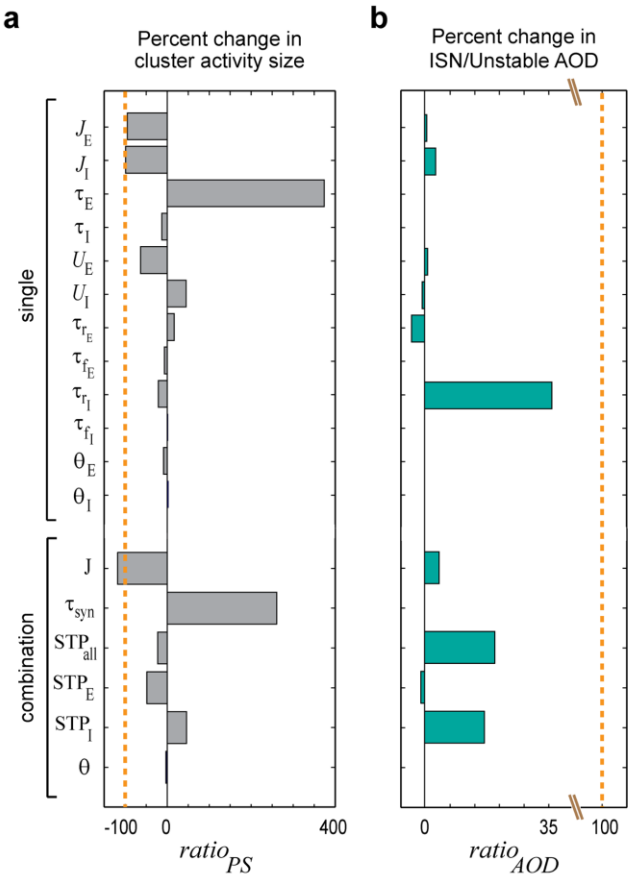

Figure 5. Impact of specific maturational processes on the sparsification process. We measured the change in network behavior when, virtually, we only mature a single parameter or small sets of similar parameters from P10 to P20. This enables us to indicate key parameters required for sparsification. (**a**) The plotted values of $ratio_{PS}$ measure the modification-induced changes in PS_{net}^{amp}, i.e. the size of simulated cluster activity, relative to the decrease when transitioning from P10 to P20. The dashed orange line at $ratio_{PS} = -100$ % indicates the normal amount of decrease in PS_{net}^{amp}, as expected when transitioning from P10 to P20. (**b**) The plotted values of $ratio_{AOD}$ measure the modification-induced change in $AOD_{ISN\ /\ Unstable}$, i.e. the ratio of areas of ISN and unstable FP-domains, relative to the increase when transitioning from P10 to P20. The dashed orange line at $ratio_{AOD} = +100$ % indicates the normal amount of increase in $AOD_{ISN/Unstable}$, as expected when transitioning from P10 to P20. See Methods for the formulas of $ratio_{PS}$ and $ratio_{AOD}$. For computing $AOD_{ISN/Unstable}$, we considered the E_r-I_r-plane plots with $[E_r^{max}, I_r^{max}] = [10,10]$ Hz. Parameters combinations are $J = \{J_E, J_I\}$, $\tau_{syn} = \{\tau_E, \tau_I\}$, $STP_{all} = \{STP_E, STP_I\}$, $STP_E = \{U_E, \tau_{r_E}, \tau_{f_E}\}$, $STP_I = \{U_I, \tau_{r_I}, \tau_{f_I}\}$, $\theta = \{\theta_E, \theta_I\}$.

the previous *in vitro* studies reported that GABA is excitatory (or both excitatory and inhibitory) at the network level[32], recent *in vivo* studies harnessing new experimental techniques found that GABA inhibits intact neonatal networks in neocortex and hippocampus[20,29,31]. In particular, GABAergic transmission was shown to limit the spatial extent of cluster activity[20]. In our model, we tested these two hypotheses by blocking the GABAergic receptors in two P3 networks with either excitatory (Supplementary Fig. 6b) or inhibitory GABAergic transmission (Fig. 4b). This simulated manipulation led to an increase in the cluster activity size only when GABAergic transmission was inhibitory at the network level. Therefore, our results support the recent *in vivo* findings[31,33]. Importantly, this finding implies that even when GABA depolarizes immature neurons, GABA still can attenuate the instability effect on network activity, thereby restricting cluster activity size.

To our knowledge, there are only few previous modelling studies covering this developmental period (e.g. see refs[39,40]), where the authors' main focus was on the potential mechanism of the cluster activity generation under

in vitro condition. These studies were focused on a single postnatal stage and this stage was mostly restricted to the first postnatal week, like P5. Moreover, these authors probably did not consider some important biophysical considerations which have only recently been revealed by *in vivo* studies: the abolishment of cluster activity following the removal of glutamatergic synapses[20,29], the existence of a profound inhibitory effect of GABAergic transmission at the network level[20,29] and its non-excitatory (but depolarizing) effect at the neuron level[20,31] during the first postnatal week, or that the loss of large cluster activity occurs around eye-opening[2,3] and not around P7[41]. In contrast, here, (i) we used a unified computational model which takes into account most of these recently reported biophysical considerations (see Supplementary Method and Table 1), (ii) our work shows results based on, and mainly in accordance to the recent *in vivo* studies, where these studies revealed some critical features different from those reported for *in vitro* data, (iii) we studied the whole developmental period, comprising the time course of sparsification, and not only a single postnatal stage, (iv) we not only address the possible underlying mechanism of the postnatal cluster activity generation, but also the developmental changes in the operating regimes and information processing capabilities, as well as the possible refinements in network properties governing the sparsification.

There are advantages and limitations of our modeling approach. Clearly, as compared to a mean-field model as employed here, a spiking network model can in principle provide more detailed results, e.g. one could model the temporal sparseness of spiking activities, or the specific patterns of sensory inputs at the neuron level. However, for this early developmental period, we are not aware of any established neuron model. For such a model, a considerable amount of unspecified neurobiological parameters is required to be measured experimentally first. Instead, using a mean-field model enabled us to forgo such detailed parameterizations by considering only their average characteristics over the network. Although this procedure comes at the price of removing biological details, this enabled us to use an extended Wilson-Cowan-type model[13]; a well-established model and extensively used before to study adult networks behavior[18,42]. This model enabled us to incorporate the available, experimentally reported developmental trajectories of intrinsic neuronal and synaptic parameters (see Supplementary Method and Table 1), including short-term synaptic plasticity. In addition to its biophysical interpretability, this model is in general mathematically tractable which allowed us to derive analytical expressions, e.g. in our stability analyses (see Supplementary Methods). Moreover, this model is readily extendable to incorporate other biophysical mechanisms like spike-frequency adaptation, or to build a spatial graph of multiple homogenous and heterogeneous inter-connected networks to study, e.g. the activity propagation over different brain areas.

In sum, we have shown that by establishing and extending a novel application of an existing computational model to immature networks and integrating recent experimental findings, new mechanistic insights into the development of neural networks can be obtained. We expect that, in the future, this modelling approach can also guide research by providing for concrete predictions that can be tested experimentally.

Methods

Here, we briefly describe the main components of our model and the analyses. A detailed description can be found in Supplementary Methods.

STP-RNN model. This model (Fig. 1a) is an extended version of Wilson-Cowan's recurrent neural network (RNN) mean-field model[43], for which the short-term plasticity (STP) of synaptic connections were also modeled[13]. The equations governing the model dynamics over time are (dots denote the time derivatives):

$$\begin{aligned}
\tau_E \dot{E}_r(t) &= -E_r(t) + G_E(J_{EE}\, u_{EE}(t)\, x_{EE}(t)\, E_r(t) - J_{EI}\, u_{EI}(t)\, x_{EI}(t)\, I_r(t) + e_E(t) - \theta_E) \\
\tau_I \dot{I}_r(t) &= -I_r(t) + G_I(J_{IE}\, u_{IE}(t)\, x_{IE}(t)\, E_r(t) - J_{II}\, u_{II}(t)\, x_{II}(t)\, I_r(t) + e_I(t) - \theta_I) \\
\dot{x}_{ij} &= \tau_{r_{ij}}^{-1}\left(1 - x_{ij}(t)\right) - u_{ij}(t)\, x_{ij}(t) A_j(t) \\
\dot{u}_{ij} &= \tau_{f_{ij}}^{-1}\left(U_{ij} - u_{ij}(t)\right) + U_{ij}\left(1 - u_{ij}(t)\right) A_j(t)
\end{aligned}$$

where j and i $\in$ {E, I}, $A_j \in \{E_r, I_r\}$, j is the index of presynaptic population, E_r (=A_E) and I_r (=A_I) are the average activity (in hertz) of E- and I-populations which receive, respectively, the external inputs e_E and e_I, e.g., from other brain regions, G_i is the linear input-output gain above population activity threshold θ_i (otherwise $G_i = 0$), and x_{ij} and u_{ij} are the dynamic variables of short-term synaptic depression and facilitation mechanisms. The parameter definitions and values are listed in Table 1. A STP-RNN with synaptic efficacies frozen at the FP is called Frozen STP-RNN (a Static-RNN-type model).

Phase plane components. E_r-I_r-plane is the 2D phase plane of E- and I-population activity rates (I_r vs. E_r), in which the E_r- and I_r- nullclines are represented as the set of points for which $dE_r/dt = 0$ and $dI_r/dt = 0$, respectively. For a STP-RNN, the depicted quasi E_r and I_r nullclines in E_r-I_r-plane are based on the reduced STP-RNN (Supplementary equation (7)). Any intersection of these two quasi nullclines (i.e. the FP) can represent the steady state of the whole network (i.e. the 10D STP-RNN).

Stability of FPs. To determine the stability of any FP of interest we applied linear stability analysis to our 10D STP-RNNs (or 2D Frozen STP-RNNs): We investigated whether all eigenvalues of the network's system of equations linearized around the FP (using the Jacobian matrix) have strictly negative real parts (if so, the FP is stable), or whether at least one eigenvalue with positive real part exists (if so, the FP is unstable). This can be re-stated as: A FP is stable if following a small perturbation from that FP (at which the network was before perturbation), the network dynamics converge back to it. Conversely, if the dynamics move away from the FP or dies out, that FP is unstable.

Operating regimes and FP-domains. The stable operating regimes of a RNN at a FP can be classified as an inhibition-stabilized network (ISN) vs. a Non-ISN[25,26]. To discriminate between these two regimes three criteria were defined: (**A**) Excitatory instability: For the inhibitory activity rate fixed at the FP, the recurrent excitation is strong enough to render the E-population intrinsically unstable. (**B**) Excitatory stability: In contrast to (**A**), the E-population is stable *per se*, i.e. even with a feedback inhibition fixed at its level at the FP. (C) Overall stability: The dynamic feedback inhibition to the E-population is strong enough to stabilize the whole network activity. At a FP, a network operating under the (**A**) and (C) criteria is an ISN, while a network operating under the (**B**) and (C) criteria is a Non-ISN. A network, which is neither ISN nor Non-ISN at the FP, operates under an unstable regime.

We partition the E_r-I_r-plane into different domains of operating regimes (FP-domains). Each FP-domain contains all potential steady states (i.e. FPs) at which the network could operate under the corresponding regime. The area of each FP-domain is computed numerically as *AOD* (area of domain). Note that the borders between the FP-domains (Fig. 3a) were determined by using numerical simulations, when we plotted the FP-domains of operating regimes based on their stability criteria (**A**-C) obtained analytically in Supplementary Methods (see "Characterization of operating regimes" section in Supplementary Methods).

Cluster activity size and duration. In a RNN, the cluster activity (network spike; PS_{net}) usually involves the population spikes[44,45] in both E (PS_E) and I (PS_I) populations. To approximate cluster activity size, i.e. the total number of neurons synchronized during a cluster activity, we calculate $PS_{net}^{amp} = \omega \times (A_{sum}^{amp} - A_{sum}^{0})$ (a dimensionless parameter), where $A_{sum} = E_r + I_r$ is the sum of the activity of E- and I-populations (in hertz), A_{sum}^{amp} and A_{sum}^{0} are the maximal activity during the cluster activity and the preceding activity, respectively, and ω is a scaling factor (in units of [Hz^{-1}]) to convert the activity rate to an approximate number of activated neurons during the cluster activity. For simplicity, we set $\omega = 1$, since its veridical value is not defined for the mean-field model. We measure the cluster activity duration as its termination time minus its onset time.

Computation of $ratio_{PS}$ and $ratio_{AOD}$. To investigate the impact of specific maturational processes on sparsification (as used in Fig. 5), we first substituted single parameters or a small combination of parameters at P10 by their values at P20 (Table 1), followed by the computation of the $ratio_\gamma = 100 \times \varpi\ (\gamma_{P10}^{res} - \gamma_{P10})/(\gamma_{P20} - \gamma_{P10})$, where for $ratio_{PS}$ we set $\gamma = PS_{net}^{amp}$ with $\varpi = -1$, and for $ratio_{AOD}$ we set $\gamma = AOD_{ISN/Unstable}$ with $\varpi = +1$. γ_{P10}^{res} is the value of γ measured after the parameter(s) value(s) substitution.

Data availability. Custom Matlab and Mathematica codes for our model are available upon request from the corresponding author.

References

1. Khazipov, R. & Luhmann, H. J. Early patterns of electrical activity in the developing cerebral cortex of humans and rodents. *Trends Neurosci.* **29**, 414–418 (2006).
2. Golshani, P. *et al.* Internally mediated developmental desynchronization of neocortical network activity. *J Neurosci.* **29**, 10890–10899 (2009).
3. Rochefort, N. L. *et al.* Sparsification of neuronal activity in the visual cortex at eye-opening. *Proc Natl Acad Sci USA.* **106**, 15049–15054 (2009).
4. Kerr, J. N., Greenberg, D. & Helmchen, F. Imaging input and output of neocortical networks *in vivo*. *Proc Natl Acad Sci USA* **102**, 14063–14068 (2005).
5. Olshausen, B. A. & Field, D. J. Sparse coding of sensory inputs. *Curr Opin Neurobiol.* **14**, 481–487 (2004).
6. Shadlen, M. N. & Newsome, W. T. Noise, neural codes and cortical organization. *Curr Opin Neurobiol.* **4**, 569–579 (1994).
7. Colonnese, M. T. *et al.* A conserved switch in sensory processing prepares developing neocortex for vision. *Neuron.* **67**, 480–498 (2010).
8. Vanhatalo, S. *et al.* Slow endogenous activity transients and developmental expression of K+-Cl- cotransporter 2 in the immature human cortex. *European Journal of Neuroscience.* **22**, 2799–2804 (2005).
9. Luhmann, H. J. *et al.* Spontaneous Neuronal Activity in Developing Neocortical Networks: From Single Cells to Large-Scale Interactions. *Frontiers in Neural Circuits.* **10**, https://doi.org/10.3389/fncir.2016.00040 (2016).
10. Etherington, S. J. & Williams, S. R. Postnatal development of intrinsic and synaptic properties transforms signaling in the layer 5 excitatory neural network of the visual cortex. *J Neurosci.* **31**, 9526–9537 (2011).
11. De Felipe, J., Marco, P., Fairen, A. & Jones, E. G. Inhibitory synaptogenesis in mouse somatosensory cortex. *Cereb Cortex.* **7**, 619–634 (1997).
12. Feldmeyer, D. & Radnikow, G. Developmental alterations in the functional properties of excitatory neocortical synapses. *Journal of Physiology-London.* **587**, 1889–1896 (2009).
13. Tsodyks, M., Pawelzik, K. & Markram, H. Neural networks with dynamic synapses. *Neural Comput.* **10**, 821–835 (1998).
14. Abbott, L. F., Varela, J. A., Sen, K. & Nelson, S. B. Synaptic depression and cortical gain control. *Science.* **275**, 220–224 (1997).
15. Zucker, R. S. & Regehr, W. G. Short-term synaptic plasticity. *Annu Rev Physiol.* **64**, 355–405 (2002).
16. Haider, B., Duque, A., Hasenstaub, A. R. & McCormick, D. A. Neocortical network activity *in vivo* is generated through a dynamic balance of excitation and inhibition. *J Neurosci.* **26**, 4535–4545 (2006).
17. Petersen, C. C., Hahn, T. T., Mehta, M., Grinvald, A. & Sakmann, B. Interaction of sensory responses with spontaneous depolarization in layer 2/3 barrel cortex. *Proc Natl Acad Sci USA.* **100**, 13638–13643 (2003).
18. Barak, O. & Tsodyks, M. Persistent activity in neural networks with dynamic synapses. *PLoS Comput Biol.* **3**, e35, https://doi.org/10.1371/journal.pcbi.0030035 (2007).
19. Millman, D., Mihalas, S., Kirkwood, A. & Niebur, E. Self-organized criticality occurs in non-conservative neuronal networks during Up states. *Nat Phys.* **6**, 801–805 (2010).
20. Kirmse, K. *et al.* GABA depolarizes immature neurons and inhibits network activity in the neonatal neocortex *in vivo*. *Nat Commun.* **6**, https://doi.org/10.1038/ncomms8750 (2015).
21. Rigas, P. *et al.* Spontaneous Up states *in vitro*: a single-metric index of the functional maturation and regional differentiation of the cerebral cortex. *Front Neural Circuits.* **9**, 59, https://doi.org/10.3389/fncir.2015.00059 (2015).
22. Shu, Y., Hasenstaub, A. & McCormick, D. A. Turning on and off recurrent balanced cortical activity. *Nature.* **423**, 288–293 (2003).
23. Prida, L. M. & Sanchez-Andres, J. V. Nonlinear frequency-dependent synchronization in the developing hippocampus. *J Neurophysiol.* **82**, 202–208 (1999).
24. Cossart, R., Aronov, D. & Yuste, R. Attractor dynamics of network UP states in the neocortex. *Nature.* **423**, 283–288 (2003).

25. Ozeki, H., Finn, I. M., Schaffer, E. S., Miller, K. D. & Ferster, D. Inhibitory stabilization of the cortical network underlies visual surround suppression. *Neuron.* **62**, 578–592 (2009).
26. Tsodyks, M. V., Skaggs, W. E., Sejnowski, T. J. & McNaughton, B. L. Paradoxical effects of external modulation of inhibitory interneurons. *J Neurosci.* **17**, 4382–4388 (1997).
27. Latham, P. E. & Nirenberg, S. Computing and stability in cortical networks. *Neural Comput.* **16**, 1385–1412 (2004).
28. Chagnac-Amitai, Y. & Connors, B. W. Horizontal spread of synchronized activity in neocortex and its control by GABA-mediated inhibition. *J Neurophysiol.* **61**, 747–758 (1989).
29. Minlebaev, M., Ben-Ari, Y. & Khazipov, R. Network mechanisms of spindle-burst oscillations in the neonatal rat barrel cortex *in vivo*. *J Neurophysiol.* **97**, 692–700 (2007).
30. Rahmati, V., Kirmse, K., Marković, D., Holthoff, K. & Kiebel, S. J. Inferring Neuronal Dynamics from Calcium Imaging Data Using Biophysical Models and Bayesian Inference. *PLoS Comput Biol.* **12**, e1004736, https://doi.org/10.1371/journal.pcbi.1004736 (2016).
31. Valeeva, G., Tressard, T., Mukhtarov, M., Baude, A. & Khazipov, R. An Optogenetic Approach for Investigation of Excitatory and Inhibitory Network GABA Actions in Mice Expressing Channelrhodopsin-2 in GABAergic Neurons. *J Neurosci.* **36**, 5961–5973 (2016).
32. Ben-Ari, Y., Gaiarsa, J. L., Tyzio, R. & Khazipov, R. GABA: a pioneer transmitter that excites immature neurons and generates primitive oscillations. *Physiol Rev.* **87**, 1215–1284 (2007).
33. Kirmse, K., Witte, O. W. & Holthoff, K. GABAergic depolarization during early cortical development and implications for anticonvulsive therapy in neonates. *Epilepsia.* **52**, 1532–1543 (2011).
34. Bakkum, B. W., Benevento, L. A. & Cohen, R. S. Effects of light/dark- and dark-rearing on synaptic morphology in the superior colliculus and visual cortex of the postnatal and adult rat. *J Neurosci Res.* **28**, 65–80 (1991).
35. Hopfield, J. J. Neural networks and physical systems with emergent collective computational abilities. *Proc Natl Acad Sci USA.* **79**, 2554–2558 (1982).
36. Wang, X. J. Synaptic reverberation underlying mnemonic persistent activity. *Trends Neurosci.* **24**, 455–463 (2001).
37. Seung, H. S., Lee, D. D., Reis, B. Y. & Tank, D. W. Stability of the memory of eye position in a recurrent network of conductance-based model neurons. *Neuron.* **26**, 259–271 (2000).
38. Ben-Yishai, R., Bar-Or, R. L. & Sompolinsky, H. Theory of orientation tuning in visual cortex. *Proc Natl Acad Sci USA* **92**, 3844–3848 (1995).
39. Jeong, H. Y. & Gutkin, B. Synchrony of neuronal oscillations controlled by GABAergic reversal potentials. *Neural Comput.* **19**, 706–729 (2007).
40. Luccioli, S., Ben-Jacob, E., Barzilai, A., Bonifazi, P. & Torcini, A. Clique of functional hubs orchestrates population bursts in developmentally regulated neural networks. *PLoS Comput Biol.* **10**, e1003823, https://doi.org/10.1371/journal.pcbi.1003823 (2014).
41. Garaschuk, O., Linn, J., Eilers, J. & Konnerth, A. Large-scale oscillatory calcium waves in the immature cortex. *Nat Neurosci.* **3**, 452–459 (2000).
42. Mongillo, G., Barak, O. & Tsodyks, M. Synaptic theory of working memory. *Science.* **319**, 1543–1546 (2008).
43. Wilson, H. R. & Cowan, J. D. Excitatory and inhibitory interactions in localized populations of model neurons. *Biophys J.* **12**, 1–24 (1972).
44. Loebel, A. & Tsodyks, M. Computation by ensemble synchronization in recurrent networks with synaptic depression. *J Comput Neurosci.* **13**, 111–124 (2002).
45. Tsodyks, M., Uziel, A. & Markram, H. Synchrony generation in recurrent networks with frequency-dependent synapses. *J Neurosci.* **20**, 1–5 (2000).

Acknowledgements

This work was supported by the Open Access Publication Funds of the TU Dresden, the Priority Program 1665 of the German Research Foundation (HO 2156/3-1/2, KI 1816/1-1/2 and KI 1638/3-1/2), the Collaborative Research Center/Transregio 166 of the German Research Foundation (B3 to KH and KK), the Research Group FO 1738 (WI 830/10-2 to KH), the Federal Ministry of Education and Research (01GQ0923 to KH) and the Interdisciplinary Centre for Clinical Research Jena (to KK and KH). The funders had no role in study design, data collection and analysis, decision to publish, or preparation of the manuscript.

Author Contributions

V.R., K.K., K.H., L.S. and S.J.K. designed the study. V.R. designed the model, derived analytical expressions, and ran the experiments. V.R., K.K., K.H., L.S. and S.J.K. participated in the interpretation of the data and findings. V.R., K.K., K.H., L.S. and S.J.K. wrote the manuscript.

Additional Information

Supplementary information accompanies this paper at https://doi.org/10.1038/s41598-017-13468-z.

Competing Interests: The authors declare that they have no competing interests.

Publisher's note: Springer Nature remains neutral with regard to jurisdictional claims in published maps and institutional affiliations.

5. Discussion

In this thesis, we focused on two goals: i) developing novel methods for extracting information about biophysical parameters and variables as well as spiking activities, underlying calcium imaging data, and ii) using these data in combination with well-established computational modeling methods to investigate sparsification as an essential, universal phenomenon of neural networks maturation. In the following, we discuss the results that we obtained towards these two goals.

5.1. Calcium imaging processing methods

Extracting quantities of interest from the recorded fluorescence traces remains still challenging, mainly due to the intrinsic slow [Ca^{2+}] kinetics *per se* as compared to the time scale of spikes, and different types of noise and artifacts. The proposed reconstruction methods (e.g. see (Greenberg et al. 2008, Grewe et al. 2010, Park et al. 2013, Sasaki et al. 2008, Vogelstein et al. 2010, Vogelstein et al. 2009, Yaksi und Friedrich 2006, Pnevmatikakis et al. 2016)) to overcome these issues have certain limitations in e.g. making inference about biophysical quantities underlying the fluorescence traces, performing a fast processing of long-term data, adapting readily to the variability in kinetics of fluorescence transients, and minimizing the need for user interaction. Accordingly, we developed two novel methods for analyzing calcium imaging data: CaBBI (Calcium imaging Analysis using Biophysical models and Bayesian Inference) (Rahmati et al. 2016) and UFARSA (Ultra-fast Accurate Reconstruction of Spiking Activity) (Rahmati et al. 2018). We discuss these two methods in the following sections.

5.1.1. CaBBI: novelty of the method

CaBBI (Rahmati et al. 2016) is a novel probabilistic, neuronal deconvolution-based method. It is the first method which enables making inference about the biophysical variables and parameters underlying calcium imaging data. To develop this method, we pursued the idea that the principled knowledge about neuronal dynamics, including spike and burst generation mechanisms, can be employed to infer the underlying biophysical quantities. CaBBI uses a variational Bayesian inference method (Daunizeau et al. 2014, Daunizeau et al. 2009) to invert the biophysical generative models of fluorescence data. As generative models, we proposed to use novel biophysical models which create a direct and parsimonious link between the neuronal dynamics, e.g. the membrane potential (rather than only the spikes), and fluorescence trace; such biophysically informed generative models have not been introduced before, and have specific

advantages which we discuss in next section. We derived three different generative models, which are based on the well-known FitzHugh-Nagumo (FHN) neuron model (FitzHugh 1955, Fitzhugh 1961) or two novel neuron models that we developed in this thesis; i.e. the Quadratic-Gaussian integrate-and-fire (QGIF) and Bursting-QGIF neuron models. The QGIF (1D) and Bursting-QGIF (2D) are non-hybrid (i.e. differentiable) I&F models, where, with a minimum number of neuronal variables, they can emulate different spiking and bursting patterns observed in electrophysiological data. By developing the family of QGIF-family neuron models, we aimed at reducing the model complexity for model inversion.

5.1.2. CaBBI: advantages and limitations

To the best of the author's knowledge, CaBBI is the first method which enables making inference about the intrinsic neuronal dynamics (e.g. membrane potential or $[Ca^{2+}]$ kinetics) and biophysical parameters (e.g. the conductance of voltage-gated channels), underlying calcium imaging data. This unique feature of CaBBI is a result of its biophysical modeling basis, where biologically interpretable spiking and bursting neuronal models are used as generative models. In addition, this feature of CaBBI enables it to directly infer and quantify the changes in biophysical parameters, caused by e.g. a selective pharmacological manipulation. Importantly, this allows the user to test specific hypotheses by assigning appropriate priors which are susceptible for the expected changes due to an intervention. Although not shown here, by using formal model comparisons, including Bayesian model selection (Rigoux et al. 2014, Stephan et al. 2009), the user can then proceed by comparing this change-sensitive model against an alternative model that does not expect this change. As such an application, we showed that CaBBI can reliably infer the changes in calcium decay time-constant and in M-type potassium channels, which had been caused by simulated pharmacological interventions.

Using biophysically informed generative models has also the great advantage of constraining the possible fluorescence kinetics and variations. This is important in making the inference robust against noise sources which are unlikely to be generated by the generative models. Moreover, the Bayesian approach of CaBBI enables the user to incorporate prior knowledge about the values or about the plausible range of biophysical quantities. To this end, the user can choose the width of the prior distributions to effectively inform the inversion to what extent the parameters should be determined from the data or by prior knowledge. Using model comparison techniques can then

enable selecting the best model among different prior expectations (Rigoux et al. 2014, Stephan et al. 2009) (not shown in this thesis).

Finally, we showed that CaBBI is not only robust against measurement noise, but can be intrinsically adapted to fluorescence transients with rather variable rise and decay kinetics. This is because CaBBI is informed by its biophysical generative models about the possible kinetics. This is important because methods based on fixed or prototypical templates of fluorescence transients (Greenberg et al. 2008, Grewe et al. 2010, Kerr et al. 2005b, Yaksi und Friedrich 2006, Kerr et al. 2007) or model-based methods assuming, e.g., only sharp rise kinetics (Vogelstein et al. 2010, Vogelstein et al. 2009) may face severe difficulties in handling data with rather variable transient shapes and slow rise kinetics, respectively. For example, such slow rise kinetics lasting several hundred milliseconds can be observed in the recordings with genetically-encoded fluorescence calcium indicators (Chen et al. 2013b, Reiff et al. 2005, Lin und Schnitzer 2016), or in our data recorded from immature hippocampal neurons; see also (Takano et al. 2012). In particular, by applying CaBBI to these neonatal data, without any manual interaction to adapt the method parameters, we were able to reconstruct the spatiotemporal patterns of cellular activation during giant depolarizing potential (GDPs) waves in hippocampus (Ben-Ari et al. 2007, Takano et al. 2012). This indicates that CaBBI can also be used as a reliable method to infer the complex characteristics of immature neural networks.

Beyond the novel features of CaBBI, it has however some limitations. All of these limitations can be overcome by extensions and further development of the method but require future work. One of them is its need for rather long computer run times to process a fluorescence trace, as compared to established methods (Sasaki et al. 2008, Vogelstein et al. 2010). This is mainly due to the Bayesian framework that we used and also the implementation in Matlab. Secondly, to avoid over-parameterization and reducing the complexity of the generative models for inversion we had to fix many parameters and use suitable priors, based on previous experimental studies. This was necessary to preclude CaBBI from being too unconstrained, and also to guide the inversion to explore in, and converge to, biologically interpretable parameter regimes. Third, the currently used generative models of CaBBI are not able to infer spike counts from the amplitude of fluorescence transient: The transient amplitudes can in principle encode the number of spikes underlying those transients. This limitation is presumably due to the biophysical essence of

spiking and bursting neuron models which we used in CaBBI, where each transient is essentially considered to be evoked by one spike, regardless of the transient amplitude.

In sum, CaBBI, rather than being a pure reconstruction method only, is the first method which enables analysis of calcium imaging data in term of underlying biophysical parameters and variables.

5.1.3. UFARSA: novelty of the method

Inferring other biophysical quantities than spiking activity might be unnecessary for experiments which require only the underlying firing patterns to address their questions. Therefore, we developed UFARSA as a novel heuristic, model-free-type method, focusing on spiking activity reconstruction only (Rahmati et al. 2018). UFARSA provides several advantages in this specific task, while avoiding the rather complex inversion process of CaBBI. This method is mainly based on a set of new, heuristic algorithms, which can be subdivided into five components: i) Pre-processing, ii) Reconstruction, iii) Timing correction, iv) Spike-count estimation, and v) Demerging. In a sequential manner, UFARSA applies these components to a given fluorescence trace to reconstruct the underlying spiking activities, i.e. both event time and spike count per fluorescence transient.

5.1.4. UFARSA: advantages and limitations

A main feature of UFARSA is its capability in providing a near-automatic reconstruction of spiking activities. All the established methods, to the best of the author's knowledge, have at least one parameter required to be set by the user for new data; i.e. for data which were recorded under a different setting than those used to develop that method. For instance, such a manual parametrization is required in template matching method to determine, at least, a new template of fluorescence transient, or in the fast filter method to set a new threshold for extracting inferred spiking activities (Clements und Bekkers 1997, Greenberg et al. 2008, Grewe et al. 2010, Kerr et al. 2007, Kerr et al. 2005b). However, in the absence of joint electrophysiological data, which is a common situation for calcium imaging recordings, finding optimal parameter values is practically not possible. Consequently, the selection of parameter values, and thus the reconstruction accuracy, usually depends on the user's experience with the specific method and the data at hand. In contrast, UFARSA allows for a near-automatic reconstruction from different fluorescence data types (e.g. differing in terms of their rise and decay kinetics). The main two reasons for this feature are as follows. First, we have proposed a data-driven approach for setting the central

parameter (i.e. the leading threshold) of UFARSA. This approach allows the user to effectively avoid the typical search process for optimal parameter values; in contrast to most of the established methods such as (Clements und Bekkers 1997, Greenberg et al. 2008, Grewe et al. 2010, Vogelstein et al. 2010, Vogelstein et al. 2009, Yaksi und Friedrich 2006). The second reason lies in the model-free essence of UFARSA which enables it to automatically adapt to transients with different rise and decay kinetics or amplitudes, both within and across fluorescence traces (or region of interest; ROIs). This is in contrast to most of the model- or template-based methods (Clements und Bekkers 1997, Greenberg et al. 2008, Grewe et al. 2010, Kerr et al. 2007, Kerr et al. 2005b, Vogelstein et al. 2010, Vogelstein et al. 2009). Moreover, UFARSA can use the variability in the transient amplitudes presented within in a fluorescence trace to estimate the spike count per transient. Such an estimation of the number of spikes underlying a transient is not possible for e.g. CaBBI; it considers each transient to be evoked by maximum one spiking event (e.g. one spike).

Beyond its near-automatic feature, UFARSA is an ultra-fast reconstruction method. Why is this important? Long-term calcium imaging and data recorded at a high sampling frequency (e.g. 1 kHz) can enable studying long-term neural activity patterns with a high temporal resolution (Grewe et al. 2010, Grienberger und Konnerth 2012, Prevedel et al. 2016). However, analyzing such data remains challenging due to at least two issues: i) the measurement noise is effectively increased by increasing the imaging sampling frequency, and ii) a fast reconstruction method is required to process, in a reasonable short time, these large data sets which typically have millions of frames. With respect to the first issue, we found that increasing sampling frequency increases the reconstruction accuracy of UFARSA, even under relatively low SNR conditions. This is mainly because the superimposed transients are better resolved (discriminated) at higher temporal resolutions, which in turn improves the event detection procedure in UFARSA. Regarding the second issue, we showed that UFARSA is an ultra-fast method which, even when using a standard modern desktop computer, requires less than 2 seconds for processing a fluorescence trace extracted from 1,000,000 frames. This means that the user can perform the reconstruction of data recorded from e.g. 20 ROIs (or neurons) for 1000 seconds at a sampling frequency of 500 Hz, in less than 20 seconds. This makes UFARSA faster than previously established methods; e.g. UFARSA is at least one order of magnitude faster than the fast filter which needs around 1 second for deconvolving a trace of 50,000 time points (Vogelstein et al. 2010).

As any method, UFARSA also comes with some limitations. First, before performing the actual reconstruction, the automatic smoothing method used by UFARSA may lead to merging of some superimposed fluorescence transients. To handle such cases, we introduced a specific algorithm to demerge such transients so that the underlying spikes can be reconstructed. However, especially under low SNR traces or high firing rates, this demerging algorithm does not guarantee to demerge all such transients. The second limitation lies in the fact that the reconstruction algorithm behind UFARSA is mainly based on transient amplitudes. That is, it is potentially sensitive to deflection artefacts in fluorescence traces, where it may falsely consider the upward-phase of a deflection to be a transient's rising phase. In addition to our introduced deflection removal algorithms in UFARSA, new methods may be required to improve handling, in particular, the short-lasting positive deflection artifacts. Third, to estimate the spike count per fluorescence transient UFARSA uses the variability in the amplitudes of transients detected within a trace, independently from other traces. Therefore, its spike count estimation accuracy is likely to reduce in the absence of sufficient information, conveyed by transient amplitudes about their underlying spike counts. Therefore, UFARSA may be extended to include a new algorithm to perform a simultaneous, or recursive, reconstruction of whole data set. This will enable using the overall amplitude variability in the data set for spike count estimation, which can in turn increase its accuracy. Finally, lowering the detection threshold of UFARSA to potentially improve the spike count estimation accuracy may instead lead to overestimation. This is because lowering the threshold can make UFARSA more prone to a false detection of relatively small, non-spike-evoked transients like neuropil activity.

In sum, we believe that UFARSA, as an ultra-fast near-automatic method, is a suitable method for accurately reconstructing the spiking activity from large calcium imaging data sets, under a wide range of variabilities in the transient kinetics, sampling frequencies, firing rates, and SNRs.

5.2. Sparsification

Recent *in vivo* calcium imaging experiments, covering the first postnatal month in rodents, have provided a continuous monitoring of the sparsification process in intact cortex (Golshani et al. 2009, Rochefort et al. 2009). These data show explicitly that network activity undergoes a dramatic transition from large cluster activity to a relatively sparse mode around the time of eye-opening. Moreover, previous electrophysiological recordings have measured the developmental trajectory of several intrinsic neuronal and synaptic parameters (De Felipe et al. 1997,

Etherington und Williams 2011, Feldmeyer und Radnikow 2009, Golshani et al. 2009), including STP (Etherington und Williams 2011, Feldmeyer und Radnikow 2009). Despite these established experimental findings, the mechanisms underlying sparsification, and whether or how the developmental changes in network dynamics and those in intrinsic neuronal and synaptic properties are linked, remain largely unknown.

5.2.1. Computational, dynamic systems modeling

Considering the experimentally measured developmental trajectory of network activity measured by calcium imaging and those of the intrinsic neuronal and synaptic parameters, we proposed to use a computational, dynamic systems modeling approach to investigate the sparsification (Rahmati et al. 2017).

We first modeled the *in vivo* activity of a developing neural network on the basis of the established experimental findings, during the first postnatal month. As a neural network model, we used an extended version of the Wilson-Cowan-type model, which accounts for both types of STP (Tsodyks et al. 1998); i.e. synaptic depression and facilitation mechanisms, rendering the synaptic strengths dynamic over time (Zucker und Regehr 2002). This neural network model is well-established and has been already used extensively to study the behavior of adult networks (Barak und Tsodyks 2007, Mongillo et al. 2008). The network is of a mean-field type and models the mean firing activity rates of one excitatory and one inhibitory neuronal population with both reciprocal- and self-synaptic connections. It has the advantage of being mathematically accessible and biophysically interpretable. Besides, it enables studying the developing neural networks based on the average effects of the experimentally measured parameters, at the network level. This is important, because currently no well-established immature (or developing) neuron model exists to allow for a spiking neural network study. Presumably, this is because many neuronal and synaptic parameters are unspecified and in principle need to be measured first, for this developmental period. Nonetheless, using the available experimental data, we were able to parameterize the network for four postnatal days (P): P3 (period of physiological blindness), P10 (a few days before eye-opening), P14 (the day after eye-opening) and P20 (a few days after eye-opening). Selecting these postnatal stages for network parameterization allowed us to cover the developmental states of visual cortical networks from before to after the time of eye-opening.

Subsequently, we used the mathematical tool of stability analysis, as a well-established dynamic system approach (Izhikevich 2007), along with network simulations to study this developing

network model, in order to provide the first mechanistic insights into the developmental emergence of sparse coding.

5.2.2. Underlying mechanisms

Our results shed light on several aspects of sparsification. These include the cluster activity generation and its spatiotemporal characteristics, the specific maturational processes being essential for mediating the transition from dense to sparse coding, the potential developmental refinements in network information processing capabilities, and the role of GABA at the network level. In the following we discuss these points.

First, we surprisingly found that a particular combination of strong synaptic depression and a transient unstable state, hidden in network fast (i.e. firing) dynamics allows the developing networks (P3 to P20) to either be mostly silent for relatively long periods or generate cluster activity. Besides, we found that the network is of a mono-stable type before eye-opening, with only one fixed point (FP) which is its stable rest state. Therefore, it can be concluded that the cluster activity generation mechanism at these early developmental stages is in stark contrast to those proposed for adult networks' cluster activity, mainly due to the usual assumption of bi- or multi-stable networks (Barak und Tsodyks 2007, Millman et al. 2010).

Secondly, our results provide for an explanation of previous experimental results suggesting that sparsification is dominantly mediated by intrinsic factors (Colonnese et al. 2010, Golshani et al. 2009, Rochefort et al. 2009), whereas sensory experience during the first days after eye-opening may have only a modulatory contribution to this phenomenon (Rochefort et al. 2009). This is mainly because i) our computational modeling study, by harnessing experimentally measured developmental trajectories of intrinsic neuronal and synaptic parameters, revealed that sparsification is profoundly dependent on an elaborate, parallel refinement of not only absolute synaptic efficacies but also on both STP and intrinsic membrane properties, and background activity, and ii) experimental studies found that sensory deprivation has only a modest effect on the total synapse numbers (Bakkum et al. 1991).

Thirdly, we sought to address how the sparsification process prepares an *in vivo* developing network for an effective processing of sensory inputs towards the time of eye-opening. Intriguingly, we found, in our model, that sparsification translates not only to a developmental reduction in the instability of network firing activity but also to an effective availability of the inhibition-stabilized network (ISN; vs. Non-ISN) regime as well as the emergence of spontaneous

attractors and state transition mechanisms. These results provide novel insights into developmental refinements in network information processing capabilities. For instance, we found that Non-ISN and instability may be the dominating regimes of the network before eye-opening, and ISN regime becomes effectively available only afterwards. The Non-ISN regime allows immature networks to maintain their stability without a need for inhibitory transmission, while developmental increasing availability of ISN regime may enable the developing network for processing complex computations (Latham und Nirenberg 2004). Interestingly, some experimental observations indicate that adult cortical networks operate under an ISN regime (Chagnac-Amitai und Connors 1989, Ozeki et al. 2009). Moreover, the emergence of spontaneous attractors and state transition mechanisms (i.e. transition between FPs) in our model may be thought of as an early step towards representation of perceptual stimuli in developing networks.

Fourthly, we addressed the open question about the role of GABA at the network level during the first postnatal week. In our model, we found that blocking inhibitory, but not excitatory, GABAergic synapses leads to a decrease in cluster activity size. Interestingly, this result supports recent *in vivo* findings that GABA inhibits intact immature networks in neocortex and hippocampus (Kirmse et al. 2015, Valeeva et al. 2016, Minlebaev et al. 2007). At the same time, this result is in contrast to the findings of most *in vitro* studies reporting that GABA acts as excitatory or both excitatory and inhibitory at the network level (Ben-Ari et al. 2007). Importantly, our modeling result indicates that even when GABA is able to depolarize immature neurons *in vivo* (Kirmse et al. 2015), it can still confine the cluster activity size (as also observed experimentally (Kirmse et al. 2015)) via attenuating the instability effect on network activity.

In sum, this work, by providing a strong link between experimental findings and model behavior, elucidates how adult sparse coding networks may emerge developmentally.

5.3. Conclusion and outlook

Taken together, in this thesis we introduced novel reconstruction methods (CaBBI and UFARSA) for calcium imaging data, and presented a unified modeling approach, enabling us to combine findings based on these data with a well-established computational modeling approach, to elucidate novel mechanistic insights into the developmental emergence of sparse coding.

By developing CaBBI, we could provide a novel way of analyzing calcium imaging data in terms of biophysical parameters and variables. In contrast to established reconstruction methods,

CaBBI will enable the experimenters to reliably access the underlying biophysical quantities (rather than only spiking activities), and infer, or even test specific hypothesis regarding, the changes in biophysical parameters; e.g. caused by pharmacological interventions. Moreover, CaBBI can be considered as the first step toward establishing "spiking neural networks" of biophysical neuron models, where an extension of its generative models should enable inferring the network's biophysical quantities, from large-scale calcium imaging data.

By developing UFARSA, we provided for an ultra-fast, near-automatic method for an accurate reconstruction of spiking activities. Importantly, we expect UFARSA, relative to other methods, to notably speed up and ease the analysis of e.g. long-term calcium imaging data or data showing systematic variation in the transient kinetics or firing rates, and at the same time to minimize the need for user interaction or experience in the method. Furthermore, it will allow experimenters to perform an effective correction of frequently observed artifacts, including fast large negative deflections or rather complex, low frequency component temporal drifts. This artifact-correction can in turn enable more reliable post-processing analysis of the data.

By establishing and extending a novel application of a well-established computational modeling approach to developing neural networks, along with integrating recent experimental findings (including those based on calcium imaging), we could elucidate mechanistically how adult sparse coding networks emerge developmentally. In particular, we addressed the potential mechanisms governing cluster activity generation and its spatiotemporal characteristics, the specific maturational processes mediating sparsification process, as well as the developmental refinements in network information processing capabilities preparing it for an effective processing of sensory stimuli towards the postnatal onset of vision. Beyond these key findings, we expect our approach to guide future research about postnatal development of neural networks, by providing concrete predications that can be tested experimentally.

In sum, the methods and models described in this thesis provide for an advanced computational analysis of calcium imaging data, thereby facilitating the functional analysis of neuronal assemblies under diverse physiological and pathophysiological conditions.

6. References

Ackman JB, Burbridge TJ, Crair MC. 2012. Retinal waves coordinate patterned activity throughout the developing visual system. Nature, 490 (7419):219-225.

Adelsberger H, Garaschuk O, Konnerth A. 2005. Cortical calcium waves in resting newborn mice. Nat Neurosci, 8 (8):988-990.

Arichi T, Whitehead K, Barone G, Pressler R, Padormo F, Edwards AD, Fabrizi L. 2017. Localization of spontaneous bursting neuronal activity in the preterm human brain with simultaneous EEG-fMRI. Elife, 6.

Baillet S. 2017. Magnetoencephalography for brain electrophysiology and imaging. Nat Neurosci, 20 (3):327-339.

Bakkum BW, Benevento LA, Cohen RS. 1991. Effects of light/dark- and dark-rearing on synaptic morphology in the superior colliculus and visual cortex of the postnatal and adult rat. J Neurosci Res, 28 (1):65-80.

Barak O, Tsodyks M. 2007. Persistent activity in neural networks with dynamic synapses. PLoS Comput Biol, 3 (2):e35.

Ben-Ari Y, Gaiarsa JL, Tyzio R, Khazipov R. 2007. GABA: a pioneer transmitter that excites immature neurons and generates primitive oscillations. Physiol Rev, 87 (4):1215-1284.

Brenowitz SD, Regehr WG. 2007. Reliability and heterogeneity of calcium signaling at single presynaptic boutons of cerebellar granule cells. J Neurosci, 27 (30):7888-7898.

Burbridge TJ, Xu HP, Ackman JB, Ge X, Zhang Y, Ye MJ, Zhou ZJ, Xu J, Contractor A, Crair MC. 2014. Visual circuit development requires patterned activity mediated by retinal acetylcholine receptors. Neuron, 84 (5):1049-1064.

Buzsaki G, Anastassiou CA, Koch C. 2012. The origin of extracellular fields and currents - EEG, ECoG, LFP and spikes. Nature Reviews Neuroscience, 13 (6):407-420.

Catterall WA. 2000. Structure and regulation of voltage-gated Ca2+ channels. Annu Rev Cell Dev Biol, 16:521-555.

Chagnac-Amitai Y, Connors BW. 1989. Horizontal spread of synchronized activity in neocortex and its control by GABA-mediated inhibition. J Neurophysiol, 61 (4):747-758.

Chen JL, Andermann ML, Keck T, Xu NL, Ziv Y. 2013a. Imaging neuronal populations in behaving rodents: paradigms for studying neural circuits underlying behavior in the mammalian cortex. J Neurosci, 33 (45):17631-17640.

Chen TW, Wardill TJ, Sun Y, Pulver SR, Renninger SL, Baohan A, Schreiter ER, Kerr RA, Orger MB, Jayaraman V, Looger LL, Svoboda K, Kim DS. 2013b. Ultrasensitive fluorescent proteins for imaging neuronal activity. Nature, 499 (7458):295-300.

Chorev E, Epsztein J, Houweling AR, Lee AK, Brecht M. 2009. Electrophysiological recordings from behaving animals--going beyond spikes. Curr Opin Neurobiol, 19 (5):513-519.

Chow MS, Wu SL, Webb SE, Gluskin K, Yew DT. 2017. Functional magnetic resonance imaging and the brain: A brief review. World J Radiol, 9 (1):5-9.

Clements JD, Bekkers JM. 1997. Detection of spontaneous synaptic events with an optimally scaled template. Biophys J, 73 (1):220-229.

Colonnese MT, Kaminska A, Minlebaev M, Milh M, Bloem B, Lescure S, Moriette G, Chiron C, Ben-Ari Y, Khazipov R. 2010. A conserved switch in sensory processing prepares developing neocortex for vision. Neuron, 67 (3):480-498.

Daunizeau J, Friston KJ, Kiebel SJ. 2009. Variational Bayesian identification and prediction of stochastic nonlinear dynamic causal models. Physica D-Nonlinear Phenomena, 238 (21):2089-2118.

Daunizeau J, Adam V, Rigoux L. 2014. VBA: a probabilistic treatment of nonlinear models for neurobiological and behavioural data. PLoS Comput Biol, 10 (1):e1003441.

David O, Kiebel SJ, Harrison LM, Mattout J, Kilner JM, Friston KJ. 2006. Dynamic causal modeling of evoked responses in EEG and MEG. Neuroimage, 30 (4):1255-1272.

De Felipe J, Marco P, Fairen A, Jones EG. 1997. Inhibitory synaptogenesis in mouse somatosensory cortex. Cereb Cortex, 7 (7):619-634.

Dupont E, Hanganu IL, Kilb W, Hirsch S, Luhmann HJ. 2006. Rapid developmental switch in the mechanisms driving early cortical columnar networks. Nature, 439 (7072):79-83.

Easton CR, Weir K, Scott A, Moen SP, Barger Z, Folch A, Hevner RF, Moody WJ. 2014. Genetic elimination of GABAergic neurotransmission reveals two distinct pacemakers for spontaneous waves of activity in the developing mouse cortex. J Neurosci, 34 (11):3854-3863.

Ermentrout B, Terman D. 2010. Mathematical Foundations of Neuroscience. Springer.

Etherington SJ, Williams SR. 2011. Postnatal development of intrinsic and synaptic properties transforms signaling in the layer 5 excitatory neural network of the visual cortex. J Neurosci, 31 (26):9526-9537.

Feldmeyer D, Radnikow G. 2009. Developmental alterations in the functional properties of excitatory neocortical synapses. J Physiol-London, 587 (9):1889-1896.

FitzHugh R. 1955. Mathematical models of threshold phenomena in the nerve membrane. Bulletin of Mathematical Biology, 17 (4):257-278.

Fitzhugh R. 1961. Impulses and Physiological States in Theoretical Models of Nerve Membrane. Biophys J, 1 (6):445-466.

Garaschuk O, Linn J, Eilers J, Konnerth A. 2000. Large-scale oscillatory calcium waves in the immature cortex. Nat Neurosci, 3 (5):452-459.

Gobel W, Helmchen F. 2007. In vivo calcium imaging of neural network function. Physiology (Bethesda), 22:358-365.

Golshani P, Goncalves JT, Khoshkhoo S, Mostany R, Smirnakis S, Portera-Cailliau C. 2009. Internally mediated developmental desynchronization of neocortical network activity. J Neurosci, 29 (35):10890-10899.

Greenberg DS, Houweling AR, Kerr JN. 2008. Population imaging of ongoing neuronal activity in the visual cortex of awake rats. Nat Neurosci, 11 (7):749-751.

Grewe BF, Langer D, Kasper H, Kampa BM, Helmchen F. 2010. High-speed in vivo calcium imaging reveals neuronal network activity with near-millisecond precision (vol 7, pg 399, 2010). Nature Methods, 7 (6):479-479.

Grienberger C, Konnerth A. 2012. Imaging calcium in neurons. Neuron, 73 (5):862-885.

Harris KD, Quiroga RQ, Freeman J, Smith SL. 2016. Improving data quality in neuronal population recordings. Nat Neurosci, 19 (9):1165-1174.

Herreras O. 2016. Local Field Potentials: Myths and Misunderstandings. Front Neural Circuits, 10:101.

Izhikevich E. 2007. Dynamical systems in neuroscience : the geometry of excitability and bursting. MIT Press.

Izhikevich EM. 2004. Which model to use for cortical spiking neurons? Neural Networks, IEEE Transactions on, 15 (5):1063-1070.

Jackson AF, Bolger DJ. 2014. The neurophysiological bases of EEG and EEG measurement: a review for the rest of us. Psychophysiology, 51 (11):1061-1071.

Kerr JN, Greenberg D, Helmchen F. 2005a. Imaging input and output of neocortical networks in vivo. Proc Natl Acad Sci U S A, 102 (39):14063-14068.

Kerr JN, de Kock CP, Greenberg DS, Bruno RM, Sakmann B, Helmchen F. 2007. Spatial organization of neuronal population responses in layer 2/3 of rat barrel cortex. J Neurosci, 27 (48):13316-13328.

Kerr JND, Greenberg D, Helmchen F. 2005b. Imaging input and output of neocortical networks in vivo. Proceedings of the National Academy of Sciences of the United States of America, 102 (39):14063-14068.

Khazipov R, Luhmann HJ. 2006. Early patterns of electrical activity in the developing cerebral cortex of humans and rodents. Trends Neurosci, 29 (7):414-418.

Khazipov R, Sirota A, Leinekugel X, Holmes GL, Ben-Ari Y, Buzsaki G. 2004. Early motor activity drives spindle bursts in the developing somatosensory cortex. Nature, 432 (7018):758-761.

Kiebel SJ, Garrido MI, Moran R, Chen CC, Friston KJ. 2009. Dynamic causal modeling for EEG and MEG. Hum Brain Mapp, 30 (6):1866-1876.

Kirmse K, Hubner CA, Isbrandt D, Witte OW, Holthoff K. 2018. GABAergic Transmission during Brain Development: Multiple Effects at Multiple Stages. Neuroscientist, 24 (1):36-53.

Kirmse K, Kummer M, Kovalchuk Y, Witte OW, Garaschuk O, Holthoff K. 2015. GABA depolarizes immature neurons and inhibits network activity in the neonatal neocortex in vivo. Nat Commun, 6:7750.

Latham PE, Nirenberg S. 2004. Computing and stability in cortical networks. Neural Comput, 16 (7):1385-1412.

Leinekugel X, Khazipov R, Cannon R, Hirase H, Ben-Ari Y, Buzsaki G. 2002. Correlated bursts of activity in the neonatal hippocampus in vivo. Science, 296 (5575):2049-2052.

Lin MZ, Schnitzer MJ. 2016. Genetically encoded indicators of neuronal activity. Nat Neurosci, 19 (9):1142-1153.

Linden H, Tetzlaff T, Potjans TC, Pettersen KH, Grun S, Diesmann M, Einevoll GT. 2011. Modeling the spatial reach of the LFP. Neuron, 72 (5):859-872.

Luhmann HJ, Sinning A, Yang JW, Reyes-Puerta V, Stuttgen MC, Kirischuk S, Kilb W. 2016. Spontaneous Neuronal Activity in Developing Neocortical Networks: From Single Cells to Large-Scale Interactions. Front Neural Circuit, 10.

Lystad RP, Pollard H. 2009. Functional neuroimaging: a brief overview and feasibility for use in chiropractic research. The Journal of the Canadian Chiropractic Association, 53 (1):59-72.

Majewska A, Sur M. 2003. Motility of dendritic spines in visual cortex in vivo: changes during the critical period and effects of visual deprivation. Proc Natl Acad Sci U S A, 100 (26):16024-16029.

Marguet SL, Le-Schulte VT, Merseburg A, Neu A, Eichler R, Jakovcevski I, Ivanov A, Hanganu-Opatz IL, Bernard C, Morellini F, Isbrandt D. 2015. Treatment during a vulnerable developmental period rescues a genetic epilepsy. Nat Med, 21 (12):1436-1444.

Millman D, Mihalas S, Kirkwood A, Niebur E. 2010. Self-organized criticality occurs in non-conservative neuronal networks during Up states. Nat Phys, 6 (10):801-805.

Min BK, Marzelli MJ, Yoo SS. 2010. Neuroimaging-based approaches in the brain-computer interface. Trends Biotechnol, 28 (11):552-560.

Minlebaev M, Ben-Ari Y, Khazipov R. 2007. Network mechanisms of spindle-burst oscillations in the neonatal rat barrel cortex in vivo. J Neurophysiol, 97 (1):692-700.

Mongillo G, Barak O, Tsodyks M. 2008. Synaptic theory of working memory. Science, 319 (5869):1543-1546.

Moreaux L, Laurent G. 2007. Estimating firing rates from calcium signals in locust projection neurons in vivo. Front Neural Circuits, 1:2.

O'Shea DJ, Trautmann E, Chandrasekaran C, Stavisky S, Kao JC, Sahani M, Ryu S, Deisseroth K, Shenoy KV. 2017. The need for calcium imaging in nonhuman primates: New motor neuroscience and brain-machine interfaces. Exp Neurol, 287 (Pt 4):437-451.

Obien MEJ, Deligkaris K, Bullmann T, Bakkum DJ, Frey U. 2015. Revealing neuronal function through microelectrode array recordings. Frontiers in Neuroscience, 8.

Ohki K, Chung S, Ch'ng YH, Kara P, Reid RC. 2005. Functional imaging with cellular resolution reveals precise micro-architecture in visual cortex. Nature, 433 (7026):597-603.

Olshausen BA, Field DJ. 2004. Sparse coding of sensory inputs. Curr Opin Neurobiol, 14 (4):481-487.

Ozeki H, Finn IM, Schaffer ES, Miller KD, Ferster D. 2009. Inhibitory stabilization of the cortical network underlies visual surround suppression. Neuron, 62 (4):578-592.

Park IJ, Bobkov YV, Ache BW, Principe JC. 2013. Quantifying bursting neuron activity from calcium signals using blind deconvolution. J Neurosci Methods, 218 (2):196-205.

Pnevmatikakis EA, Soudry D, Gao Y, Machado TA, Merel J, Pfau D, Reardon T, Mu Y, Lacefield C, Yang W, Ahrens M, Bruno R, Jessell TM, Peterka DS, Yuste R, Paninski L. 2016. Simultaneous Denoising, Deconvolution, and Demixing of Calcium Imaging Data. Neuron, 89 (2):285-299.

Prevedel R, Verhoef AJ, Pernia-Andrade AJ, Weisenburger S, Huang BS, Nobauer T, Fernandez A, Delcour JE, Golshani P, Baltuska A, Vaziri A. 2016. Fast volumetric calcium imaging across multiple cortical layers using sculpted light. Nature Methods, 13 (12):1021-U1215.

Rahmati V, Kirmse K, Holthoff K, Kiebel SJ. 2018. Ultra-fast accurate reconstruction of spiking activity from calcium imaging data. J Neurophysiol, 119 (5):1863-1878.

Rahmati V, Kirmse K, Markovic D, Holthoff K, Kiebel SJ. 2016. Inferring Neuronal Dynamics from Calcium Imaging Data Using Biophysical Models and Bayesian Inference. PLoS Comput Biol, 12 (2):e1004736.

Rahmati V, Kirmse K, Holthoff K, Schwabe L, Kiebel SJ. 2017. Developmental Emergence of Sparse Coding: A Dynamic Systems Approach. Sci Rep, 7 (1):13015.

Reiff DF, Ihring A, Guerrero G, Isacoff EY, Joesch M, Nakai J, Borst A. 2005. In vivo performance of genetically encoded indicators of neural activity in flies. J Neurosci, 25 (19):4766-4778.

Rigoux L, Stephan KE, Friston KJ, Daunizeau J. 2014. Bayesian model selection for group studies - revisited. Neuroimage, 84:971-985.

Rochefort NL, Garaschuk O, Milos RI, Narushima M, Marandi N, Pichler B, Kovalchuk Y, Konnerth A. 2009. Sparsification of neuronal activity in the visual cortex at eye-opening. Proc Natl Acad Sci U S A, 106 (35):15049-15054.

Russell JT. 2011. Imaging calcium signals in vivo: a powerful tool in physiology and pharmacology. Br J Pharmacol, 163 (8):1605-1625.

Sasaki T, Takahashi N, Matsuki N, Ikegaya Y. 2008. Fast and accurate detection of action potentials from somatic calcium fluctuations. Journal of Neurophysiology, 100 (3):1668-1676.

Shadlen MN, Newsome WT. 1994. Noise, neural codes and cortical organization. Curr Opin Neurobiol, 4 (4):569-579.

Smetters D, Majewska A, Yuste R. 1999. Detecting action potentials in neuronal populations with calcium imaging. Methods, 18 (2):215-221.

Stephan KE, Penny WD, Daunizeau J, Moran RJ, Friston KJ. 2009. Bayesian model selection for group studies. Neuroimage, 46 (4):1004-1017.

Takano H, McCartney M, Ortinski PI, Yue C, Putt ME, Coulter DA. 2012. Deterministic and stochastic neuronal contributions to distinct synchronous CA3 network bursts. J Neurosci, 32 (14):4743-4754.

Tolner EA, Sheikh A, Yukin AY, Kaila K, Kanold PO. 2012. Subplate neurons promote spindle bursts and thalamocortical patterning in the neonatal rat somatosensory cortex. J Neurosci, 32 (2):692-702.

Tsodyks M, Pawelzik K, Markram H. 1998. Neural networks with dynamic synapses. Neural Comput, 10 (4):821-835.

Uludag K, Roebroeck A. 2014. General overview on the merits of multimodal neuroimaging data fusion. Neuroimage, 102:3-10.

Valeeva G, Tressard T, Mukhtarov M, Baude A, Khazipov R. 2016. An Optogenetic Approach for Investigation of Excitatory and Inhibitory Network GABA Actions in Mice Expressing Channelrhodopsin-2 in GABAergic Neurons. J Neurosci, 36 (22):5961-5973.

van der Bourg A, Yang JW, Reyes-Puerta V, Laurenczy B, Wieckhorst M, Stuttgen MC, Luhmann HJ, Helmchen F. 2016. Layer-Specific Refinement of Sensory Coding in Developing Mouse Barrel Cortex. Cereb Cortex.

Vanhatalo S, Palva JM, Andersson S, Rivera C, Voipio J, Kaila K. 2005. Slow endogenous activity transients and developmental expression of K+-Cl- cotransporter 2 in the immature human cortex. Eur J Neurosci, 22 (11):2799-2804.

Vogelstein JT, Watson BO, Packer AM, Yuste R, Jedynak B, Paninski L. 2009. Spike Inference from Calcium Imaging Using Sequential Monte Carlo Methods. Biophysical Journal, 97 (2):636-655.

Vogelstein JT, Packer AM, Machado TA, Sippy T, Babadi B, Yuste R, Paninski L. 2010. Fast nonnegative deconvolution for spike train inference from population calcium imaging. J Neurophysiol, 104 (6):3691-3704.

Yaksi E, Friedrich RW. 2006. Reconstruction of firing rate changes across neuronal populations by temporally deconvolved Ca2+ imaging. Nat Methods, 3 (5):377-383.

Yang JW, Hanganu-Opatz IL, Sun JJ, Luhmann HJ. 2009. Three patterns of oscillatory activity differentially synchronize developing neocortical networks in vivo. J Neurosci, 29 (28):9011-9025.

Yang W, Carrillo-Reid L, Bando Y, Peterka DS, Yuste R. 2018. Simultaneous two-photon imaging and two-photon optogenetics of cortical circuits in three dimensions. Elife, 7.

Zhang J, Ackman JB, Xu HP, Crair MC. 2011. Visual map development depends on the temporal pattern of binocular activity in mice. Nat Neurosci, 15 (2):298-307.

Zucker RS, Regehr WG. 2002. Short-term synaptic plasticity. Annu Rev Physiol, 64:355-405.

7. Appendix

Danksagung

I would like to warmly thank Prof. Dr. Stefan Kiebel and Prof. Dr. Knut Holthoff for their very kind and excellent mentorships and their constructive and outstanding discussions. I would like also to warmly thank PD. Dr. Knut Kirmse who always supported me with his generous help, fruitful discussions, his patience in answering my experimental questions and, importantly, for his persistence in directing my motivation towards the important scientific questions. To pursue my research interests in neuroscience, they provided me with a great chance to learn the discipline and precision required to both generate worthy and striking scientific results and, at the same time, aim at the questions which will have a real contribution to the field.

I would like to thank my colleague MSc. Dario Cuevas Rivera for his sincere friendship, generous help, and his fruitful discussions on mathematical concepts. I am also thankful to my colleagues in the Chair of Neuroimaing at Technical University of Dresden and my colleagues in the Bioimaging group at the University Hospital Jena for the outstanding atmosphere, and also their trust on my expertise for analyzing their data. I would like also to warmly thank Prof. Dr. Lars Schwabe who introduced me to the neuroscience world, helped me in adapting my scientific background to this new environment, and who always supported me with showing the directions which can lead to my success.

Personal thanks go to my family, especially to my wife Sadaf S. T. and to my parents. They offered me their unconditional affection and support. Especially, I would not have been able to complete this work without my wife's patience, support, help, and kindness.

Ehrenwörtliche Erklärung

Hiermit erkläre ich, dass mir die Promotionsordnung der Medizinischen Fakultät der Friedrich-Schiller-Universität bekannt ist,

ich die Dissertation selbst angefertigt habe und alle von mir benutzten Hilfsmittel, persönlichen Mitteilungen und Quellen in meiner Arbeit angegeben sind,

mich folgende Personen bei der Auswahl und Auswertung des Materials sowie bei der Herstellung des Manuskripts unterstützt haben: Knut Kirmse, Knut Holthoff, Dimitriji Markovic, Lars Schwabe, Stefan Kiebel,

die Hilfe eines Promotionsberaters nicht in Anspruch genommen wurde und dass Dritte weder unmittelbar noch mittelbar geldwerte Leistungen von mir für Arbeiten erhalten haben, die im Zusammenhang mit dem Inhalt der vorgelegten Dissertation stehen,

dass ich die Dissertation noch nicht als Prüfungsarbeit für eine staatliche oder andere wissenschaftliche Prüfung eingereicht habe und

dass ich die gleiche, eine in wesentlichen Teilen ähnliche oder eine andere Abhandlung nicht bei einer anderen Hochschule als Dissertation eingereicht habe.

Jena, 21.07.2019 Vahid Rahmati

---------- ----------

Ort, Datum **Unterschrift des Verfassers**